A Sample of Galactic PDRs: [CII] Optical Depth Effects and Self-Absorption

Inaugural-Dissertation
zur
Erlangung des Doktorgrades
der Mathematisch-Naturwissenschaftlichen Fakultät
der Universität zu Köln

vorgelegt von

Cristian Guevara N.

aus Copiapó, Chile

Köln, 2019

To my Wife, Parents and Grandmother

Abstract

The main objective of this work was to determine the optical depth of the ionized carbon and to study the effects that could be arise from this optical depth. For this reason, high spectral resolution and sensitivity observations were done of the [^{12}CII] ^{2}P$_{3/2}$-^{2}P$_{1/2}$ 158 μm fine structure line and the [^{13}CII] hyperfine structure line splitted into three components. The observations were done simultaneously with up-GREAT 7x2 array receiver on board the airborne observatory SOFIA towards four photodissociation regions covering a wide range of physical conditions: the HII region M43, the edge-on and faint Horsehead photodissociation region, the spherical and highly ionized Monoceros R2 and the massive and clumpy M17 SW. Additionally, the M17 complex was observed in [CI] ^{3}P$_1$-^{3}P$_0$ 609 μm line in order to study the large scale [CI] emission along M17 SW and M17 N. The observations were done with the SMART array receiver of the NANTEN2 telescope at high spatial and spectral resolution.

As a first step, direct comparisons of the [^{12}CII] and [^{13}CII] emission line profiles and intensities for multiple positions in each source, assuming a single homogeneous layer and a reasonable ^{12}C/^{13}C abundance ratio, have revealed that the Cp13 line, scaled up by the canonical abundance ratio between ^{12}C and ^{13}C, completely overshoots the [^{12}CII] emission with different line profiles. Thus, [^{12}CII] is optically thick in all sources and, in the case of Mon R2 and M17 SW, is heavily affected by self-absorption effects. Column densities derived from the [^{13}CII] integrated intensity show extremely high column densities, four times higher than the column densities derived directly from [^{12}CII] integrated intensity. This situation required a more sophisticated analysis. A multi-component dual layer model of the radiative transfer equation has been developed to take into account the discrepancy between the line profiles of both isotopes,as well as the intensities between them. The model allows the simultaneous fit of the emission of both isotopes and the derivation of the physical properties of the [CII] gas, namely column density and excitation temperature. The model is composed of a background emitting layer and a foreground absorbing layer. The parameters derived from the model show extremely high background column densities, up to 10^{19} cm^{-2} or as an equivalent visual extinction around 41 magnitudes; and cold foreground column densities up

to 10^{18} cm^{-2} or 13 mag. Also, a multi-component single layer model has been studied, but it has been discarded as a physically unlikely scenario. The extreme background column densities require multiple PDR surfaces stacked along the line of sight, showing a clumpy structure. The cold high column density foreground gas can not be explained with any known scenario and only speculations can be done to explain its origin.

The M17 SW [CI] observations have shown the velocity distribution of the [CI] emission and, through the analysis of momenta maps, three distinctive velocity structures have been identified. Each structure can be associated with HI atomic gas, H_2 molecular gas and as a part of a foreground molecular cloud associated to the M17 complex, respectively. The [CI] column density of the complex ranges between 10^{17} and 10^{18} cm^{-2}, or in equivalent visual extinction, between 1 and 10 magnitudes. M17 SW has the larger amount of material and the larger column density. The [CI] spectra are shifted to the redder part of the spectra, with respect to molecular and ionized tracers. Also, the [CI] equivalent visual extinction is much lower compared to the other tracers. This can be explained as an expected deficit of neutral carbon, but precise measurements of the local abundances needed to derive the extinctions would require the use of numerical models and large scale data sets of complementary tracers, that will be part of future work.

Zusammenfassung

Das Hauptziel dieser Arbeit war es, die optische Tiefe des ionisierten Kohlenstoffs zu bestimmen, und Effekte die daraus herrühren. Zu diesem Zweck wurden spektral hochaufgelöste Beobachtungen mit hoher Sensititivität von der [^{12}CII] ^{2}P$_{3/2}$-^{2}P$_{1/2}$ 158 μm Feinstrukturlinie und den [^{13}CII] Hyperfeinstrukturlinien, die in drei Komponenten aufgespaltet sind, gemacht. Diese Beobachtungen wurden simultan mit dem upGREAT 7x2 Array-Empfänger an Bord des SOFIA-Flugzeugs in Richtung von vier Photodissoziationsregionen (PDR) erlangt, die eine große Vielfalt von physikalischen Bedingungen abbilden: die HII-Region M43, die leuchtschwache "edge-on" Horsehead Photodissoziationsregion, die sphärische und hochionisierte Monoceros R2, und die massive und klumpige M17 SW Region. Zusätzlich wurde der M17 Komplex in der [CI] ^{3}P$_1$-^{3}P$_0$ 609 μm Linie beobachtet um die großräumige [CI] Emission entlang von M17 SW und M17 N zu untersuchen. Diese Beobachtungen wurden mit dem SMART Array-Empfänger des NANTEN2-Teleskops mit hoher spektraler und räumlicher Auflösung erlangt.

In einem ersten Schritt wurden die Emissionslinienprofile von [^{12}CII] und [^{13}CII] verglichen, sowie die Intensitäten für etliche Positionen in jeder Quelle. Dies geschah unter der Annahme einer einzelnen, homogenen, emittierenden Schicht und eines angemessenen ^{12}C/^{13}C Isotopenverhältnisses. Diese Analyse ergab, dass die mit dem kanonischen Isotopenverhältnis von ^{12}C/^{13}C skalierte [^{13}CII] Linie komplett die [^{12}CII] Emission mit verschiedenen Linienprofilen übertrifft. Das lässt darauf schließen, dass [^{12}CII] in allen Quellen optisch dick und, im Falle von Mon R2 und M17 SW, stark von Selbstabsorptionseffekten betroffen ist. Die Säulendichten, die aus den integrierten [^{13}CII] Intensitäten gewonnen wurden, sind extrem hoch; vier mal höher als die aus den integrierten Intensitäten von [^{12}CII]. Diese Situation erforderte eine wesentlich anspruchsvollere Analyse. Hierfür wurde ein Zweischichtmodell mit mehreren Komponenten der Strahlungstransportgleichung erwickelt, um sowohl den Unterschieden zwischen den Linienprofilen beider Isotope Rechnung zu tragen, wie auch den Unterschieden ihrer Intensitäten. Das Modell erlaubt den gleichzeitigen Fit der Emission beider Isotope und die Herleitung der physikalischen Eigenschaften des [CII] Gases, genauer die Säulendichte und Anregungstemperatur. Das Modell besteht aus einer emittierenden Hintergrundschicht

und einer absorbierenden Vordergrundschicht. Die Parameter aus dem Modell zeigen extrem hohe Säulendichten im Hintergrund, bis zu 10^{19} cm^{-2} oder einer äquivalenten visuellen Extinktion von 41 Magnituden; die kalte Vordergrundkomponente hat eine Säulendichte von bis zu 10^{18} cm^{-2} oder 13 Magnituden. Weiterhin wurde ein Einschichtmodell mit mehreren Komponenten untersucht, doch als physikalisch unwahrscheinlich verworfen. Die extremen Säulendichten im Hintergrund werden durch mehrere, entlang der Sichtlinie übereinander liegende PDR Oberflächen erzeugt, die eine klumpige Struktur besitzen. Die hohe Säulendichte des kalten Vordergrundgases kann mit keinem bekannten Szenario erklärt werden und bisher kann zu seinem Ursprung nur spekuliert werden.

Die M17 SW [CI] Beobachtungen zeigen die Geschwindigkeitsverteilung der [CI]-Emission und es konnten, durch die Analyse der Momentekarten, drei verschiedene Geschwindigkeitsstukturen identifiziert werden. Jede dieser Strukturen kann mit atomarem Wasserstoffgas (HI), molekularem Wasserstoffgas (H$_2$), oder als Teil der molekularen Vordergrundwolken in Verbindung mit dem M17-Komplex in Verbindung gesetzt werden. Die [CI] Säulendichte des Komplexes liegt zwischen 10^{17} und 10^{18} cm^{-2}, entsprechend einer visuellen Extinktion von 1 bis 10 Magnituden. M17 SW hat eine höhere Menge an Material und eine höhere Säulendichte. Die [CI]-Spektren sind relativ zu den molekularen und ionisierten Emissionen zum roten (langwelligen) Teil des Spektrums hin verschoben. Weiterhin ist die [CI] äquivalente visuelle Extinktion wesentlich niedriger im Vergleich zu den Werter anderer Indikatoren. Dies kann als ein erwartetes Defizit neutralen Kohlenstoffs erklärt werden, doch werden hierzu präzise Messungen der lokalen Häufigkeiten benötigt, um die Extinktion herzuleiten, die wiederum numerische Modelle und größere Datensätze komplementärer Indikatoren erfordern, was Teil von zukünftiger Arbeit sein wird.

Contents

CONTENTS

1 | Introduction

Photodissociation Regions (PDRs) are zones of the interstellar medium (ISM) in which Far-UV photons dominate the thermal balance, chemistry, structure and distribution of the gas and dust of such regions. The incident FUV field photodissociates molecules, photoionizes atoms and molecules and heats the gas and dust. The gas is mainly cooled through fine structure line emission of excited atoms, such as [CII], [OI] and [CI]. These lines are key to study the ISM structure and dynamics.

The [CII] 158 μm fine structure line is one of the brightest emission lines in PDRs and the main cooling line in the atomic and molecular gas. The [CII] line is not only used to study the local galactic ISM, but is also used as a star-formation tracer for nearby and high redshift galaxies (eg. Boselli et al. 2002; De Looze et al. 2011; Herrera-Camus et al. 2015) due to its ionization by FUV photons produced by nearby OB stars, creating a link between the star formation activity and the [CII] emission. Therefore, it is essential to know whether the [CII] line emission is optically thin or thick. The concern to know the optical depth of [CII] has been present since the first observations of [CII]. Russell et al. (1980) refers in the first [CII] observation article that: *"Optical depth effects in the 157 μm line may be significant but have not been taken into account in our calculations because our data base is still too restricted"*. Traditionally, [CII] has been considered as an optically thin line with an optical depth around unity, but systematic measurements of the optical depth has been only done in a few cases in the last years.

As this issue has not been sufficiently addressed, the main objective of this work was to determine the optical depth of the ionized carbon, to study the effects that could be arise from this optical depth and determine the physical parameters of the ionized carbon through the observations of [^{12}CII] and [^{13}CII]. This key analysis has not been done before because, just recently, it has been tecnically feasible to observe both lines simultaneously at high sensitivity and spectral resolution.

Additionally, a fundamental element in the development of a new generation of receivers and observatories, is to have a selection of targets that may act as test

cases for the future observations. Hence, for one of the sources observed in [CII], observations were done in [CI] to be used as a pathfinder for large scale mapping of star forming regions. Therefore, an additional objective for this work was to study the large scale [CI] emission of the observations mentioned above.

2 | Physical Background

The present chapter explains the physical framework required to understand the emission of radiation by atoms and molecules in the GHz and THz frequency regimes studied for this work. This chapter outlines the basic physics of the radiation process, describes photodissociation regions in which the line emission originates, as well as details the characteristics of the different atoms and molecules employed in this work. The physical background is based on the following books: *Radiative Processes in Astrophysics* (Rybicki & Lightman 1979), *The Physics and Chemistry of the Interstellar Medium* (Tielens 2005), *Tools of Radio Astronomy* (Wilson et al. 2009) and *Physics of the Interstellar and Intergalactic Medium* (Draine 2011).

2.1 Radiation

The electromagnetic radiation can be considered as waves or photons of the electromagnetic field which radiate through the space, traveling in straight lines called rays. Hence, the energy of a ray crossing an area dA normal to the direction of the ray within a solid angle $d\omega$ in a time dt in a frequency range $d\nu$ can be defined as:

$$dE = I_\nu \, dA \, dt \, d\Omega \, d\nu \tag{2.1}$$

Where, I_ν represents the specific intensity in units of erg s^{-1} cm^{-2} ster^{-1} Hz^{-1}. By definition, the specific intensity I_ν is constant, as long as there is no emission or absorption. In particular, it is constant along the ray, independent of the distance to the source. Additionally, and knowing that the radiation propagates at the velocity of light c, the specific energy density u_ν is defined as the amount of energy contained in a volume of length cdt and area dA:

$$dE = u_\nu(\Omega) \, dA \, c \, dt \, d\Omega \, d\nu \tag{2.2}$$

Combining both equations above, $u_\nu(\Omega)$ results in:

$$u_\nu(\Omega) = \frac{1}{c} I_\nu \qquad (2.3)$$

Therefore, the mean intensity J_ν can be defined as:

$$J_\nu = \frac{1}{4\pi} \int I_\nu d\Omega \qquad (2.4)$$

2.2 Planck Function

2.2.1 Planck Spectrum

The Planck spectrum describes the electromagnetic radiation emitted by a black body i.e. a radiation source in thermal equilibrium. A proper derivation can be found in physics textbooks such as *Radiative Processes in Astrophysics* (Rybicki & Lightman 1979). Thus, the specific intensity defined above in case of thermal equilibrium is described by the black body emission $B_\nu(T)$, for a given temperature T and frequency ν, as:

$$B_\nu(T) = I_\nu(T) = \frac{2h\nu^3}{c^2} \frac{1}{e^{h\nu/k_B T} - 1} \qquad (2.5)$$

with k_B the Boltzmann's constant (1.38×10^{-16} erg K^{-1}). Figure 2.1 shows B$_\nu$(T) at different temperatures, on a double logarithmic scale.

2.2.2 Radiation and Rayleigh-Jeans Brightness Temperature

At low frequencies and at sufficiently large temperatures (>20 K), $h\nu \ll k_B T$. Therefore, $e^{h\nu/k_B T}$ can be approximated as:

$$e^{h\nu/k_B T} \cong 1 + \frac{h\nu}{k_B T} + O\left(\frac{h\nu}{k_B T}\right)^2 \qquad (2.6)$$

and using Eq 2.6 to first order in 2.5, $B_\nu(T)$ becomes:

$$B_\nu(T) \sim \frac{2\nu^2 k_B T}{c^2} \qquad (2.7)$$
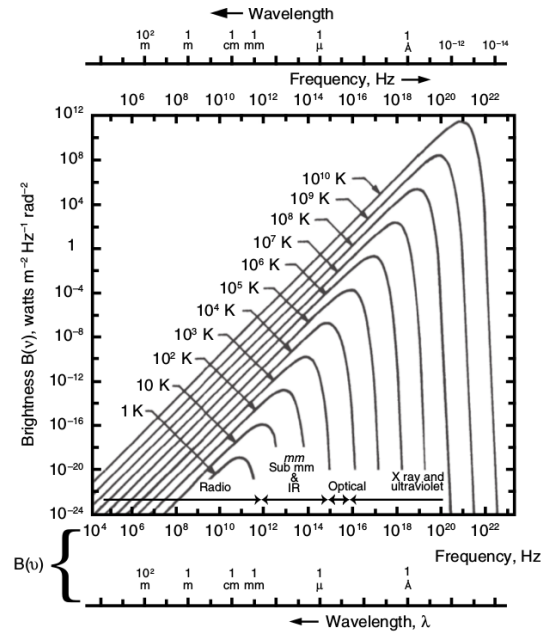
Figure 2.1: Black bodies at different temperatures with their Planck spectrum (Wilson et al. 2009).

This is also known as the Rayleigh-Jeans law, and it is a valid approximation in the limit of low frequencies and large temperatures in thermodynamic equilibrium. From there, we can define the Rayleigh-Jeans equivalent temperature $J(T)$ as:

$$J(T) = \frac{c^2}{2\nu^2 k_B} B_\nu(T) = \frac{h\nu}{k} \frac{1}{e^{h\nu/kT} - 1} \tag{2.8}$$

And, for the general case, outside thermodynamic equilibrium, the Rayleigh-Jeans brightness temperature T_b can be defined as:

$$T_b = \frac{c^2}{2\nu^2 k_B} I_\nu \tag{2.9}$$

The brightness temperature will be similar to the physical blackbody temperature only in the Rayleigh-Jeans limit (low frequencies and/or high temperatures).

2.3 Radiative Transfer Equation

The specific intensity is independent of the distance along the ray for the radiation in free space. But, it will change if radiation is absorbed or emitted. This change is described by the radiative transfer equation. The equation of radiative transfer can be defined for radiation with an intensity I_ν traversing a slab of material with a

path-length s along the direction of propagation as:

$$\frac{dI_\nu}{ds} = -\alpha_\nu I_\nu + j_\nu \tag{2.10}$$

The first term, $\alpha_\nu I_\nu$, represents the change in I_ν due to absorption of the incident radiation by the material. α_ν is the attenuation coefficient at frequency ν. The second term, j_ν, corresponds to the emissivity at frequency ν, and changes I_ν due to spontaneous emission of the material and is independent of I_ν

Thus, the optical depth, τ_ν can be defined as:

$$d\tau_\nu = \alpha_\nu ds, \ or \ \tau_\nu(s) = \int_{s_0}^{s} \alpha_\nu(s')ds' \tag{2.11}$$

The optical depth is a measure of the absorption along the path of ray. A medium is considered as optically thin or transparent when the optical depth integrated along the path through the medium is lower than unity (τ_ν <1). This means that the photon absorptions are neglectable. On the other hand, a medium is optically thick or opaque when the optical depth is higher than unity (τ_ν >1) and photon absorptions become important.

Rearranging Eq. 2.10 and using Eq. 2.11, the radiative transfer equation can be expressed as:

$$\frac{dI_\nu}{d\tau_\nu} = -I_\nu + S_\nu \tag{2.12}$$

with S_ν the source function, defined as the ratio of the emission and absorption coefficient by:

$$S_\nu = \frac{j_\nu}{\alpha_\nu} \tag{2.13}$$

Hence, the radiative transfer equation can be formally solved by multiplying Eq. 2.12 by e^{τ_ν} at both sides, and solving the resulting differential equation. The formal solution is:

$$I_\nu(\tau_\nu) = I_\nu(0)e^{-\tau_\nu} + \int_0^{\tau_\nu} e^{-(\tau_\nu - \tau_\nu')}S_\nu(\tau_\nu')d\tau_\nu' \tag{2.14}$$

The first term represents the initial intensity I$_\nu$(0), coming from behind the medium, attenuated by the optical depth factor e$^{-\tau_\nu}$. The second term represents the integral over the source function along the medium attenuated by the factor e$^{-(\tau_\nu - \tau_\nu')}$ due to its internal absorption. There is a special case to consider, when S$_\nu$ is constant. Then equation 2.14 becomes:

$$I_\nu(\tau_\nu) = I_\nu(0)e^{-\tau_\nu} + S_\nu(1 - e^{-\tau_\nu}) = S_\nu + e^{-\tau_\nu}(I_\nu(0) - S_\nu) \tag{2.15}$$

Hence, if $\tau_\nu \to \infty$, then $I_\nu \to S_\nu$, which means that in an opaque medium, the only radiation emitted is the one produced by the medium itself. On the other hand, if $\tau_\nu \to 0$, then $I_\nu \to I_\nu(0)$, meaning that one sees the emission from the background, unaltered by the medium in between.

2.4 Einstein Coefficients

2.4.1 Line Profile Function

Let's suppose a system with two energy levels, a lower level with energy E_l and a statistical weight g_l, and an upper one with energy E_u and statistical weight g$_u$, and $E_u - E_l = h\nu_0$. The energy levels have a finite energy spread, then the difference between them can be described by a line profile function, named $\phi(\nu)$, which peaks at $\nu = \nu_0$. $\phi(\nu)$ is normalized.

$$\int_0^\infty \phi(\nu)d\nu = 1 \tag{2.16}$$

And from Eq. 2.4, the mean line average intensity can be defined as:

$$\bar{J} = \frac{1}{4\pi} \int_0^\infty J_\nu \phi(\nu)d\nu \tag{2.17}$$

The processes responsible for the finite line broadening in the ISM are natural broadening due to the Heisenberg uncertainty principle sue to the finite lifetime of the upper state, and Doppler broadening due to thermal motion and microturbulence of the gas. The natural broadening is due to the uncertainty principle, for a given atomic level i, there is not a perfectly defined energy E_i, but a superposition of energies around E_i. Therefore, transitions of electrons between levels are not defined by an exact energy difference. Then, the line profile function is described by a Lorentz function, given by:

$$\phi(\nu) = \frac{\Gamma}{4\pi^2(\nu - \nu_0)^2 + (\Gamma/2)^2} \tag{2.18}$$

with Γ the quantum-mechanical damping constant, defined as the sum of all transition probabilities for spontaneous emission (see definition below in the next subsection). An additional process, not relevant for this work, is Collisional or Pressure Broadening due to collisions between particles. The line profile is also described by a Lorentzian profile.

Doppler line broadening is the dominant broadening process for line emission in the ISM. It is produced by a combination of random thermal motions and non-thermal turbulent motions by atoms. A gas with a kinetic temperature T_K will have its individual atoms moving towards or away from the observer, producing a Doppler shift. The net effect is to spread the line profile. In combination, there are non-thermal random movements as a product of microturbulence inside the gas. Both of these processes characterize the line profile function by a Gaussian profile. Hence, the total Doppler, that it is a convolution between them, also characterizes $\phi(\nu)$ by a Gaussian profile and it is defined as:

$$\phi(\nu) = \frac{1}{\Delta\nu\sqrt{\pi}}e^{-(\nu-\nu_0)^2/\Delta\nu^2} \tag{2.19}$$

where $\Delta\nu$ is the equivalent width of the line profile of line center ν_0. Also, the line profile, and consequently the optical depth, can be expressed as a function of the velocity as:

$$\phi(v) = \frac{1}{\Delta v\sqrt{\pi}}e^{-(v-v_0)^2/\Delta v^2} \tag{2.20}$$

with $\Delta v = c\Delta\nu/\nu_0$.

2.4.2 Definition of the Coefficients

If the two level system defined above interacts with a photon of energy $h\nu_0$ through emission or absorption, there are three processes that could happen:

- Spontaneous emission: The system starts in the upper state and emits a photon of energy $h\nu_0$, dropping to the lower state, even in absence of a radiation field. We can define the Einstein's coefficient A as:

  A_{ul} = transition probability per unit of time for spontaneous emission.

- Absorption: The system makes a transition from the lower state to the upper one through the absorption of a photon of energy $h\nu_0$. The absorption probability is proportional to the density of photons at frequency ν_0. The absorption probability is:

$$B_{lu}\,\bar{J} = \text{transition probability per unit of time for absorption.}$$

- Stimulated Emission: The stimulated emission is given by the interaction of an incoming photon with an excited atom or molecule. This interaction makes an electron of the atom or molecule drop to a lower energy level and emit a photon of energy $h\nu_0$. The probability of emission is:

$$B_{ul}\,\bar{J} = \text{transition probability per unit of time for stimulated emission.}$$

2.4.3   Equations of Detailed Balance

In thermodynamic equilibrium, the number of transitions from the lower to the upper state is equal to the number of transitions in the opposite direction. Defining the upper and lower state number densities of atoms as n_u and n_l respectively, the equation of balance is:

$$n_l B_{lu}\bar{J} = n_u B_{ul}\bar{J} + n_u A_{ul} \tag{2.21}$$

Isolating $\bar{J}$ from Eq 2.21 results in:

$$\bar{J} = \frac{A_{ul}/B_{ul}}{(n_l/n_u)(B_{lu}/B_{ul}) - 1} \tag{2.22}$$

But in thermodynamic equilibrium, the ratio between the densities is:

$$\frac{n_l}{n_u} = \frac{g_l e^{-E/k_B T}}{g_u e^{-(E+h\nu_0)/k_B T}} \tag{2.23}$$

The levels are populated following the same Boltzmann distribution. From the expression above, the excitation temperature T_{ex} can be defined as the ratio between relative population of two adjacent levels, independent of whether the system is in thermodynamic equilibrium or not.

$$\frac{n_u}{n_l} = \frac{g_u}{g_l} e^{-h\nu_0/k_B T_{\mathrm{ex},ul}} \tag{2.24}$$

In thermodynamic equilibrium, the excitation temperature becomes the physical temperature and is the same for all levels. On the other hand, outside equilibrium, different temperatures may characterize the population of each level. Additionally, assuming local thermodynamic equilibrium (LTE), the radiative transfer equation from Eq. 2.15 can be expressed in terms of T = T_{ex}. Therefore, $S_\nu = B(T_{\mathrm{ex}})$, and expressing $B(T_{\mathrm{ex}})$ in terms of the radiation temperature $J_\nu(T)$ defined above in Eq. 2.8, $J_\nu(T)$ can be written as:

$$J_\nu(T) = J_\nu(T_{\mathrm{bg}})e^{-\tau_\nu} + J_\nu(T_{\mathrm{ex}})(1 - e^{-\tau_\nu}) \tag{2.25}$$

With T_{bg} the radiation coming from behind the medium. Subtracting $J_\nu(T_{\mathrm{bg}})$ from both sides of Eq. 2.25, the line temperature after the subtraction of the background continuum emission becomes:

$$J_\nu(T) - J_\nu(T_{\mathrm{bg}}) = \left[J_\nu(T_{\mathrm{ex}}) - J_\nu(T_{\mathrm{bg}}) \right] \left(1 - e^{-\tau_\nu} \right) \tag{2.26}$$

Then, using Eq.2.24 in Eq. 2.22, $\bar{J}$, in thermal equilibrium, yields:

$$\bar{J} = \frac{A_{ul}/B_{ul}}{(n_l B_{lu}/n_u B_{ul})e^{h\nu_0/k_B T} - 1} \tag{2.27}$$

But in thermodynamic equilibrium, $\bar{J} = B_\nu$. For Eq. 2.27 to be equal to the Planck function (Eq. 2.5) the Einstein Coefficients must fulfill:

$$g_u B_{ul} = g_l B_{lu} \tag{2.28}$$

and

$$A_{ul} = \frac{2h\nu^3}{c^2} B_{ul} \tag{2.29}$$

The two equations above are called equations of detailed balance and they guarantee that the probability for stimulated emission and absorption are the same, except for the degeneracy factors. Also, transitions with high probability of absorption

will have high probability of emission, whether stimulated or spontaneous.

These relationships are independent of the temperature and they are fulfilled always, even when the system is not in thermodynamic equilibrium. Therefore, the Einstein coefficients are intrinsic properties of the atom.

2.4.4 Absorption and Emission Coefficients: relationship to the Einstein Coefficients

The emission and absorption coefficients defined in Sect. 2.3 can be related to the Einstein coefficients defined above after some assumptions. For the emission coefficient j_ν, it can be assumed that the emission is distributed according to the line profile function $\phi(\nu)$ (Eq. 2.16), in a similar way to the absorption. Hence, the emission can be written as:

$$j_\nu = \frac{h\nu_0}{4\pi} n_u A_{ul} \phi(\nu) \tag{2.30}$$

The absorption coefficient (α_ν) takes into account naturally the Einstein absorption coefficient. But, the stimulated emission is also proportional to the intensity, in a similar way to the absorption. Also, both processes happen at the same time and can not be disentangled. For these reasons, the stimulated emission can be treated as a negative absorption. Thus, the absorption coefficient becomes:

$$\alpha_\nu = \frac{h\nu_0}{4\pi} \phi(\nu) \left(n_l B_{lu} - n_u B_{ul} \right) \tag{2.31}$$

Also, Eq. 2.10 and the source function S_ν (Eq. 2.13) can be expressed in terms of the Einstein coefficients as:

$$\frac{dI_\nu}{ds} = -\frac{h\nu}{4\pi} \left(n_l B_{lu} - n_u B_{ul} \right) \phi(\nu) I_\nu + \frac{h\nu}{4\pi} N_u A_{ul} \phi(\nu) \tag{2.32}$$

$$S_\nu = \frac{n_u A_{ul}}{n_l B_{lu} - n_u B_{ul}} \tag{2.33}$$

Hence, using Equations 2.28 and 2.29 in 2.31 and 2.33, α_ν and S_ν result in:

$$\alpha_\nu = \frac{h\nu_0}{4\pi} n_l B_{lu} \left(1 - \frac{g_l n_u}{g_u n_l} \right) \phi(\nu) \tag{2.34}$$

$$S_\nu = \frac{2h\nu^3}{c^2} \frac{1}{\left(\frac{g_u n_l}{g_l n_u} - 1\right)} \tag{2.35}$$

Finally, using Eq. 2.24 for both equations above, α_ν and S_ν become:

$$\alpha_\nu = \frac{h\nu_0}{4\pi} n_l B_{lu} \left[1 - e^{-h\nu/k_B T_{\mathrm{ex}}}\right] \phi(\nu) \tag{2.36}$$

$$S_\nu = B_\nu(T_{\mathrm{ex}}) \tag{2.37}$$

2.4.5 Optical Depth in terms of Einstein Coefficient

From above, Eq. 2.36 express the relationship between the absorption coefficient and the Einstein coefficients. Thus, using Eq. 2.11 with Eq. 2.36, the optical depth can be expressed as:

$$\tau_\nu = \frac{h\nu_0}{4\pi} N_l B_{lu} \left[1 - e^{-h\nu/k_B T_{\mathrm{ex}}}\right] \phi(\nu) \tag{2.38}$$

With $N_l = n_l s$ the column density. Then, in the LTE regime, the partition function Z can be defined. The partition function describes the statistical properties of a system in thermodynamic equilibrium. It is defined as:

$$Z = \sum_i g_i e^{-E_i/k_B T} \tag{2.39}$$

Then, the relative column density N_i, can be expressed as:

$$\frac{N_i}{N} = \frac{g_i e^{-E_i/k_B T_{ex}}}{Z} \tag{2.40}$$

Therefore, Eq. 2.38 can be rewritten using Eq. 2.40 as:

$$\tau_\nu = \frac{h\nu_0}{4\pi} N B_{lu} \left(1 - e^{-h\nu/k_B T}\right) \left[\frac{g_i e^{-E_i/k_B T_{ex}}}{Z}\right] \phi(\nu) \tag{2.41}$$

And using the Einstein coefficients relationships (Eqs. 2.28 and 2.29) in Eq. 2.41, the optical depth can be expressed as a function of the frequency as:

$$\tau_\nu = \frac{c^2}{8\pi\nu_0^2}\frac{g_u}{g_l}NA_{ul}\left(1 - e^{-h\nu/k_BT}\right)\left[\frac{g_ie^{-E_i/k_BT_{ex}}}{Z}\right]\phi(\nu) \tag{2.42}$$

Hence, using Eq. 2.20, the optical depth as a function of the Doppler velocity becomes:

$$\tau(v) = \frac{c^3}{8\pi\nu_0^3}\frac{g_u}{g_l}NA_{ul}\left(1 - e^{-h\nu/k_BT}\right)\left[\frac{g_ie^{-E_i/k_BT_{ex}}}{Z}\right]\phi(v) \tag{2.43}$$

2.5 Description of the Observed Atoms and Molecules

The study of the atom and molecular physics, quantum levels and line emission is an extensive field that will not be covered here in depth. The purpose of this section is to describe the atoms and molecules observed through fine structure line, hyperfine line structure line or rotational line transition that will be analyzed below in Chapter. 5. The atoms are ionized carbon, neutral carbon and ionized nitrogen. For the molecules, low-J carbon monoxide will be analyzed below. Extensive discussion over the subject, as well as some summaries, can be found in textbooks such as *Radiative Processes in Astrophysics* (Rybicki & Lightman 1979), *Tools of Radio Astronomy* (Wilson et al. 2009), *The Physics of Atoms and Quanta* (Haken & Wolf 2000) and *Molecular Physics and Elements of Quantum Chemistry* (Haken & Wolf 2004).

It is important to define first the description of the species, the basic terminology used in Astrophysics. The atomic element in neutral state is written as the species with an uppercase 0 (A^0), and in single ionized state as the element with an uppercase + (A^+). In Astrophysics, the transitions are named using the name of the species and successive Roman numbers. The atom with a number I refers to fine or hyperfine structure line transitions of the neutral atom (AI), the atom with a number II refers to transition for a single ionized atom (AII), and so on. If the transition is written between brackets ([ ]), it means that the transition is forbidden ($[AI], [AII]$,etc). Forbidden transitions are transitions that are unlikely to occur, requiring a longer time to happen. At first order, transitions are governed by electric dipole transitions, at second order, magnetic dipoles and electric quadropoles and so on at higher orders. Transition with no contribution from the electric dipole moment are forbidden. They are dominant, i.e. brighter, in space due to the extremely
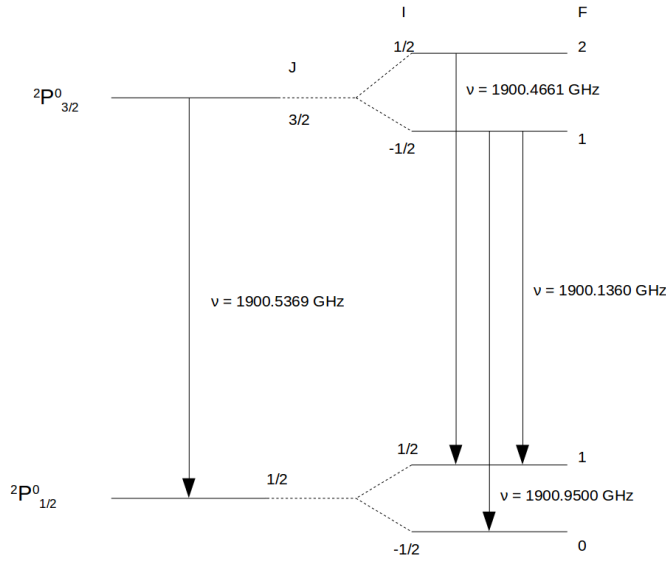
Figure 2.2: Fine-structure levels of C^+ and hyper-fine structure levels of $^{13}C^+$ (see also Table 2.1).

low gas density. This makes collision unlikely, allowing the gas to decay by emitting a forbidden-line photon.

2.5.1 $^{12}C^+$ and $^{13}C^+$ - Ionized Carbon

C^+ ground electronic state $1s^2 2s^2 2P^0$ is divided into two fine-structure levels $^2P^0_{1/2}$ and $^2P^0_{3/2}$, as we can see in Fig. 2.2. C^+ is excited to the $^2P^0_{3/2}$ level through collisions with electrons (Keenan et al. 1986; Blum & Pradhan 1991; Wilson & Bell 2002; Wilson et al. 2005), atomic hydrogen (Launay & Roueff 1977b; Barinovs et al. 2005) or molecular hydrogen (Flower & Launay 1977; Flower 1988), depending on whether the collision partner is available in the different layers of the PDR. The excitation is followed by a subsequent radiative decay to the $^2P^0_{1/2}$ level by spontaneous emission or collisions, producing a photon of frequency 1900.5369 GHz or 157.7 μm (Cooksy et al. 1986), see table 2.1 for the $[^{12}CII]$ spectroscopic parameters. [CII] fine structure line has a spontaneous emission probability of $A_{10} = 2.29 \times 10^{-6}$ s-1 (Mendoza 1983; Tachiev & Froese Fischer 2001; Wiese & Fuhr 2007).

$^{13}C^+$ is one of the isotopes of C^+. Due to the presence of an additional spin of the unpaired neutron in the nucleus, the two C^+ fine-structure levels are splitted into 4 hyper-fine structure levels, as we can see in Fig. 2.2. This hyper-fine splitting produces three components. These components are labeled by the total angular momentum change F=2→1, F=1→0 and F=1→1. Figure 2.3 illustrates the resulting spectrum for the case of a sufficiently narrow intrinsic line width, in such a way that

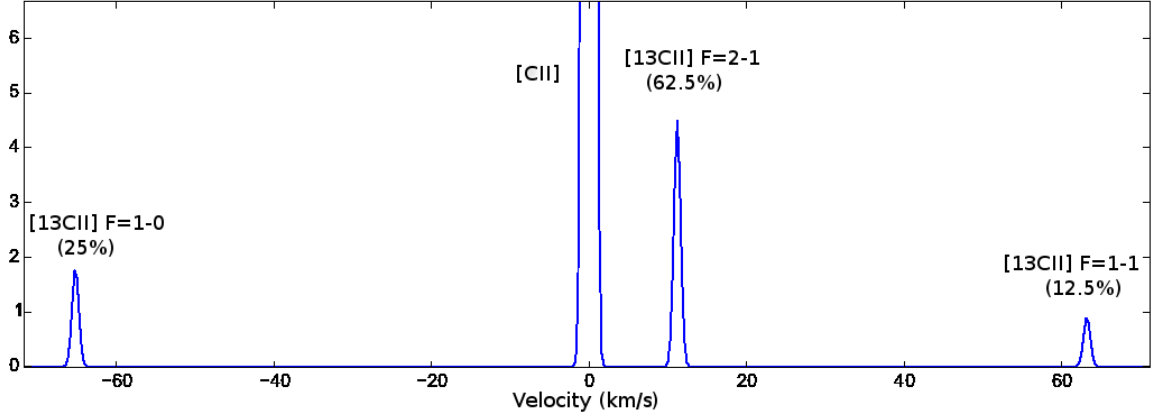Figure 2.3: Spectral signature of the [^{13}CII] hyperfine structure and [^{12}CII] for a hypothetical, narrow line width (see also Table 2.1).

Table 2.1: [^{12}CII] and [^{13}CII] Spectroscopic parameters

Line	Statistical g_u	Weight g_l	Frequency ν (GHz)	Vel. offset $\delta\, v_{F\to F'}$ (km/s)	Relative intensity $s_{F\to F'}$
[^{12}CII] $^2P_{3/2}-^2P_{1/2}$	4	2	1900.5369	0	—
[^{13}CII] F=2→1	5	3	1900.4661	+11.2	0.625
[^{13}CII] F=1→0	3	1	1900.9500	-65.2	0.250
[^{13}CII] F=1→1	3	3	1900.1360	+63.2	0.125

the strongest hyperfine satellite of [^{13}CII], F=2→1, does not blend with the [^{12}CII] line. The frequencies of the hyper-fine transitions were determined by Cooksy et al. (1986). Ossenkopf et al. (2013) confirmed that the hyper-fine frequencies were correct through direct astronomical observations, with an accuracy of 3 MHz. They also computed the relative line strengths of the [^{13}CII] hyperfine satellites and noted that the relative strengths given by Cooksy et al. (1986) were incorrect. The right ratios for the $F' - F = 2 - 1 : 1 - 0 : 1 - 1$ transitions are 0.625:0.25:0.125, and the old line ratios were 0.444:0.356:0.20. This anomaly had also been reported before by Graf et al. (2012).

The relevant [^{12}CII] and [^{13}CII] spectroscopic parameters are summarized in Table 2.1, including the velocity offsets of the [^{13}CII] hyperfine components relative to [^{12}CII]. The frequency separation of the hyperfine lines is small enough that all lines can be observed simultaneously with the bandwidth available in current, state-of-the-art high resolution heterodyne receivers, the 130 km/s separation of the outer hfs-satellites corresponds to slightly below 1 GHz frequency separation.

2.5.1.1 [CII] Optical Depth Estimation from the Main Beam Temperature ratio

For a direct estimation of the optical depth from the observed main beam temperature ratio, it can be assumed, as a first approximation, that the source is composed of a single, homogeneous layer. The optical depth is proportional to the line of sight integral of the population differences between the upper and lower states. We can estimate the ratio between the optical depth of [^{13}CII] and [^{12}CII] if two conditions are met: The chemical abundance ratio between ^{12}C$^+$ and ^{13}C$^+$, defined as ^{12}C$^+/^{13}$C$^+ = \alpha^+$, is constant across the source; and the excitation temperature of the main isotopic line and all three [^{13}CII] hyperfine satellites are identical at each position in the source.

Instead of calculating the [^{12}CII] optical depth for each [^{13}CII] hyperfine satellite separately, the noise weighted average is used, of the appropriate velocity shifted and scaled-up three hyperfine satellites:

$$
\mathrm{T_{mb,13,tot}}(v) = \frac{\sum_{F,F'} w_{F \to F'} \dfrac{\mathrm{T_{mb,13}}(v - \Delta v_{F \to F'})}{s_{F \to F'}}}{\sum_{F,F'} w_{F \to F'}}
$$

$$
w_{F \to F'} = \left(\frac{s_{F \to F'}}{\sigma} \right)^2
$$

(2.44)

with $s_{F \to F'}$ the relative intensities from Table 2.1 and σ is the rms noise level of the observation. The F, F'-sum in eq. 2.44 runs over all satellites that are not blended with the main [^{12}CII] line. From the radiative transfer equation from Eq. 4.13, the ratio between the temperatures of both isotopes can be expressed as:

$$
\frac{\mathrm{T_{mb,12}}(v)}{\mathrm{T_{mb,13,tot}}(v)} = \frac{1 - e^{-\tau_{12}(v)}}{1 - e^{-\tau_{13,tot}(v)}}
$$

(2.45)

Furthermore, the optical depth of [^{13}CII] is inversely proportional to the abundance ratio α^+ as:

$$
\tau_{13,tot}(v) = \beta_{tot} \, \tau_{12}(\nu)
$$

(2.46)

$$
\beta_{tot} = \frac{1}{\alpha^+} \sum_{F,F'} s_{F \to F'}
$$

(2.47)

If the three hyper-fine components are used $\beta_{tot} = 1/\alpha^+$, $s_{F \to F'}$ is the relative

intensity of the [^{13}CII] hyperfine satellite (Table 2.1). Combining Eq. 2.45 and 2.46, the [^{12}CII] optical depth can be estimated as:

$$\frac{\text{T}_{\text{mb},12}(v)}{\text{T}_{\text{mb},13,tot}(v)} \simeq \frac{1 - e^{-\tau(v_{12})}}{\beta_{tot}\,\tau(v_{12})} \tag{2.48}$$

2.5.1.2 [CII] Column Density and Optical Depth

For an atomic fine-structure level transition, the energy E_i is:

$$E_i = h\nu_i \tag{2.49}$$

To estimate the [^{12}CII] column density, the partition function Z from Eq. 2.39 for a two level system is:

$$Z = g_l e^{-h\nu_l/kT} + g_u e^{-h\nu_u/kT} \tag{2.50}$$

And the optical depth from Eq. 2.43 becomes:

$$\tau(v) = \frac{c^3}{8\pi\nu_0^3}\frac{g_u}{g_l}N A_{ul}\left[\frac{1 - e^{-h\nu/kT}}{1 + \frac{g_u}{g_l}e^{-h\nu_l/kT}}\right]\phi(v) \tag{2.51}$$

From here, the column density can be derived from the integrated intensity. This is calculated from the integration of the main beam temperature from Eq. 4.13 defined below in Chapter 4, assuming that the background contribution is negligible and approximating the optical depth as (1-e$^{-\tau}$) $\approx \tau$. Therefore, the integrated main beam temperature is:

$$\int T_{\text{mb}}(v)\,dv = \int \frac{h\nu_0}{k}\frac{1}{e^{h\nu_0/kT} - 1}\tau(v)\,dv \tag{2.52}$$

and replacing Eq. 2.42 into 2.52:

$$\int T_{\text{mb}}(v)\,dv = \frac{h\nu}{k}\frac{c^3}{8\pi\nu_0^3}A_{ul}N\frac{1}{1 + \frac{g_u}{g_l}e^{h\nu/kT}} \tag{2.53}$$

Rearranging Eq. 2.53 for the column density, becoming:

$$N(CII) = \frac{8\pi k\nu_0^2}{hc^3 A_{ul}}f(T)\int T_{\text{mb}}(v)\,dv \tag{2.54}$$

with $f(T) = 1 + \frac{g_l}{g_u}e^{h\nu/kT}$. In the high limit case for the temperature, if T goes to infinity, f(T) goes to 3/2. Higher values of f(T) occur at lower excitation temperatures. Therefore, a minimum column density can be defined for the high limit case as:

$$N_{\min}(CII) = \frac{3}{2}\frac{8\pi k\nu_0^2}{hc^3 A_{ul}}\int T_{\mathrm{mb}}(v)\,dv \qquad (2.55)$$

and the column density from Eq. 2.54 as:

$$N(CII) = \frac{2}{3}f(T)\,N_{\min}(CII) \qquad (2.56)$$

Figure 2.4 shows how the value of the excitation temperature affects the column density estimated from the integrated intensity, specially below the 91.2 K.
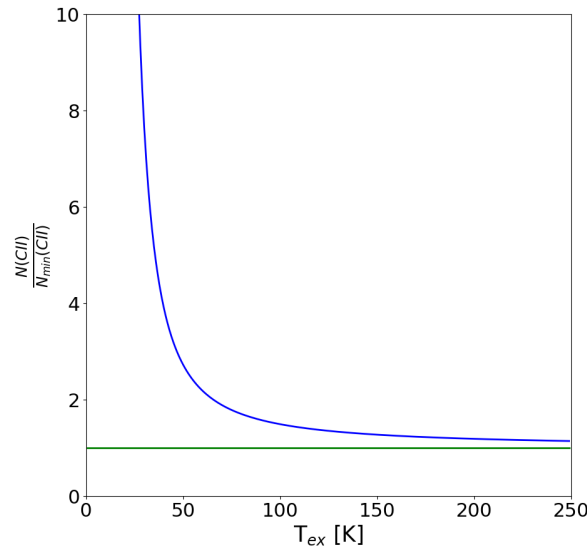
Figure 2.4: Ratio between N(CII) and $N_{\min}$(CII) as a function of the excitation temperature. Above the temperature of the [CII] transition, 91.2 K, the increase relative to the minimum value is well below a factor of 2.

2.5.2 C^0 - Neutral Carbon

Carbon ground electronic state is $1s^2 2s^2 2p^2$. The ground state is divided into three fine-structure levels $^3P_0$, $^3P_1$ and $^3P_2$ (Saykally & Evenson 1980), see Fig. 2.5 for the fine-structure level diagram.
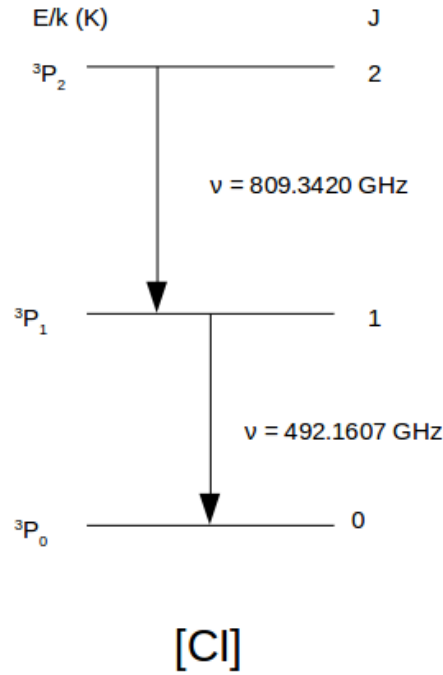
Figure 2.5: Fine-structure levels of atomic carbon

It is excited mainly by collisions with atomic hydrogen (Yau & Dalgarno 1976; Launay & Roueff 1977a; Abrahamsson et al. 2007), but also with He and H_2 (Monteiro & Flower 1987). [CI] $^3P_2$-$^3P_1$ transition emits a photon with a frequency of 809.3 GHz and a spontaneous emission probability of $A_{21} = 2.68 \times 10^{-7}$ s-1 and $^3P_1$-$^3P_0$ transition has a frequency of 492.2 GHz and a spontaneous emission probability of $A_{10} = 7.93 \times 10^{-8}$ s-1 (Draine 2011).

2.5.2.1 [CI] Column Density

From Gerin et al. (1998), the neutral carbon column density, under LTE conditions, is:

$$N(\text{C}) = 1.9 \times 10^{15} \int T_{\text{mb}} \, dv \, Q(T_{\text{kin}}) e^{E_1/kT_{\text{kin}}} \; (cm^{-2}) \qquad (2.57)$$

with the partition function $Q(T) = 1 + 3e^{-E_1/kT} + 5e^{-E_2/kT}$, carbon atom energy levels $E_1/k = 23.6$ K and $E_2/k = 62.5$ K, the integrated intensity in units of K km s^{-1} and T_{kin} the kinetic temperature of the carbon gas.

2.5.3 N^+ - Ionized Nitrogen

N^+ corresponds to ionized nitrogen. The atom has an ionization potential of 14.5 eV, higher than hydrogen. For this reason, it can be found in HII regions and in diffuse ionized gas, tracing the ionized hydrogen and reflecting the effects of the UV photons, as well as the electron density. N^+ is created mainly by UV photoionization, but also by cosmic rays and x-rays ionization, electron collisional excitation and proton charge exchange (Langer et al. 2015). It is depleted in fully ionized regions by electron radiative and dielectronic recombination, and in partially ionized regions also by exothermic charge exchange with atoms.
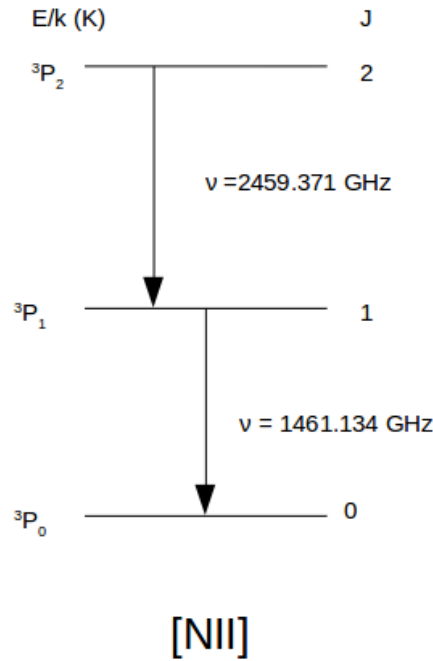
Figure 2.6: Fine-structure levels of ionized nitrogen N^+

N^+ in the ground electronic state is distributed as $1s^2 2s^2 2p^2$. Due to its electronic distribution, it is divided in three fine structure levels, similar to neutral carbon. $^3P_2$ has a E_j/k of 118 K with a $g_2 = 5$, $^3P_1$ has a E_j/k of 70 K with a $g_1 = 3$ and $^3P_0$ has a E_j/k of 0 K with a $g_0 = 1$. [NII] $^3P_2$-$^3P_1$ transition has a frequency of 2459.371 GHz (121.9 μm), meanwhile $^3P_1$-$^3P_0$ transition has a frequency of 1461.134 GHz (205.2 μm) (Brown et al. 1994). The spontaneous emission probability A_{21} corresponds to 7.5×10^{-6} s-1 and A_{10} to 2.1×10^{-6} s-1 (Galavis et al. 1997). It is excited through collision with electrons (Lennon & Burke 1994; Hudson & Bell 2004; Tayal 2011).

2.5.3.1 [NII] Column Density

From Langer et al. (2015), the [NII] column density can be estimated from the integrated intensity in the optically thin limit as:

$$I_{ul}([\text{NII}]) = \int T(K)\, dv = \frac{hc^3}{8\pi\nu_{ul}^2} A_{ul} f_u N(\text{N}^+) \tag{2.58}$$

where A_{ul} is the Einstein A coefficient for the transition, ν_{ul} the transition frequency, f_u is the fractional population of the upper state, $N(\text{N}^+)$ is the column density and the integrated intensity is in units of K km s^{-1}. For the 205 μm $^3\text{P}_1$-$^3\text{P}_0$ transition, it can be written as (Langer et al. 2015):

$$I_{ul}([\text{NII}]) = 5.06 \times 10^{-16} f_1 N(\text{N}^+) \, (\text{K km s}^{-1}) \tag{2.59}$$

with f_1 fractional population of N$^+$ in the $^3\text{P}_1$ state. The fractional population has the condition of $f_2 + f_1 + f_0 = 1$, with f_i the fractional population of the different levels. N$^+$ is excited by electron collision, therefore, the level populations depend directly from the electron density of the HII region. From Goldsmith et al. (2015), Fig. 2.7 shows how the population fraction for the different levels changes for a kinetic temperature of 8000 K.

If only the $^3\text{P}_1$-$^3\text{P}_0$ transition has been observed, it is not possible to derive the electron density. But assuming a kinetic temperature of 8000 K, the population fraction of the level $^3\text{P}_1$ peaks at 0.45 with an electron density of 100 cm^{-3}. Therefore, this value can be used to derive the column density as a lower limit.

2.5.4 CO - Carbon Monoxide Rotational Transitions

CO, carbon monoxide is a diatomic heteronuclear molecule. Diatomic molecules correspond to molecules formed by two atoms. Each electronic state can be defined by a vibrational quantum number v and a rotational quantum number J, that corresponds to the total angular momentum, that is the sum of the electronic angular momentum L and the angular momentum N. Heteronuclear diatomic molecules are molecules formed by different atoms, such as CO, OH or HD. They have a permanent electric dipole, hence vibrational and rotational transitions are allowed in the ground electronic state. The spontaneous emission coefficient A_{ul} is given by (Mangum & Shirley 2015):

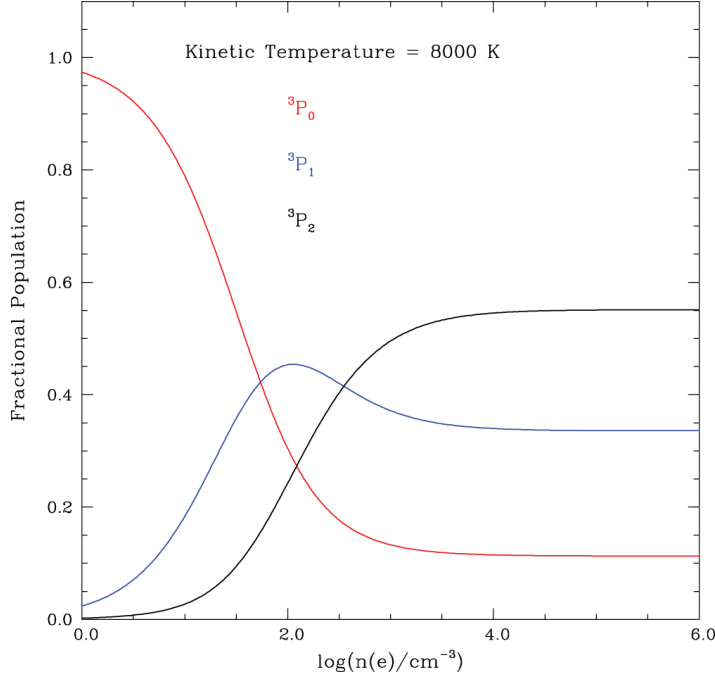$$A_{ul} = \frac{64\pi^4\nu^3}{3hc^3} |\mu_{lu}|^2 \tag{2.60}$$

Figure 2.7: Fractional populations of three N^+ fine structure levels for kinetic temperature of 8000 K, as a function of electron density. From Goldsmith et al. (2015)

with $|\mu_{lu}|^2$ the dipole matrix element. For a pure rotational transition in the ground electric and vibrational levels, from J to J-1, the dipole matrix element is:

$$|\mu_{lu}|^2 = \mu^2 \frac{J}{2J+1} \quad J \to J-1 \tag{2.61}$$

with μ^2 the permanent electric dipole moment of the molecule. The energy levels for the rotational transitions, using the rigid rotor approximation, are:

$$E_J = hB_0 J(J+1) \tag{2.62}$$

with B_0 the rigid rotor rotation constant. The partition function Z from Eq. 2.39 can be approximated for a diatomic molecule as (Schneider et al. 2016b):

$$Z_{\mathrm{mol}} = \sum_{J=1}^{\infty} (2J+1) e^{\frac{-E_J}{k_B T}} \sim \frac{k_B T_{\mathrm{ex}}}{hB_0} + 1/3 \tag{2.63}$$

CO has a permanent dipole moment of $\mu \approx 0.11 \times 10^{-18}$ esu cm, the ground rotational transition has rotational frequency B = $\nu/2/$J, $h^2/Ik \approx 5.5$ K and a critical density of 2200 cm^{-3}. The combination of these three conditions results in the CO being

easily excited, even in cold molecular clouds. CO is excited mainly through collision with H_2 and by radiative trapping (Scoville & Solomon 1974; Green & Thaddeus 1976). Radiative trapping means that the emission of excited CO is reabsorbed by an unexcited one, trapping the photons inside the cloud at large optical depths.

Also, the beam average total column density can be determined from the observed integrated main beam intensity as (Schneider et al. 2016b):

$$N = \frac{3hZ_{\mathrm{mol}}}{8\pi^3\mu^2 J} \frac{e^{E_J/kT_{\mathrm{ex}}}}{[1 - e^{-h\nu/kT_{\mathrm{ex}}}](J(T_{\mathrm{ex}}) - J(T_{\mathrm{BG}}))} \int T_{\mathrm{mb}}\, dv \ (cm^{-2}) \qquad (2.64)$$

with $J(T)$ the brightness temperature from Eq. 2.8, $T_{\mathrm{BG}} = 2.7$ K, J the upper rotational quantum number value of the transition and $\int T_{\mathrm{mb}}\, dv$ the velocity integrated line intensity in units of K km s^{-1}.

3 | Astrophysics

In this chapter, there is a discussion of the characteristics of the Photodissociation Regions, such as physical and chemical processes, regions that are part of them and the main atoms and molecules that form the gas on them. This description is a general review about this kind of regions and serves as an introduction to the subject. For more in-depth reviews, readers are invited to check artciles such as *Photodissociation regions. I - Basic model. II - A model for the Orion photodissociation region* (Tielens & Hollenbach 1985), *Dense Photodissociation Regions (PDRs)* (Hollenbach & Tielens 1997) and *Photodissociation Regions in the Interstellar Medium of Galaxies* (Hollenbach & Tielens 1999). There is a discussion also about the origin of the ^{12}C/^{13}C Isotopic Abundance Ratio and how it changes across the Galaxy. Finally, a description is given of the four PDR sources observed for this thesis work: M43, the Horsehead PDR, Monoceros R2 and M17. Their physical characteristics and observations that have been done before this work are described below.

3.1 Photodissociation Regions

A Photodissociation Region (PDR) is a region of the interstellar medium (ISM) where the structure, thermal balance and chemistry are dominated by Far-UV (FUV) photons that interact with the gas and dust of the region. The PDR is a transition region between the fully ionized to the dense molecular gas. The FUV photons are generated by nearby OB stars and they have energies between 6 eV and 13.6 eV (Tielens & Hollenbach 1985; Hollenbach & Tielens 1997, 1999). At lower energies, most atoms are not ionized and photoelectric in dust grains is negligible. At higher energies, hydrogen is ionized and it is not part of a PDR. The FUV average interstellar radiation is usually expressed in terms of the Habing field (Habing 1968) corresponding to:

$$G_0 \equiv \frac{u(6 - 13.6\,eV)}{5.29 \times 10^{-14}\,erg\,cm^{-3}} \tag{3.1}$$

with u(6-13.6 eV) the energy density between 6 and 13.6 eV. It can be expressed also in Draine units (Draine 1978), with $\chi = 1.71\,G_0$. The incident flux for a PDR

ranges from the local average interstellar radiation field (ISRF) of 1.7 G_0 (Draine 1978), which contains contributions from early-type stars from the Galaxy, to $G_0 \geq 10^6$.

The incident FUV field photodissociates molecules, photoionizes atoms and molecules and heats the gas and dust through photoelectric heating or direct absorption of photons. These mechanisms produce a layered structure, as shown in Fig. 3.1. Assuming that the incident FUV flux comes from the left, and going deeper into the cloud from left to right, the column density progressively increases and the temperature of the gas and dust decrease. Outside the PDR, there is the so-called HII region, where hydrogen is ionized by the incident FUV field, with gas temperatures~10^4 K and visual extinction (A_v) lower than 0.1 magnitudes. Due to the photoionization of hydrogen, all the photons with energy higher than 13.6 eV are absorbed, creating an ionization front, separating the HII region from the PDR itself and forming a layered structure. Additionally, species with a ionization potential higher than hydrogen become completely neutral inside the PDR, such as nitrogen (14.5 eV) or oxygen (13.6 eV), and species with a ionization potential lower than H are photoionized inside the PDR, such as carbon (11.3 eV).

3.1.1 H/H_2 Transition Zone

Thus, inside the PDR, the gas temperature in the outer layers ranges from 10^2 to 10^3 K. The abundance of atomic hydrogen is kept in equilibrium between the reduction of atomic hydrogen through the formation of molecular hydrogen (H_2) on the surface of dust grains, and the increase of it through the photodissociation of H_2 by the absorption of FUV photons in the Lyman and Werner transitions in the 912 to 1100 Å wavelength range, pumping H_2 to a bound excited electronic state. This absorption is followed by fluorescence back to an excited vibrational state in the ground electronic state, and leads to dissociation only 10% of the time. The electronic excited H_2 dissociates through reactions with atoms such as C^+ or O or collisions with H or H_2 to overcome the activation barrier and fluorescence back to the vibrational continuum and then dissociate.

When the molecular hydrogen column density increases ($> 10^{14}$ cm^{-2}), H_2 becomes optically thick and self-shields Lyman and Werner transitions. This allows for an increase of H_2, helped by the progressive attenuation of the FUV radiation by dust grains. Therefore, the photodissociation rate depends on the H_2 abundance and level population as a function of the depth in the cloud. Therefore, an H/H_2 transition zone or dissociation front appears, with a sharp profile at $A_v \sim 1 - 2$
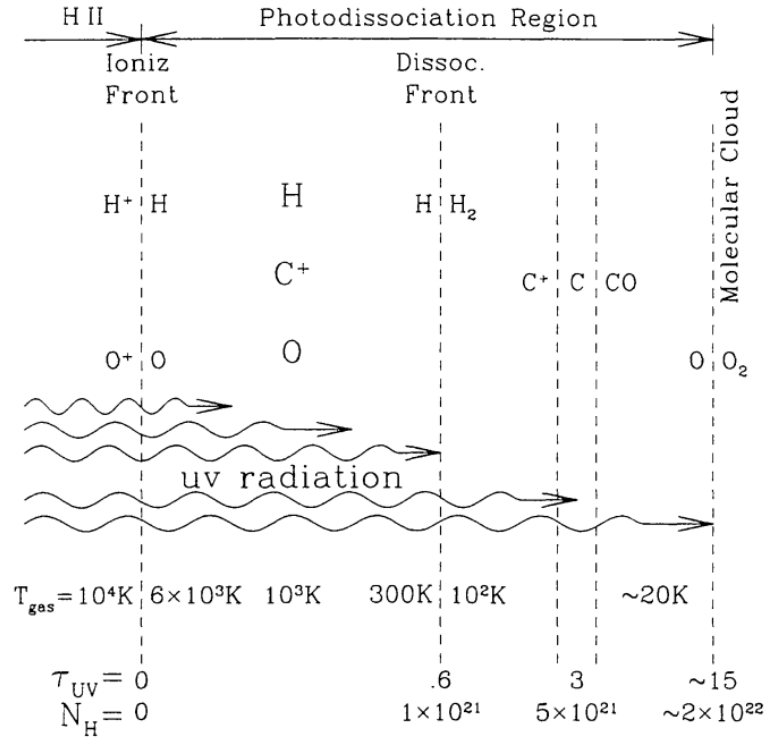
Figure 3.1: Photodissociation region structure. In the scheme, the FUV radiation comes from nearby OB stars to the left. The PDR starts from the ionization front, goes through the atomic region and ends inside the the molecular cloud (Draine & Bertoldi 1999).

magnitudes. Due to the self-shielding, the H/H_2 transition is located closer to the ionization front than the $C^+/C/CO$ or O/O_2 transition fronts.

3.1.2 C^+/C/CO Transition Zone

Deeper into the cloud, there is a C^+/C/CO transition region with temperatures between 10 and 100 K. Fig. 3.2 shows the complex chemical network of carbon. In general, the networks are complex systems with a large number of species playing a role in the formation and destruction of different atoms and molecules, depending on the physical conditions of the gas, such as density, column density, incident FUV flux and others.

Here, a description is offered of the atoms and molecules observed for this thesis and their main mechanisms of formation and destruction. This transition region can present a layered structure, when the gas is not extremely clumpy, with the ionized carbon (C^+) closer to the ionization front, carbon (C) present in the intermediate
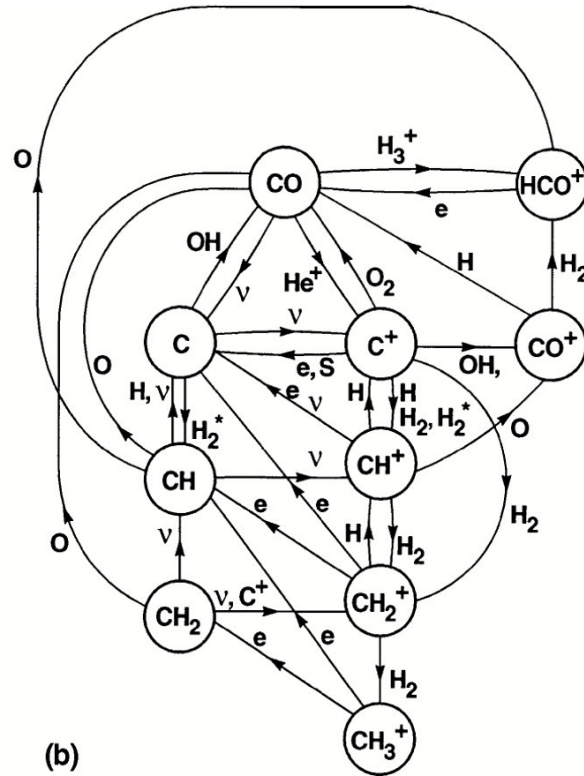
Figure 3.2: PDR chemical network with the most important reaction from the carbon-bearing compounds (Hollenbach & Tielens 1997).

layer and carbon monoxide (CO) in the last layer. The abundance of C^+ decreases with the deepness of the cloud. The transition region takes place due to a competing process between the recombination of C^+ into neutral carbon (C) or carbon monoxide (CO), and the photoionization of C into C^+.

C^+ corresponds to ionized carbon and is created through photoionization of carbon, with an ionization potential to overcome of 11.2 eV (Tielens & Hollenbach 1985). Due to its low ionization potential, compared to hydrogen, it is abundant in HII regions and in the UV illuminated surface of atomic and molecular clouds.

$$C + h\nu \rightarrow C^+ + e^- \tag{3.2}$$

The dominant reactions of destruction of C^+ are through radiative recombination into C with the abundant free electrons located closer to the ionization front. Much deeper, the main mechanism is radiative association with H_2 (Röllig et al. 2006), this lead to the formation of CH or CH_2, which reacts with O and produces CO.

$$C^+ + e^- \rightarrow C + \nu \tag{3.3}$$

$$C^+ + H_2 \rightarrow CH^+/CH_2^+ + \nu \tag{3.4}$$

It is also important to name $^{13}C^+$, even if its abundance is low compared to the other species, but, is a key atom studied for this thesis. $^{13}C^+$ plays a role in the isotopic exchange reaction that forms ^{13}CO (Watson et al. 1976; Smith & Adams 1980; Langer et al. 1984), being inversely proportional to each other as seen below:

$$^{13}C^+ + {}^{12}CO \rightleftarrows {}^{13}CO + {}^{12}C^+ + \Delta E(35K) \tag{3.5}$$
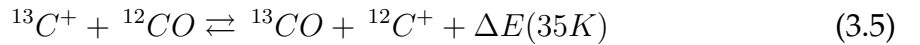
At high temperatures, both reactions are equally probable, but when the temperature decreases below 35 K, the back reaction becomes less likely. This would lead to fractionation, as explained below (Sect. 3.2).

In parallel, carbon (C^0) is formed and destroyed simultaneously. It is found in PDRs and is abundant in HI regions. Carbon plays an important role as a key component in the chemical network for the formation of molecules as CO. Carbon is formed by the reionization of C^+ (Eq. 3.3), charge exchange with sulfur (S) and photodissociation of CO (Röllig & Ossenkopf 2013):

$$C^+ + S \rightarrow C + S^+ \tag{3.6}$$

$$CO + h\nu \rightarrow C + O \tag{3.7}$$

Deeper into the cloud, where the abundance of electrons drops, carbon is formed by charge exchange reactions with sulfur and SiO (Tielens & Hollenbach 1985):

$$C^+ + S \rightarrow C + S^+ \tag{3.8}$$

$$C^+ + SiO \rightarrow C + SiO^+ \tag{3.9}$$

At low A_v, carbon is destroyed through photoionization by the UV field, forming C^+ (Eq. 3.2). Deeper into the cloud, carbon turns into carbon monoxide through

the neutral-neutral exchange reactions with OH and O_2. The last reaction becomes dominant deeper due to a decrease in the ionization rate of OH. This leads to an increase of CO much deeper into the cloud and it is one of the main mechanisms of CO formation:

$$C + OH \rightarrow CO + H \tag{3.10}$$

$$C + O_2 \rightarrow CO + O \tag{3.11}$$

In PDRs, CO is formed in different ways (Tielens & Hollenbach 1985). At the edge of the cloud, it can be formed by the radiative association of C^+ with H_2, they form CH and CH_2 (Eq. 3.4), the latter molecules react with O and form CO.

$$CH_2^+ + O \rightarrow CO + H^+/H_2^+ \tag{3.12}$$
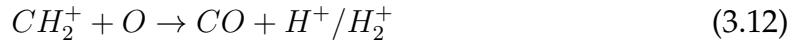
Deeper into the cloud, C^+ reacts with SiO and forms CO. Another way is by the reaction of OH with C^+ or C, to form CO, as well as many other routes. CO has a dissociation energy of 9.6 eV and at the edge of the cloud is destroyed mainly by photodissociation (van Dishoeck & Black 1988; Visser et al. 2009), and deeper into the cloud, it is destroyed by reactions with He^+ and H_3^+ and collisions.

$$CO + He^+ \rightarrow C^+ + O + He \tag{3.13}$$

$$CO + He_3^+ \rightarrow HCO^+ + H_2 \tag{3.14}$$

All these competing processes form a C^+/C/CO layered structure, less sharp than the H/H_2 transition zone.

3.1.3 Heating and Cooling

The dominant gas cooling process in PDRs is through collisional excitation and then FIR fine structure line emission of abundant atoms in the PDR, such as [CII] at 158 μm, [OI] at 63 and 145 μm or to a lesser extent [SiII] at 35 μm and [CI] at 370 and

609 μm. Main collisional partners are electrons located closer to the ionization front, atomic and molecular hydrogen. The collisions subtract kinetic energy from the gas, exciting electrons in the atoms to higher energy levels. Other processes, less important, are absorption of FUV photons by H_2 resulting in rovibrational transitions emission, and emission of molecular rotational lines, in particular CO. Both processes happen deeper into the cloud at higher densities than the [CII] fine structure emission.

For heating, the main two mechanisms are heating by photoelectric effect on PAHs (Polycyclic Aromatic Hydrocarbons) and small dust grains, and FUV pumping of H_2 molecules. The photoelectric heating is produced by FUV photons that hit the surface of the PAHs and create energetic electrons of several eV. For grains, the FUV photons are absorbed inside the grains, producing photoelectrons that diffuse through the grain due to collisions or escape from the grains. These electrons are injected into the gas with an excess of kinetic energy. The heating process is dominated by small grains (<50 Å). For large grains, the photoelectrons rarely escape, because the photons are absorbed deeper into the grain ($\sim$100 Å) and for the photoelectrons, it is much harder to escape due to the grain size. PAHs also play a role in the photoelectric heating, but they are less efficient in heating than small grains. They are limited by their ionization potential, that sometimes can be larger than 13.6 eV; so, absorbed photons do not produce photoelectrons. The photoelectric heating efficiency depends also on the charge of the grain. The higher the charge, the higher the ionization potential to overcome. This leads to neutral grains and PAHs as much more efficient heaters than positively charged ones. Larger grains in the ISM tend to be positively charged, whereas, small grains are neutral.

The other heating mechanism named above is the absorption of FUV photons by H_2. Part of this mechanism is the same that photodissociates the molecule. The absorption will pump the molecule to a bound excitation state. From there, 10-15% of the time, the molecule will fluoresce back to the vibrational continuum of the ground electronic state and dissociate. The rest of the time, it will fluoresce back to an excited vibrational state. At high densities ($>10^4$ cm^{-3}), it will heat the gas through collisional excitation with atomic hydrogen and to a thermalization of the rovibrational states. Other mechanisms are photoionization of atoms and molecules, where the electron removes some photon energy in the form of kinetic energy; dust-gas heating, due to the difference in temperature between them, only if the dust is warmer than the gas (if not, it is a cooling process), and cosmic-ray heating due to the ionization by cosmic-rays emission.

3.1.4 Numerical Models

A series of theoretical models have been developed over the last 30 years to infer the PDRs physical condition. This is done through numerical simulations to describe physical and chemical processes using different setups for it. A good summary of how the PDRs codes works and a comparison between them can be found in an article by Röllig et al. (2007). The models solve the radiative transfer equation for the dust and gas in a cloud, the chemical balance of formation and destruction for the different species included in them and the thermal balance of heating and cooling in the cloud. Most models are steady-state, static PDR models, which assume thermal and chemical balance and ignore any flow through the PDR. The assumed model geometry is a key input for the models; in general, one of the two approaches is plane parallel geometry, with a source illuminating from one or both sides. This simplifies the radiative transfer equation and easily generates a layered structure. Some models are the Meudon Code (Le Petit et al. 2006), CLOUDY (Ferland et al. 1998; Shaw et al. 2005) or the PDR Toolbox (Kaufman et al. 2006; Pound & Wolfire 2008). The other approach is the assumption of a spherical cloud that even allows for clumpy clouds with codes such as the KOSMA-τ model (Röllig et al. 2006). The numerical models are an important tool to derive the physical properties of the cloud using the observed data.

3.2 ^{12}C/^{13}C Isotopic Abundance Ratio

^{12}C and ^{13}C are formed by different processes and environments. Comprehensive reviews of isotopes abundance in the interstellar medium are Wilson & Matteucci (1992) and Wilson (1999), with detailed description of the formation of both carbon isotopologues and nucleosynthesis in stars. ^{12}C is produced mainly in high mass stars (M> 6 M$_\odot$) as a primary product. The massive stars burn helium and transform it into carbon through the triple alpha process (Burbidge et al. 1957; Timmes et al. 1995), where three alpha particles (^{4}He nucleus) combine to form a carbon nucleus. The carbon is then expelled through supernova explosions. ^{13}C is principally produced from ^{12}C as an intermediate step of the carbon-nitrogen-oxygen (CNO) cycle (Wilson & Matteucci 1992; Wilson 1999) in intermediate mass AGB stars (1.5-6 M$_\odot$). The ^{13}C is later ejected into the ISM through solar winds.

The timescales required to produce ^{13}C are much longer than the ones for ^{12}C. This difference causes an imbalance in the isotopic ratio between ^{12}C and ^{13}C. Hence, the ^{12}C/^{13}C elemental isotopic ratio (α) decreases with time. On the other hand,

there is a positive gradient for α in the galactic disk, that increases with the galacto-centric distance (Wilson & Matteucci 1992). This can be understood as a reduction of ^{12}C and an increment of ^{13}C due to the cycle of enrichment of the interstellar gas with metals by stars of all masses over the life of the Galaxy. The star formation rate (SFR) and the star population concentrate in the galactic center and the inner spiral arms, and because the star formation started before in the center of the Galaxy, there has been enough time for an increase of the ^{13}C. Therefore, α decreases with time and increases with galactocentric distance.

The ^{12}C/^{13}C elemental isotopic ratio has been studied for several decades (e.g. Penzias 1980; Langer et al. 1984; Güsten et al. 1985; Henkel et al. 1985; Langer & Penzias 1990, 1993; Wilson & Rood 1994; Wouterloot & Brand 1996; Savage et al. 2002; Milam et al. 2005; Giannetti et al. 2014). The common approach has been to derive the ratio from the comparison of ^{12}C and ^{13}C line intensities of common molecules containing carbon such as CO, H$_2$CO or CN. The studies show in all cases that α increases with Galactic radius. Milam et al. (2005), by compiling CO and H$_2$CO and CN data, derive a common galacto-centric gradient according to:

$$\alpha = 6.21(1.00)D_{\mathrm{GC}} + 18.71(7.37) \; [\mathrm{kpc}] \tag{3.15}$$

where D_{GC} is the galacto-centric radius.

Another effect that may arise is chemical fractionation. Chemical fractionation can be understood as a change in the isotopic abundance ratio due to the action of the interstellar chemistry. This occurs because of the difference between isotopes in the zero-point vibrational energy of their relative nucleus masses. The differences are small, of the order of $\sim 10^{-2}$ eV, but they affect the way chemical reactions work, specially at low temperatures (Wilson & Matteucci 1992). The charge exchange reaction described in Eq. 3.5, that involves ^{13}C$^+$ and CO, becomes more efficient for the forward reaction at low temperatures. This would lead to an enrichment of ^{13}C, shifting ^{13}C$^+$ into ^{13}CO, with a decrease of the ^{12}CO/^{13}CO chemical abundance ratio and an increment of the ^{12}C$^+$/^{13}C$^+$ (α^+) ratio (Woods & Willacy 2009; Röllig & Ossenkopf 2013). Ionized carbon can be found in the outer parts of the PDR, hence this reaction should not affect molecules in dense cores; however, in a clumpy medium, with small clumps and large surface area, chemical fractionation could arise.

3.3 PDRs Sources

For this thesis work, a wide range of PDRs sources have been observed in the Galaxy. For the original project, six PDRs sources were observed in [^{12}CII] fine structure and [^{13}CII] hyper-fine structure line emission using the SOFIA/upGREAT receiver : M43, the Horsehead PDR, DR21, S106, Monoceros R2 and M17. DR21 and S106 were partially observed and the rms noise levels were too high for an analysis. The sources were selected covering a wide range of physical conditions, from the low density, single ionizing source and simple geometry of M43, to the complex, massive, cluster ionized source and clumpy structure of M17. The objective was to study the [^{12}CII] and [^{13}CII] in different environments and study their similarities and differences between them. As an additional project, a large scale map of [CI] $^3P_1$-$^3P_0$ was observed using the NANTEN2/SMART receiver in M17. In this section, there is a description of the physical properties and observational history of the four sources analyzed in this thesis: M43, the Horsehead PDR, Monoceros R2 and M17.

3.3.1 M43

M43 is a close-by ideal spherical nebula conformed by a relatively dust-free HII region with an exciting star in the center (Thum et al. 1978; Smith et al. 1987). The region has a circular shape and is obscured by a small and dense molecular cloud (Hanel 1987). M43 is located northeast of the Orion Nebula or M42 (Goudis 1982). It is part of the Orion complex and has a distance of 389 pc (Kounkel et al. 2018). The region has one single ionizing source, an early B type star HD37061 or NU Ori (Abt et al. 1991; Preibisch et al. 1999; Simón-Díaz et al. 2011). A dust lane formed by a wall of dense material separates M43 from Orion (Khallesse et al. 1980). Therefore, M43 is isolated from the ionizating photons coming from the Trapezium cluster of M42 and it is only affected by HD37061.

M43 was first observed by an heterodyne instrument at 408 MHz by Mills & Shaver (1968). Dust emission was observed by Smith et al. (1987) between 28 and 180 μm and CO and ^{13}CO J=1-0. They estimated dust temperatures $\sim$ 45 K and confirmed NU Ori as the primary source of excitation for the dust, and a density of 4000 cm^{-3} for a mixture of dust and gas. Subrahmanyan (1992) studied the region at 330-MHz radio continuum and concluded that the region is a spherically symmetric HII region with an electron temperature of 9000 K. It has been studied also at optical wavelengths and through spectrography at those wavelengths (O'Dell 2001; Smith et al. 2005; O'Dell & Harris 2010; Simón-Díaz et al. 2011). Due to its close distance, its simple spherical geometry and a single ionization source, M43 is well suited as a

simple, properly characterized test case for the present study.

3.3.2 The Horsehead PDR

The Horsehead nebula is a dark cloud filament protruding out of the Orion Molecular Cloud complex (Abergel et al. 2003) and is visible in the optical against the prominent Hα emission of the large-scale ionized surface of the Orion Molecular Cloud complex. The region is located at a distance of 360 pc (Gaia Collaboration et al. 2016). The cloud features a PDR with an edge-on geometry that corresponds to the illuminated edge of the molecular cloud L1630 on the near side of the HII region IC 434. It is illuminated by two OB systems, ζ Ori and σ Ori, with a moderate far-UV intensity of ~100 (Reipurth & Bouchet 1984), and a projected distance between σ Ori and the nebula of 3.2 pc (Ochsendorf et al. 2014). It was studied in [CII] by Zhou et al. (1993) and CO and ^{13}CO by Kramer et al. (1996). Philipp et al. (2006) studied the nebula in CI (1-0) and CO (4-3) using the CHAMP array.

More recently, it was the target of an extended molecular line survey with the IRAM 30-m telescope (Guzmán et al. 2012; Pety et al. 2012; Gratier et al. 2013; Guzmán et al. 2013) and IRAM PdB (Guzmán et al. 2015). Lately, an extensive [^{12}CII] map was observed by upGREAT/SOFIA as part of the SOFIA Director's Discretionary Time and these data are publicly available [1] and it has been started to be used for analysis (Pabst et al. 2017; Bally et al. 2018). Pabst et al. (2017) estimated a gas mass of 3 M$_\odot$ and a gas density for the molecular cloud of 4×10^4 cm^{-3}for the Horsehead PDR. The Horsehead PDR with its simple edge-on geometry is an excellent source for studying the PDR structure resulting from the penetration of the UV field into the molecular cloud.

3.3.3 Monoceros R2

Monoceros R2 (Mon R2) is an ultra compact HII region located at 830 pc (Racine 1968; Herbst & Racine 1976). The region contains a reflection nebula and the UCHII region is surrounded by several PDRs with different physical conditions (Pilleri et al. 2014; Treviño-Morales et al. 2014). R2 refers to the 2nd reflection nebula. IRS1 is the main ionizing source (Choi et al. 2000) with a high UV field G$_0$ > 10^5 (Rizzo et al. 2003). The region can be seen as spherical concentric layers involving IRS1.

---

[1]https://www.sofia.usra.edu/science/proposing-and-observing/
proposal-calls/sofia-directors-discretionary-time/horsehead-nebula
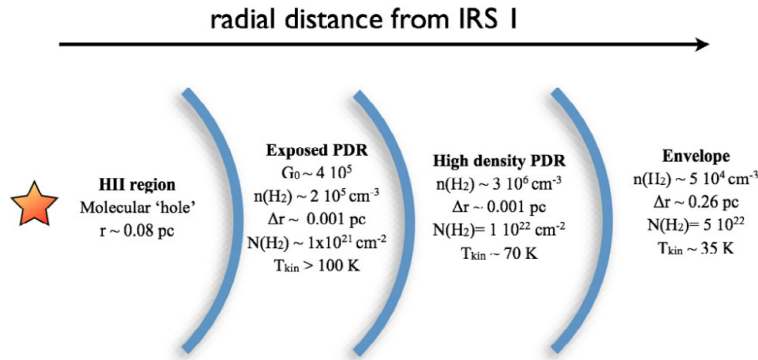
Figure 3.3: Schematic of the geometry of Mon R2 with the physical parameters of each layer, as a function of the distance from IRS1. From Pilleri et al. (2013).

A schematic of the geometry of Mon R2 from Pilleri et al. (2013) can be seen in Fig. 3.3. The geometry was derived from previous observations and modeling by Pilleri et al. (2012). They model the gas deriving the physical conditions of the gas analyzing the velocity and the physical distribution of the emission and their intensity. The HII region is an envelope around the star with no molecular gas and it expands at 10 km s^{-1} (Choi et al. 2000). The next layer is an exposed PDR ionized directly by IRS1 with a density $\sim 10^5$ cm^{-3} and a kinetic gas temperature of 100 K (Berné et al. 2009). Inside the PDR, the kinetic temperature is 70 K with a high density $\sim 10^6$ cm^{-3} (Rizzo et al. 2003). The molecular cloud is also illuminated by external sources from the outside with a $G_0 = 100$ (Pilleri et al. 2012). First observations in CO (1-0) were done by Loren et al. (1974). Over the last years, Mon R2 has been extensively studied using Spitzer/IRS, Herschel/HIFI and IRAM 30m/EMIR, covering a wide range of atomic and molecular lines (Berné et al. 2009; Pilleri et al. 2012, 2013; Ossenkopf et al. 2013; Treviño-Morales et al. 2014, 2016).

3.3.4   M17

M17 is one of the brightest and most massive star forming regions in the Galaxy. The M17 complex is located at a distance of 1.98 kpc. Xu et al. (2011) determined the distance to the complex through the observation of CH$_3$OH 12 GHz masers and used trigonometrix parallaxes to accurately estimate the distance. M17 is associated with the cluster NGC 6618, a highly obscured cluster (Av>10) with more than 100 OB stars ionizing the ISM (Beetz et al. 1976; Hoffmeister et al. 2008) and relatively young age (≤ 1 Myr) (Lada et al. 1991). The massive binaries CEN1 (Kleinmann 1973) are part of the cluster. CEN1 is formed by 2 O4 visual binary stars and they seem to be the main ionization source of the complex (Hoffmeister et al. 2008). Due to its youth, no supernova explosion has happened yet.

Lada et al. (1974) observed ^{13}CO and C^{18}O toward the complex and detected two *bright spots* of CO emission, one to the southwest of the optical nebula and a second, less bright, to the north. Therefore, the complex can be split into two regions, M17 North (M17 N) and M17 Southwest (M17 SW).

M17 N is located 10′ north of the exciting stars and it has not been studied much. More recently, it has been studied through continuum infrared observations (Henning et al. 1998; Klein et al. 1999), dust continuum at 850 and 450 μm (Reid & Wilson 2006) and large scale maps of the whole M17 complex of different CO transition lines and isotopologues (Wilson et al. 1999, 2003; Nishimura et al. 2018), JHKs imaging polarimetric observations (Chen et al. 2012) and X-rays emission (Broos et al. 2007). The density ranges between 10^4-10^5 cm^{-3}. The region seems to be externally ionized by the nearby cluster.

M17-SW is located in the southwestern side of the M17 complex and contains the nearby UCHII region (Felli et al. 1984; Chini et al. 2000) and it has been considered as a prototype of an edge-on interface. The large-scale, simple edge on geometry is much more complex on smaller scales. The M17 SW interface has a highly clumpy structure, proven by several studies of ionized, atomic and molecular emission (Stutzki et al. 1988; Genzel et al. 1988; Stutzki & Güsten 1990; Meixner et al. 1992; Snell et al. 2000; Pérez-Beaupuits et al. 2010, 2012, 2015b,a). The large extent of the [CII] emission, evident since the first observations of [CII] (Russell et al. 1981), has been successfully interpreted as being due to UV penetration between clumps (Stutzki et al. 1988). The high column densities involved across this complex source make it an ideal testbed for optical depth studies. In fact, early observations of the neutral atomic carbon fine structure line intensity in correlation with rare isotopic CO emission have been interpreted as evidence for moderate optical depth in this otherwise optically thin fine structure line (Genzel et al. 1988).

The gas clumps near the HII region/molecular cloud interface seems to be distributed in high density clumps ($< 10^5$ cm^{-3}) encapsulated in interclump material ($\sim 10^3$ cm^{-3}) surrounded by diffuse gas (~ 300 cm^{-3}), embedded in the strong UV field from the exciting cluster, which is estimated to provide a UV field of G$_0$= 5.6x10^4 (Meixner et al. 1992). Pérez-Beaupuits et al. (2015a) fitted the line spectral energy distribution (SED) of the CO, HCN and HCO$^+$ species for a molecular gas model divided into two layers. The results were a cold layer with a density of $\sim 6 \times 10^4$ cm^{-3} and a warm layer with densities as high as 10^6 cm^{-3}. Additionally, Pérez-Beaupuits et al. (2015b) detected that at least 64% of [CII] is not associated with molecular or

atomic emission traced by [CI] and $C^{18}O$ lines. The structure of the neutral and molecular gas are also affected by magnetic fields, with an intensity as high as $\sim$ 500 μG (Brogan et al. 1999; Brogan & Troland 2001). Due to the high magnetic fields, Pellegrini et al. (2007) proposed that the regions is dominated by magnetic pressure rather than gas pressure, increasing the column density and amplifying the local cosmic-ray density.

M17 presents an interesting case of study because is one of the most prominent and bright HII region-molecular cloud complexes. The high density and UV radiation field are a good example of massive and extreme regions. Also, it is a prime case of star formation triggered by the compression of the gas due to the expansion of the HII region. It is an ideal source for studying the clumpy structure of the molecular cloud, from the ionizing source to the atomic gas and into the molecular cloud. The high densities suggest optical depth effects and it is a good candidate for studying the physical conditions of the cloud and to extrapolate them to extra-galactic conditions.

4 | Radio Astronomy

In this chapter, there is a general discussion of how the telescopes are involved in the observations, detailing the temperature scales when dealing with observations from a telescope, as well as the efficiencies related to these temperatures. We describe the observational history of [^{12}CII] and [^{13}CII] and the telescopes involved through history with these observations. Finally, there is a description of the receivers used during the observations for this thesis and the observational strategies for each source and receiver.

4.1 Temperature Scales and Telescope Efficiencies

In this section,basic concepts regarding the temperature scales and the telescope efficiencies are explained. Extensive discussion about the subject can be found in *Recommendations for calibration of millimeter-wavelength spectral line data* (Kutner & Ulich 1981), *Calibrations of spectral line data at the IRAM 30m radio telescope, Version 2.1, January 24th* (Kramer 1997) and *Tools of Radio Astronomy* (Wilson et al. 2009).

An antenna is a device that converts electromagnetic radiation into electrical currents or vice-versa. A radio telescope is a receiving antenna. An antenna pattern is characterized by a power pattern $P(\upsilon, \varphi)$. The power pattern is not a single perfect beam, but instead, is composed by a main lobe, where most of the reception is focused, side near lobes that contributes to the reception and weaker far side lobes that can be represented as noise. A power pattern diagram is shown in Fig. 4.1.

The normalized power pattern is defined as:

$$P_{\mathrm{n}}(\upsilon, \varphi) = \frac{P(\upsilon, \varphi)}{P_{\max}} \tag{4.1}$$

From here, the beam solid angle (Ω_{A}) can be defined as the power pattern integrated over the full sphere, the main beam solid angle (Ω_{mb}) as the power pattern integrated over only the main beam lobe, the forward beam solid angle (Ω_{f}) as the
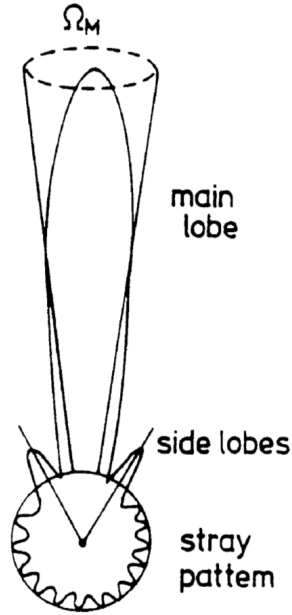
Figure 4.1: Power beam pattern in polar coordinates showing the main lobe, near side lobes and weaker far side lobes in a stray pattern. From *Tools of Radio Astronomy* (Wilson et al. 2009)

power pattern integrated over the forward side of the telescope and the diffraction pattern solid angle (Ω_D) as the power pattern integrated over the solid angle subtended by the central diffraction beam pattern of the telescope:

$$\Omega_A = \iint_{4\pi} P_n(v, \varphi) d\Omega \tag{4.2}$$

$$\Omega_{mb} = \iint_{mainlobe} P_n(v, \varphi) d\Omega \tag{4.3}$$

$$\Omega_f = \iint_{2\pi} P_n(v, \varphi) d\Omega \tag{4.4}$$

$$\Omega_d = \iint_{diffpattern} P_n(v, \varphi) d\Omega \tag{4.5}$$

From the equations above, the main beam efficiency (η_{mb}) and the forward beam efficiency (η_{fss}) can be defined as:

$$\eta_{\text{mb}} = \frac{\Omega_{\text{mb}}}{\Omega_{\text{f}}} \tag{4.6}$$

$$\eta_{\text{fss}} = \frac{\Omega_{\text{d}}}{\Omega_{\text{f}}} \tag{4.7}$$

The main beam efficiency can be estimated from continuum observations of planets, whose disk radiation temperature is known and their angular diameter fills the beam. The forward beam efficiency is measured from very extended source like the moon.

Now, the antenna temperature (T_{A^*}) can be defined as the convolution between the Rayleigh-Jeans brightness temperature T_b (defined in Sect. 2 Eq. 2.9) and the power beam pattern of the telescope. Basically, this is the temperature of the source observed by the telescope:

$$T_{\text{A}}^*(\upsilon, \varphi) = \frac{1}{\Omega_{\text{A}}} \iint_{4\pi} P_{\text{n}}(\upsilon - \upsilon', \varphi - \varphi') T_b(\upsilon', \varphi') \text{d}\Omega' \tag{4.8}$$

The forward beam antenna temperature ($T_{\text{A}}^*\prime$) can be defined as the equivalent temperature of a source that fills completely the forward side of the telescope pattern:

$$T_{\text{A}}^{*\prime} = \eta_{\text{fss}} T_{\text{A}}^* \tag{4.9}$$

And the main beam temperature can be defined as the equivalent temperature of a source that fills the main beam telescope pattern completely as:

$$T_{\text{mb}} = \frac{1}{\eta_{\text{mb}}} T_{\text{A}}^{*\prime} \tag{4.10}$$

If the source size is smaller than the beam size, beam dilution happens. The beam dilution decreases the observed intensity of the source. If a source temperature with temperature T_{s} and solid angle Ω_{s} is observed by a telescope with a beam solid angle Ω_{mb}, the observed temperature (T_{o}) is:

$$\Omega_{\text{s}} = \iint_{source} P_{\text{n}}(\upsilon, \varphi) \text{d}\Omega \tag{4.11}$$

$$T_{\mathrm{o}} = \frac{\Omega_{\mathrm{s}}}{\Omega_{\mathrm{mb}}} T_{\mathrm{s}} = \Phi_{\mathrm{ff}} T_{\mathrm{s}} \tag{4.12}$$

with the beam filling factor $\Phi_{\mathrm{ff}} = \Omega_{\mathrm{s}}/\Omega_{\mathrm{mb}}$.

The radiative transfer equation (Eq. 2.26 from Chapter 2) can be combined with the beam filling factor defined above and the main beam temperature corrected after the subtraction of the background temperature. Hence, the radiative transfer equation results in:

$$T_{\mathrm{mb}} = \Phi_{\mathrm{ff}} \left[J_\nu(T_{\mathrm{ex}}) - J_\nu(T_{\mathrm{bg}}) \right] \left(1 - e^{-\tau_\nu} \right) \tag{4.13}$$

4.2 [CII] Observational History

The observation of far infrared spectral emission coming from outside the Earth presents inherent challenges to its realization that need to be addressed. First, the atmosphere of the Earth in this regime is largely opaque, hence the requirement of observations at stratospheric altitudes through airborne observatories, or space satellites. Second, in order to simply detect photons in this regime, instrumentation and detector technology have needed substantial advance through the decades. Therefore, the first astronomical detection had to wait until 1980, when Russell et al. (1980) (Fig. 4.2) observed the [CII] line towards the Orion Nebula M42 and NGC 2024 with the Lear-Jet observatory, soon followed by a strip-map of the M17 SW PDR interface (Russell et al. 1981), showing a surprisingly large spatial extent of the [CII] emission. The observations were done with the 30 cm Lear Jet telescope and the f/6.5 liquid-helium cooled grating spectrometer (Houck & Ward 1979). The spectral resolution was ~ 0.3 μm or 1E12 KHz (modern instruments such as up-GREAT/SOFIA have a resolution of ~ 150 KHz.)

The Lear-Jet observatory was soon replaced by the improved capabilities and instrumentation of the Kuiper Airborne Observatory (KAO, Gillespie 1981). The observatory studied a larger sample composed by Milky Way sources and nearby galaxies in [CII] and the other relevant FIR-fine structure lines (e.g. Genzel et al. 1984, 1985; Crawford et al. 1985, 1986; Stacey et al. 1987; Stutzki et al. 1988). KAO went from single pixel heterodyne receivers (Betz & Zmuidzinas 1984; Roeser et al. 1987) to a 5x5 low resolution Fabry-Perot spectrometer called FIFI (Poglitsch et al. 1990). Subsequent early balloon observations (BICE, Nakagawa et al. 1998) demon-
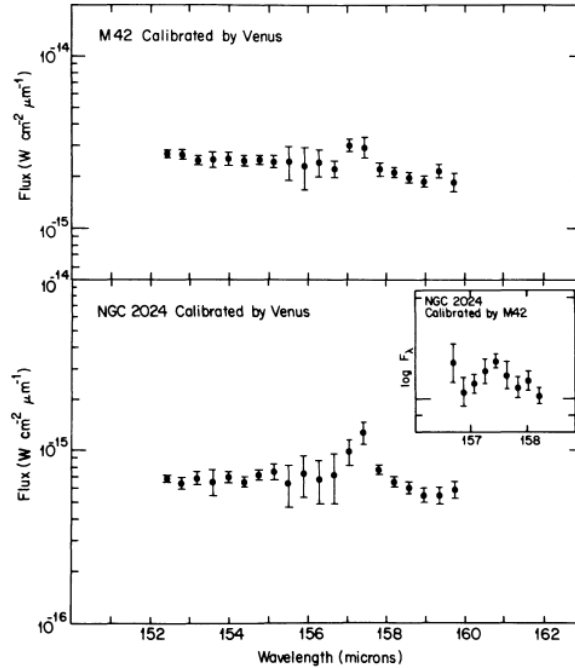
Figure 4.2: First [CII] spectra by Russell et al. (1980). Spectra of NGC 2024 and M42, from 152 to 160 μm.

strated that the [CII] emission is prominently extended across the Milky Way. The ISO satellite extended the [CII] observations to a large sample of galactic and extragalactic sources and started to exploit the possibility of using the [CII] 158 μm line to study the star forming history of galaxies (e.g. Malhotra et al. 1997; Luhman et al. 1998; Colbert et al. 1999).

The Herschel Space Observatory (Pilbratt et al. 2010) expanded the observations of far-infrared and submillimeter wavelengths for galactic and extragalactic sources. The PACS (Poglitsch et al. 2010) far-infrared photometer and medium resolution spectrometer gave access to images in two simultaneous bands of galactic and extragalactic sources (e.g. Davies et al. 2010; Smith et al. 2012; Contursi et al. 2013; Elia et al. 2014; Cormier et al. 2015; Schneider et al. 2016a). Many of these observations were integrated line intensities of FIR fine structure lines, due to technological reasons. The most common technology available was the one for building reliable low resolution spectrometers with high observing speed. The integrated line intensity observations were interpreted thanks to the new tools provided by the PDR numeric models. But, these observations were limited by its spectral resolution, being insufficient for resolving the intrinsic, thermal and turbulent line width of the [CII] emission.

To spectrally resolve the [CII] line, it was necessary to wait for heterodyne detec-

tion technology with high spectral resolution. Pioneering observations were done on KAO towards M42 region in Orion (see Fig. 4.3 below in the next section). The HIFI instrument on Herschel (de Graauw et al. 2010) was the first instrument able to routinely obtain velocity resolved spectra of [CII] 158 μm and other tracers ([NII] 205 μm or [OI] 145 μm) (e.g. Ossenkopf et al. 2013; Velusamy & Langer 2014; Ibar et al. 2015; Mookerjea et al. 2016; García et al. 2016; Lebouteiller et al. 2017). HIFI also allowed a blind [CII] survey to a sample of pointed observations (GOTC+ project, Pineda et al. 2013; Langer et al. 2014; Pineda et al. 2014). The survey traced a large amount of hydrogen not detected by molecular tracers such as CO, the so-called CO-dark H_2, and most of the emission came from dense PDRs.

These observations were still limited in bandwith and spectral baseline stability, but the rapid technological progress in the field, resulted in the state-of-the-art upGREAT heterodyne array instrument (Risacher et al. 2016) on board the Stratospheric Observatory for Infrared Astronomy (SOFIA, Young et al. 2012). upGREAT now allows routinely high sensitivity, high spectral resolution observations of [CII] and other FIR fine structure lines.

4.3 [^{13}CII] First Observations

The detection of the [^{13}CII] lines, apart from the challenges associated to the [^{12}CII] detection described above, has its own intrinsic difficulties: on the one hand, it needs high spectral resolution, for the outer satellite lines which are in addition very weak, still require a spectral resolution higher or at least half of their velocity separation, around 30 km/s. In the case of intrinsically very narrow lines, one can use the much brighter F=2$\rightarrow$1 satellite, requiring a spectral resolution below 5 km/s.

On the other hand, an elemental abundance ratio in the range of 30 to 70 implies that the lines are very weak, thus requiring long integration times even with modern, sensitive detectors. Hence observation of [^{13}CII] hyper-fine structure line satellites have presented an observational challenge and it has been observed and published to date only in four cases: A marginal detection of [^{13}CII] F=2$\rightarrow$1 was reported by Boreiko et al. (1988) in M42 Orion with the KAO using their pioneering FIR heterodyne receiver (Fig. 4.3). They partially detected the strongest [^{13}CII] F=2-1 satellite, but the high signal to noise (S/N) did not allow for a certain confirmation. Stacey et al. (1991) independently reported the detection of [^{13}CII] F=2$\rightarrow$1 in M42 with the ultra-high resolution central pixel of the Fabry-Perot spectrometer instrument FIFI on board the KAO (Fig. 4.4).
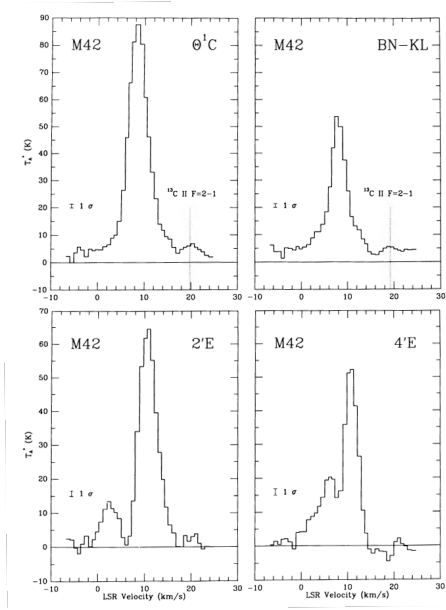
Figure 4.3: [^{12}CII] spectra towards 4 position in M42 with a marginal detection of the [^{13}CII] F = 2-1 satellite line by Boreiko et al. (1988).
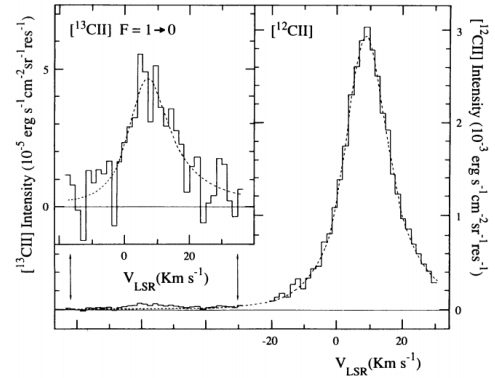
Figure 4.4: [^{12}CII] and [^{13}CII] spectra toward the Orion interface. From Stacey et al. (1991).

Graf et al. (2012), with the improved sensitivity and larger bandwidth of the GREAT receiver (Heyminck et al. 2012) on board SOFIA detected for the first time all three [^{13}CII] satellites, as well as deep self-absorption by cold foreground gas in [^{12}CII] as clear indication of high optical depth in NGC 2024. They were even able to map the extended [^{13}CII] emission (Fig. 4.5). Finally, Ossenkopf et al. (2013) reported the detection of the [^{13}CII] emission in the Orion bar with Herschel/HIFI, during the analysis of four PDRs, followed by an extended analysis by Goicoechea et al. (2015) (Fig. 4.6).

4.4   SOFIA Telescope

The Stratospheric Observatory For Infrared Astronomy (SOFIA, Becklin & Gehrz 2009; Young et al. 2012) is a joint project between NASA and the German Space Agency (DLR). The observatory is an extensively modified Boeing 747SP aircraft carrying a reflective telescope (Fig. 4.7). The SOFIA telescope is composed of a 2.7 m primary mirror with 2.5 m of effective diameter, a hyperbolic secondary mirror in a Cassegrain configuration and a flat tertiary mirror.

The main objective of the observatory is to perform Infrared (IR) observations at high altitudes to a wide range of astronomical sources such as star forming regions,
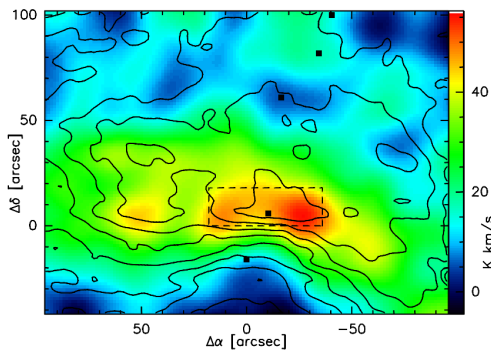
Figure 4.5: [^{13}CII] integrated intensity line map in colors and [^{12}CII] integrated intensity line contours toward NGC 2024. From Graf et al. (2012).
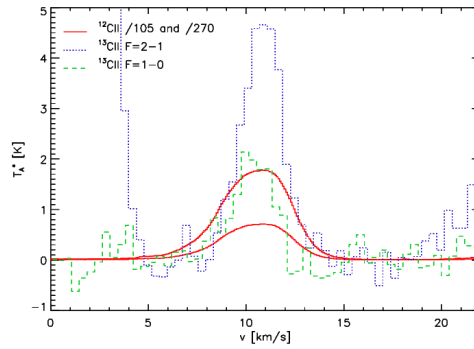
Figure 4.6: Line profile of the two strongest [^{13}CII] satellites in the Orion bar compared to [^{12}CII] profile scaled down by the elemental ratio α of 67 and the relative intensity of the satellites Ossenkopf et al. (2013).

Figure 4.7: SOFIA airborne observatory. Credit: NASA/Jim Ross

PDRs, planets, comets and asteroids in the solar system, nearby galaxies and planetary nebulae. SOFIA is also a pioneer in the study of atomic and molecular line emission and in the identification of complex molecules in the ISM such as Ortho-D_2H^+ (Harju et al. 2017) or HeH^+ (Güsten et al. 2019). The high altitudes (13.7 Km) allow to avoid more than 98% of the atmospheric water vapor. The Earth atmosphere is largely opaque at ground level in the IR regime. The typical precipitable water vapor at these altitudes is 10 μm.

The wide range of instruments on board SOFIA cover a wavelength range from 0.3 to 609 μm. Main instruments are upGREAT, FIFI-LS, HAWC+, FORCAST and EXES. upGREAT is a a Terahertz 7x2 pixels array heterodyne receiver that provides high resolution spectra of fine and hyper-fine structure atomic lines as well as ro-vibrational molecular transitions for a frequency window in the 0.490-4.747 THz range. FIFI-LS is an integral field, far-infrared spectrometer conformed by a 5x5 pixel array in the wavelength range of 51-200 μm. It provides large field of view images of fine structure atomic lines and continuum. HAWC+ is a FIR camera and imaging polarimeter that operates in the wavelength range of 50 to 240 μm. It uses two 64*40 pixel arrays of bolometers. It allows the study of polarization and the structure of magnetic fields. FORCAST is a dual-channel id-infrared camera and spectrograph that operates between 5 and 40 μm. Each channel has a 256x256 pixel array and it allows the study of the continuum and line emission in the mid-IR range. Finally, EXES is a Spectrograph that operates in the 4.5-28.3 μm wavelength range and is formed by a 1024x1024 detectors array. It allows the observation of low resolution spectra for lines such as the H_2O absorption lines.

4.4.1 GREAT Receiver

The **G**erman **RE**ceiver for **A**stronomy at **T**erahertz Frequencies (GREAT) (Young et al. 2012) was a DSB single pixel heterodyne receiver on board SOFIA. It had a modular design with four detectors available to install. The two low frequency detectors were able to run in parallel. The first low frequency detector was the L1 channel. It operated in the range between 1.27 to 1.39 THz and 1.43 to 1.52 THz, with a gap in between due to a frequency block of the atmosphere. Lines such as high-J CO rotational lines and the [NII] 205 μm fine structure line were possible to observe. The second low frequency detector was the L2 channel. It operated between 1.82 to 1.92 THz and allowed to observe high-J CO lines and [CII] 158 μmfine structure line.

The mid-frequency detector was the M channel. It operated between 2.4 and 2.7 THz. It allowed to observe HD 1-0 at 2.6 THz and OH. Finally, the high frequency detector was the H channel. It operated at 4.7 THz and allowed to observe the [OI]

63 μm fine structure line. The backends were AFTT with 1.5 GHz of bandwidth and a resolution of 212 kHz. Later, they were updated to XFFTS with 2.5 GHz of bandwith. GREAT was slowly replaced in a step by step process by two instruments. One of them is the 2x7 upGREAT array that operates two detectors in parallel in the same bands as the old L2 and H channels. The other instrument is the four-color single-pixel detector 4GREAT. It operates in four frequency bands simultaneously. The bands are between 492 and 635 GHz, 892 and 1100 GHz, the old L1 and M channels. GREAT was fully replaced in 2018 with the introduction of the last 4GREAT detector.

4.4.2   upGREAT Receiver

The upGREAT receiver (Risacher et al. 2016) is a DSB array 7x2 pixel heterodyne receiver that operates in the airborne telescope SOFIA. The receiver, with its modular design, allows up to two channels with different frequencies to work in parallel. The receiver is an upgrade of the original GREAT receiver, and it has 2 separated channels. Each of them has a (2x)7 pixel array and they are the low frequency array (LFA) channel, and the high frequency array (HFA) channel. The LFA channel operates in a frequency between 1.9 to 2.5 THz, with an LO composed of photonic mixers that cover the full bandwidth range. The array layout is formed by 2x7 pixels working at both polarizations, H and V, in an hexagonal pattern and a pixel separation in the sky of 34″ for this frequency range. This range allows to observe the [^{12}CII] and [^{13}CII] structure line and the [OI] 145 μm fine structure line.

The second channel is the HFA channel working at a specific frequency of 4.754 THz. The array layout is distributed in a similar way as in the LFA band, but with the pixels working at a single polarization in the hexagonal layout with a pixel separation of 13.8″. This channel allows to observe the [OI] 63 μm fine structure line. The receiver has also a beam rotator that allows to rotate the array configuration for any angle. The mixers for both channels are Hot Electron Bolometer (HEB) mixers (Pütz et al. 2012; Buchel et al. 2015). The backends are MPIfR-built fast Fourier transform (FFT) spectrometers (Klein et al. 2012) with 4 GHz of instantaneous bandwidth with a number of channels of 32 k and a channel spacing of 122 kHz.

4.4.3   SOFIA Observations

The observations carried out for this thesis were done with the SOFIA airborne observatory using either the single pixel GREAT receiver (Heyminck et al. 2012) or the upGREAT array receiver. As the observations were performed over several observing campaigns, during which the receiver evolved and its configuration changed,

some of the [CII] observations were done with the GREAT L2 single pixel channel and some with the upGREAT 7 pixel/2 polarization configuration (LFAH, LFAV). The [CII] channel was combined with different receivers in the other GREAT frequency channel: for M43, the Horsehead PDR and M17, the L1 single pixel channel tuned to [NII] 205 μm was used in parallel. And for Mon R2, the available upGREAT 7 pixel HFA was used in parallel, tuned to [OI] 63 μm. As spectrometers, the FFTS backends were used with an intrinsic velocity resolution of 38 m/s. All the observations were done in total power mode.

The calibration of the data to a main beam brightness temperature intensity scale, T_{mb}, was done with the *kalibrate* task (Guan et al. 2012), including bandpass gain calibration from counts into intensities, fitting an atmospheric model to the observed sky-hot scans in order to correct for the frequency dependent atmospheric transmission from the signal and image sideband. The main beam efficiencies of the individual pixels was derived through the observation of planets such as Jupiter and Saturn and for each observing epoch.

On average, the main beam efficiencies were ~0.65, consistent with the optical layout of the receiver and telescope. The main beam temperature scale is used because SOFIA's main beam pattern is clean, with low side lobes. Then, the data was further processed with the CLASS 90 package, part of the GILDAS [1] software. The long integration time in addition to the improved sensitivity of the new upGREAT/SOFIA allowed to resample the spectra to a velocity resolution of 0.3 km/s in order to obtain an rms of typically 0.2 K.

4.4.3.1 M43 Observation Strategy

The central coordinates used for these observations are 05 h 35 m 31.36 s and -05° 16′ 02.6″. During the observations, a map of 600″× 140″extent was observed, shown in Fig. 4.8, in total power on-the-fly (OTF, Mangum et al. 2007) mode for identifying the [CII] peak. A off-source reference position was used with an offset relative to the center of the map of (603″,76″). This off position was selected from CO J=2-1 observations without emission, and with a far distance from the central emission. For the deep integration to detect the [^{13}CII] line, the position of the peak emission was selected at offsets relative to the center the map of (-107.6″,28.5″). The pointing of the array was done with an orientation angle of 0° in total power mode. Weak contamination was found in the off position for [CII] with an intensity of about 2 K. The contamination was corrected through a Gaussian profile fit to the OFF emission extracted from the sky-hot spectra, which was then applied as a cor-

---

[1] https://www.iram.fr/IRAMFR/GILDAS/
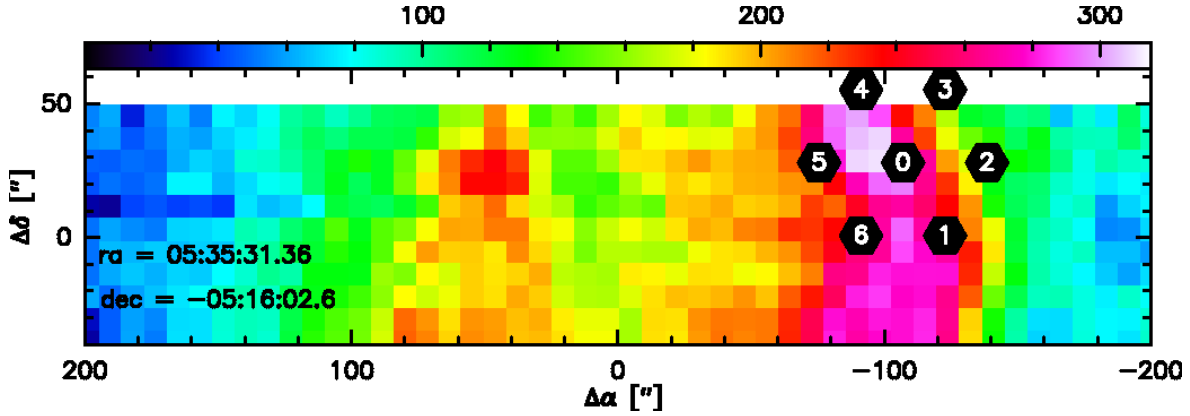
Figure 4.8: M43 [CII] integrated intensity map between 05 to 15 km/s with the position of the upGREAT array at 0°.

Table 4.1: M43 positions

	RA (J2000) (h:m:s)	DEC (J2000) (°:′:″)	Rel. Offset l (″)	Rel. Offset b (″)	rms (K)
Pos.0	5:35:24.16	−5:15:34.14	−107.6	28.5	0.18
Pos.1	5:35:23.18	−5:15:59.82	−122.3	2.8	0.20
Pos.2	5:35:22.19	−5:15:36.07	−137.1	26.5	0.20
Pos.3	5:35:23.35	−5:15:03.49	−119.7	59.1	0.17
Pos.4	5:35:25.39	−5:15:07.15	−89.3	55.5	0.18
Pos.5	5:35:26.42	−5:15:35.11	−73.9	27.5	0.16
Pos.6	5:35:25.23	−5:16:01.35	−91.7	1.3	0.15

rection to the contaminated observations (see Appendix A). The T_{rec} in DSB mode during the observations was 2800 K with a pwv of 12 μm and a total observing time of 60 minutes. The rms noise of the observations was between 0.15 and 0.20 K.

4.4.3.2 The Horsehead PDR Observation Strategy

The Horsehead PDR coordinates used for these observations were 05 h 40 m 54.27 s and -02° 28′ 00.0″. The observations were performed in two separate flight legs. The selection of the positions for the deep [^{12}CII] and [^{13}CII] integrations were made from the previous [CII] Horsehead map observed within the SOFIA Director's Discretionary Time. We pointed the LFA [CII] array to the map coordinate offsets (-5.5″,45.9″) with an array orientation angle of 30° (so that three pixels are aligned N-S) in total power mode, thus covering three positions along the bright [CII] ridge and the other 4 positions of the array being pointed slightly off, but parallel to the main ridge on both sides (see Fig. 4.9). An off-source position at (-733″,-27.5″) was
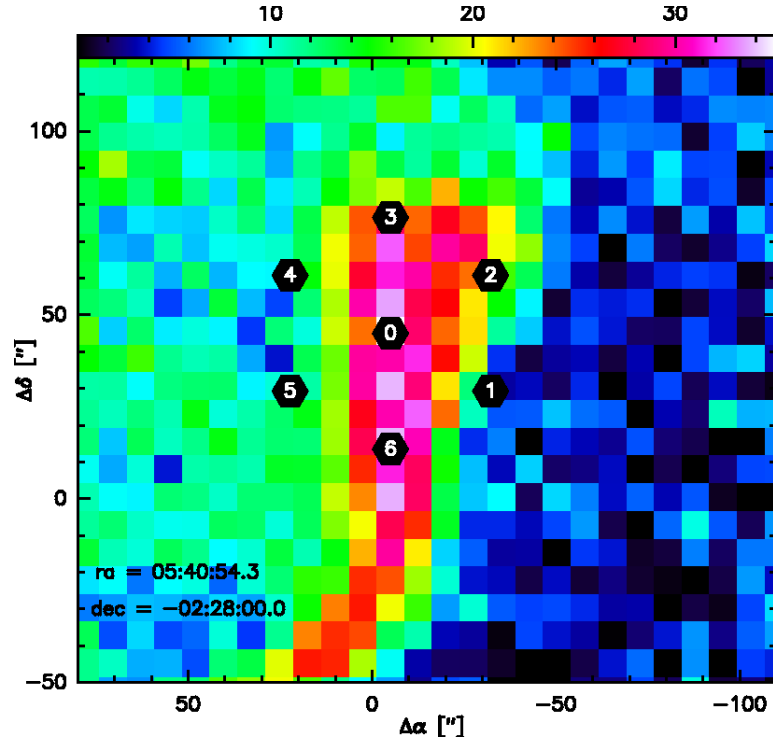
Figure 4.9: The Horsehead PDR [CII] integrated intensity map between 09 and 13 km/s with the position of the upGREAT array at 30°.

used. The T_{rec} in DSB mode was 2200 K and 2100 K for each flight respectively, with a total observing time of 154 minutes and a pwv of 8 μm and 11 μm respectively during the observations. The rms noise of the observations is between 0.08 and 0.10 K.

4.4.3.3 Monoceros R2 Observation Strategy

The Monoceros R2 (MonR2) coordinates used for these observations are 06 h 07 m 46.20 s and -06° 23' 08.0''. For the observations, two positions were observed at map offsets (0'',05'') and (−20'',05'') with the single pixel L2 GREAT channel. The positions were selected for being the two main peaks of [CII] emission (Pilleri et al. 2014), Fig. 4.10. The off-source position was at (−200'',0''). Weak contamination was found for [CII] with an intensity of around 2.5 K. The contamination was corrected following the procedure described in Appendix A against a further out off-source position at (−400'',0''). The observations were performed in total power mode. The T_{rec} in DSB mode during the observations was 1700 K with a pwv of 13 μm and a total observing time of 32 minutes. The rms noise of the observations is between 0.17 and 0.30 K.

Table 4.2: Horsehead PDR

	RA (J2000) (h:m:s)	DEC (J2000) (°:′:″)	Rel. Offset l (″)	Rel. Offset b (″)	rms (K)
Pos.0	5:40:53.91	−2:27:14.09	−5.8	45.9	0.08
Pos.1	5:40:52.11	−2:27:29.27	−32.4	30.7	0.10
Pos.2	5:40:52.14	−2:26:59.76	−32.1	60.2	0.10
Pos.3	5:40:53.98	−2:26:43.54	−4.4	76.5	0.10
Pos.4	5:40:55.80	−2:27:00.60	22.8	59.4	0.09
Pos.5	5:40:55.75	−2:27:32.54	22.1	27.5	0.08
Pos.6	5:40:53.91	−2:27:45.24	−5.6	14.8	0.09
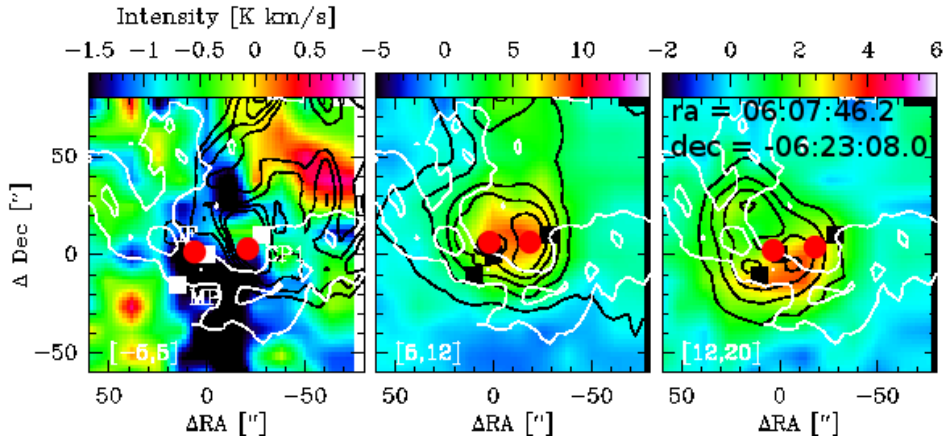
Figure 4.10: Mon R2 [CII] integrated map intensity from Pilleri et al. (2014) in black contours in overlay with other species, the 2 observed positions has been pointed out as red circles for contrast.

Table 4.3: Monoceros R2

	RA (J2000) (h:m:s)	DEC (J2000) (°:′:″)	Rel. Offset l (″)	Rel. Offset b (″)	rms (K)
Pos.1	6:07:46.21	−6:23:03.01	0	5	0.17
Pos.2	6:07:44.87	−6:23:03.01	-20	5	0.3
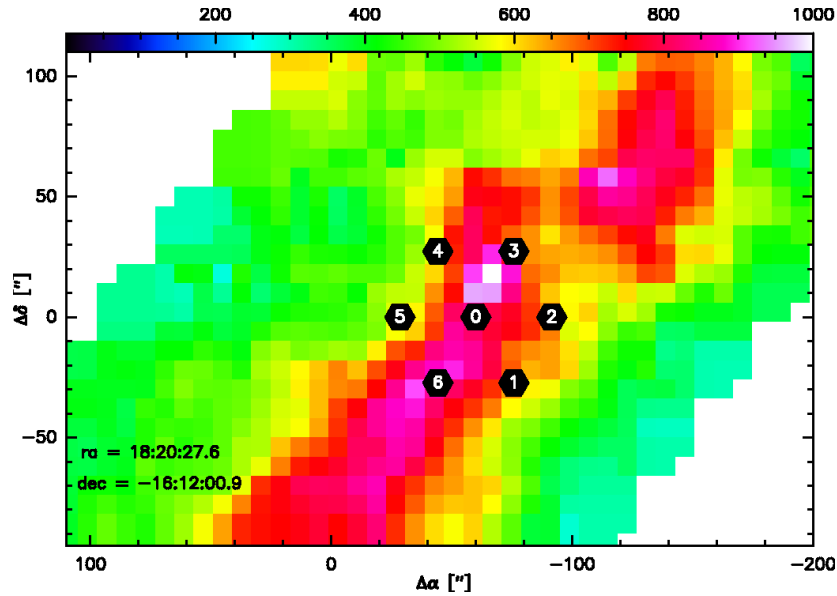
Figure 4.11: M17 SW [CII] integrated intensity map (Pérez-Beaupuits et al. 2012) between 15 to 25 km/s with the position of the upGREAT array at 0°.

4.4.3.4 M17 Observation Strategy

The M17 SW observations used the position of the SAO star 161357 as the map center position (18 h 20 m 27.60 s & -16° 12' 00.9''). Based on previous observations (Pérez-Beaupuits et al. 2012) of M17 SW in [CII] with GREAT, the array was pointed to follow the main emission ridge. The map was centered at the relatives coordinates of $(-60'',0'')$ with an angle of 0°, see Fig. 4.11. A close-by offset position was used at $(537'',-67'')$ selected from a Spitzer 8 μm map of M17 from a region without emission. This off-source position was observed against a second far distant reference position at $(1040'',-535'')$. Indeed, due to the large extent of the [CII] emission around M17 SW, weak contamination for [CII] was found with an intensity of 3.5 K peak brightness temperature at the nearby OFF position, that was corrected according to Appendix A. The T_{rec} in DSB mode was 3200 K, with a total observing time of 84 minutes and a precipitable water vapor (pwv) of 9 μm during the observations. The rms noise of the observations is between 0.18 and 0.33 K.

4.5 NANTEN2 Telescope

The NANTEN2 observatory (Kawamura et al. 2005) is a joint collaboration between the University of Nagoya from Japan, and the Universität zu Köln and the Argelander Institute for Astronomy at the University of Bonn from Germany, with additional collaborators such as the University of New South Wales and the University

Table 4.4: M17 SW

	RA (J2000) (h:m:s)	DEC (J2000) (°:′:″)	Rel. Off. l (″)	Rel. Off. b (″)	rms (K)
Pos.0	18:20:23.46	−16:12:02.01	−60.6	−1.1	0.32
Pos.1	18:20:22.45	−16:12:30.20	−75.1	−29.3	0.33
Pos.2	18:20:21.34	−16:12:05.00	−91.1	−4.1	0.23
Pos.3	18:20:22.32	−16:11:35.89	−76.9	25.0	0.22
Pos.4	18:20:24.61	−16:11:34.82	−44.0	26.1	0.31
Pos.5	18:20:25.70	−16:12:02.77	−28.2	−1.9	0.18
Pos.6	18:20:24.66	−16:12:29.23	−43.3	−28.3	0.31

of Adelaide from Australia and the Universidad de Chile from Chile. The observatory is located in the Atacama Desert of northern Chile at an altitude of 4800 m a.s.l., on Pampa la Bola next to Cerro Chajnantor. The telescope is a 4-m submillimeter telescope.

The main objective of the NANTEN2 observatory is the large scale mapping of southern hemisphere sources in molecular and atomic spectral lines between 110 and 880 GHz. The focus is the study of the distribution, structure, dynamics and chemistry of the ISM in the Galaxy and nearby external galaxies. It has two independent instruments that work separately in turns, depending on the weather conditions. A low frequency heterodyne receiver operated by the University of Nagoya, able to observe low-J CO rotational transitions at 110 and 220 GHz. This receiver operates when the precipitable water vapor is higher than 1 mm. And a mid frequency heterodyne receiver 8 pixel array called SMART operated by the University of Cologne. SMART capabilities are detailed below.

4.5.1 SMART Receiver

The Submillimeter Array Receiver for Two Frequencies (SMART, Graf et al. 2003) is a DSB dual channel 2x8 pixels heterodyne receiver installed in the 4 meter NANTEN2 telescope. It operates simultaneously in two frequencies in the submillimetric regime. The low frequency 460 GHz channel has a frequency range between 435 to 495 GHz, with an IF frequency of 4 GHz. And the high frequency 810 GHZ channel, with a frequency range between 795 and 880 GHz and an IF frequency of 1.5 GHz. The array configuration consists in two rows of four pixels in a rectangular shape with a separation between the pixels of 85″ for the 460 GHz band. A beam rotator allows to rotate the array in any angle possible.

The mixers are SISs mixers with a bandwidth of 4 GHz for both channels. The backends correspond to 16 xFFTS spectrometers with a 2.5 GHz bandwidth and 32768 channels. For the 460 GHz channel, [CI] $^3P_1$-$^3P_0$ atomic line or the CO J=4-3 molecular line can be tuned. For the 810 GHz channel, due to the bandwidth available, the [CI] $^3P_2$-$^3P_1$ atomic line and the CO J=7-6 molecular line can be observed simultaneously.

4.5.2   M17 Observation Strategy

The NANTEN2 observations of M17 SW use the position of the SAO star 161357 as the map center position (18 h 20 m 27.60 s,-16° 12′ 00.9″). For SMART, the basic unit for observing maps in OTF mode is a rectangular footprint of 340″ by 170″ to be observed in horizontal or vertical mode with respect to the orientation of the footprint. From there, the footprint is shifted in a horizontal or vertical direction creating a tile pattern with the footprint as a measuring unit.

Therefore, the 460 GHz receiver was tuned to the [CI] $^3P_1$-$^3P_0$ atomic line (the 810 GHz channel was not available during the observations). The array was rotated 90°and a map of 680 x 1360 arcsec^2 was observed. The map was built by 4x4 footprint tiles with a step size along the OTF line of 8.5″ for a 37.4″ beamsize for a fully sampled map (see Fig. 4.12). An additional footprint was observed to cover the emission in the north-east side of M17. For each footprint, the integration time per position is 3 secs. The map was observed four times, two times in horizontal OTF-mode, and two times in vertical OTF-mode. The OFF position was selected away from the main emission ridge, with relative coordinates of (1000″, 0″) and presented marginal contamination away from the velocity range of the source at 60 km/s.

The calibration of the data was done with the *kalibrate* task to scale the data to a main brightness temperature intensity scale. The main beam efficiency was 0.5, and the forward efficiency was 0.86. Then, the data was reduced with the CLASS 90 package, part of the GILDAS software. Due to the experimental state of the receiver, 50% of the data was discarded after quality checks. Finally, the data was resampled to a velocity resolution of 0.5 km/s, resulting in a noise rms of 2 K.
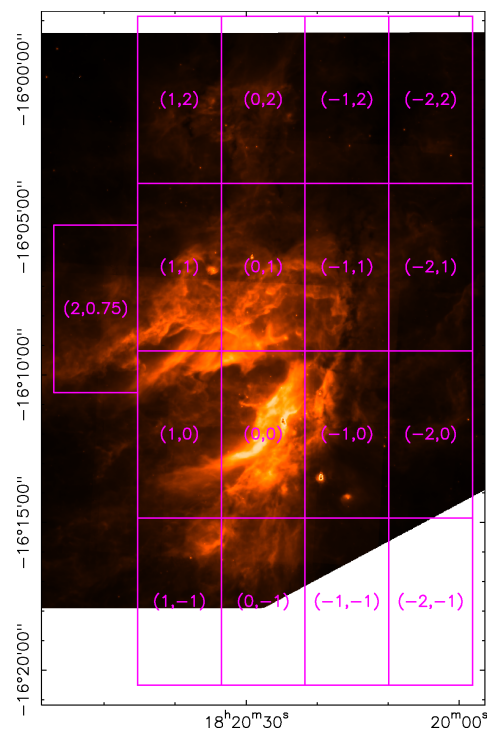
Figure 4.12: M17 [CI] $^3P_1$-$^3P_0$ observing strategy. In colors, 8 μm map from Spitzer. Each rectangle corresponds to a SMART footprint.

5 | [^{12}CII] and [^{13}CII] Optical Depth and Multi-component Dual Layer Model

This chapter shows the results of the [^{12}CII] and [^{13}CII] observations, the derivation of the optical depth of the [^{12}CII] and the development of a multi-component dual layer radiative transfer model to derive the physical properties of the [CII]. It also discusses the implications of the optical depth and self-absorption effects, deals with the possibility of alternative models for the [CII] emission and finally, shows the analysis of complementary data observed along the [CII] observations.

5.1 [^{12}CII] and [^{13}CII] Observations

The observations done toward the four sources, M43, the Horsehead PDR, Monoceros R2 and M17 SW, resulted in high signal-to-noise (S/N) spectra with the [^{12}CII] line and at least one of the [^{13}CII] satellites clearly detected for all the sources. In this section, the line profiles of the four sources and their characteristics are described. In M43, all seven positions observed with the upGREAT-array showed a narrow line profile with the main emission peak located at v_{LSR} ~10 km/s. The four positions with the strongest emission also showed a secondary peak in velocity, located at ~5 km/s, see Fig. 5.1 below. All three [^{13}CII] satellites were well defined and separated from the main [^{12}CII] line emission.

In the Horsehead PDR, the line profile was also narrow, with a single peak at ~10.5 km/s, see Fig. 5.2. In addition, the line profile showed an extended wing toward higher velocities from the [^{12}CII] peak, from 16 to 30 km/s, see Fig. 5.3. Pabst et al. (2017) did not detect this broad wing in their extended analysis of the Horsehead PDR from large scale observations available through the SOFIA Director's Discretionary Time. This feature could only be detected thanks to the long integration time and correspondingly high sensitivity achieved for this [^{13}CII] detection. Only

57
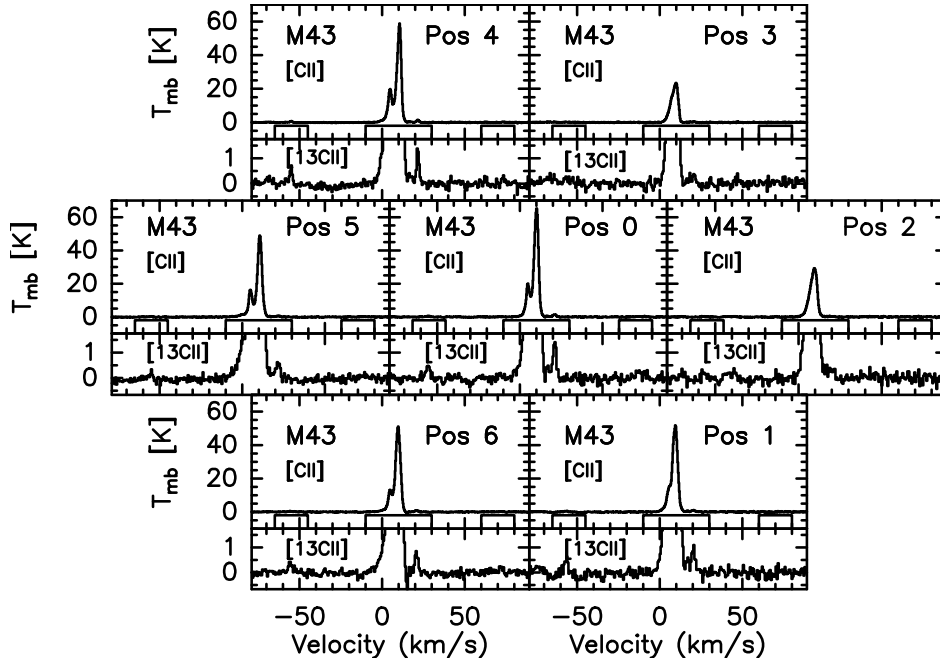
Figure 5.1: Mosaic observed in M43. For each position [^{12}CII] line profile is shown in the top box. Below the spectra, the windows for the base line subtraction is shown (-65,-45) (-10,30) (60,80) km/s. The bottom box shows a zoom to the [^{13}CII] satellites.

the strongest [^{13}CII] satellite ([^{13}CII]$_{F=2-1}$) was well detected in the positions that trace the ridge emission: positions 0, 2, 3 and 6 (Fig. 4.9 from Chapter 4).

For Mon R2, the two positions observed showed a broad emission from 0 to 35 km/s. The [^{12}CII] line profile of each position presented large differences between them, but shared a strong dip at 12 km/s. This situation was already noted by Ossenkopf et al. (2013) from Herschel [CII] observations towards Mon R2. In contrast, [^{13}CII] showed a single peak, at both positions filling the dip visible in the [^{12}CII] emission, see Fig. 5.4. All [^{13}CII] satellites were strong enough to be detected, but [^{13}CII] F = 2 − 1 was blended with the [^{12}CII] line due to the large width of the [^{12}CII] emission line.

For M17 SW, the [^{12}CII] emission was also broad, ranging from 0 to 40 km/s and the line profiles at the seven positions of the upGREAT array pixels showed large differences among each other. The [^{12}CII] profiles showed several narrow peaks and dips between them as discussed by Pérez-Beaupuits et al. (2015b) (see Fig. 5.5). Only the two outer [^{13}CII] satellites could be clearly identified, [^{13}CII]$_{F=1\rightarrow0}$ and [^{13}CII]$_{F=1\rightarrow1}$. [^{13}CII]$_{F=2-1}$ was blended due to the width of the [^{12}CII] emission line.
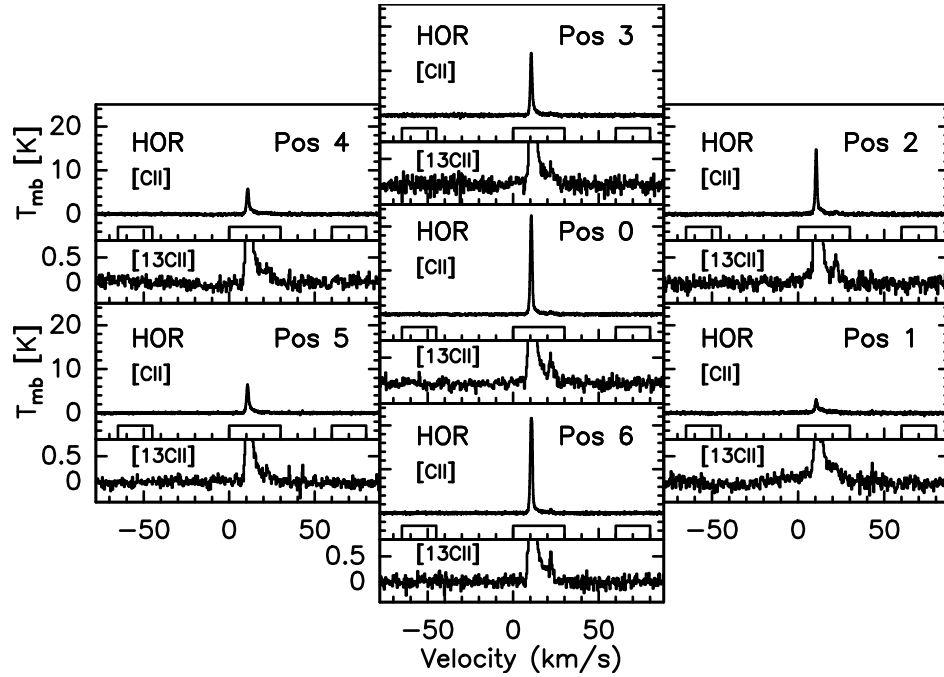
Figure 5.2: Same as Fig. 5.1, but for the Horsehead PDR observations, with the windows for the base line subtraction at (-65,-45) (0,30) (60,80) km/s.
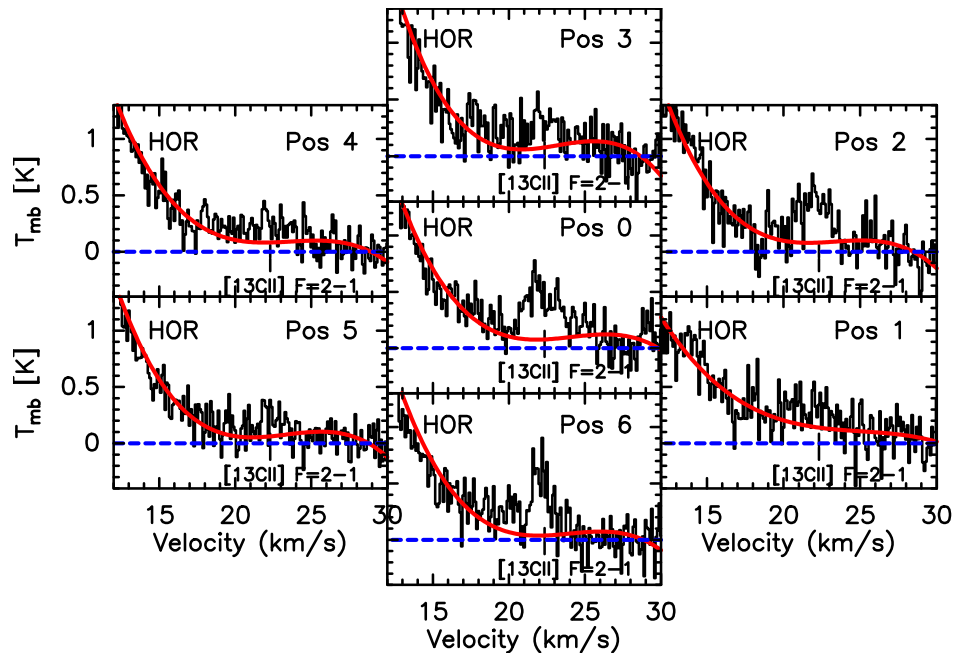
Figure 5.3: The Horsehead PDR [^{13}CII] F=2-1 emission, with the contribution from the [^{12}CII] broad wing extending from 16 to 30 km/s. The line in red represents a baseline of order 3 and the blue dashed line represents the zero intensity level.
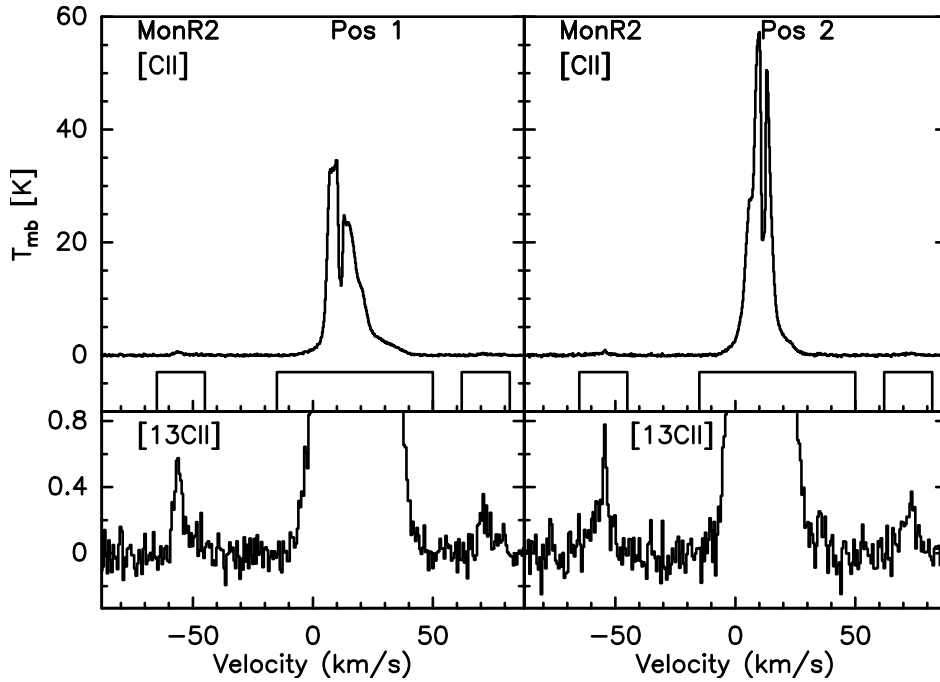
Figure 5.4: Same as Fig. 5.1, but for the Mon R2 observations, with the windows for
the base line subtraction at (-65,-45) (0,30) (60,80) km/s.
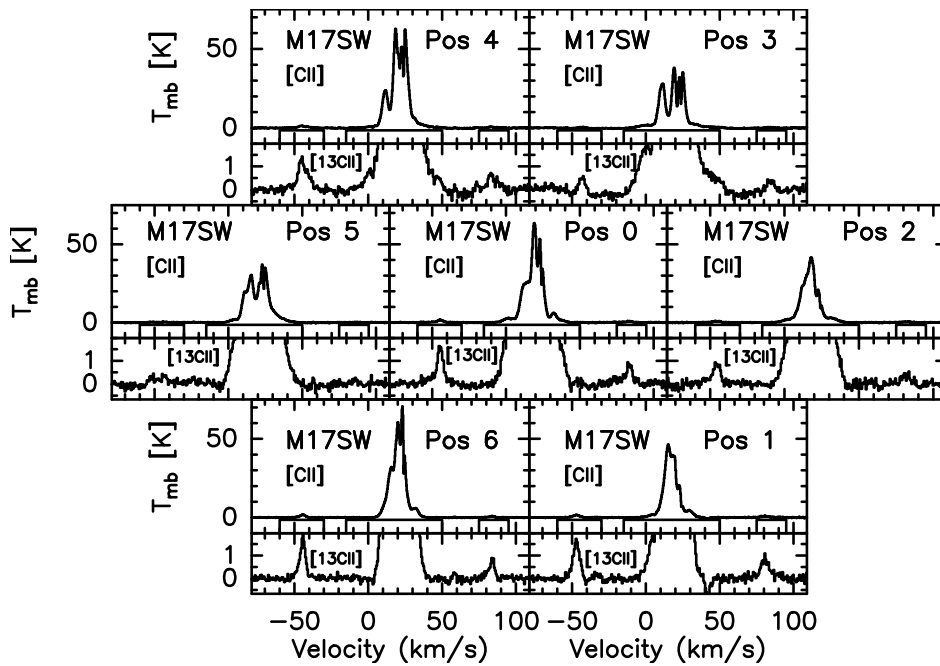
Figure 5.5: Same as Fig. 5.1, but for the M17 SW observations, with the windows for
the base line subtraction at (−60,−30) (−15,50) (75,95) km/s.

5.2 Zeroth Order Analysis: Homogeneous Single Layer

As a first approximation, and without knowing the optical depth or column density of the [^{12}CII], two simplifying assumptions have been made. First, the sources consist of a single, homogeneous layer and second, both isotopes ([^{12}CII] and [^{13}CII]) are in thermodynamic equilibrium and share the same excitation temperature. Due to the split of the [^{13}CII] into three satellites, the noise weighted average was estimated for the available [^{13}CII] hfs satellites using Eq. 2.44 from Chapter 2. For each source, the [^{13}CII] line spectra was scaled up by α^+ and compared to the [^{12}CII] one. These average [^{13}CII] spectra, scaled up by the factor α^+, are plotted as the red histograms in the upper panel of each mosaic from Figures 5.6 to 5.9 below.

For M43 (Fig. 5.6), the [^{13}CII] line profile showed, within its higher noise, a shape consistent with the main isotope line. However, the scaled up intensity was consistently higher than the observed main isotopic line in 4 of the 7 positions. This indicated that the emission is optically thick, as discussed below. The Horsehead PDR required an additional step for performing the profile comparison. In order to separate the [^{13}CII] line profile from the [^{12}CII] broad wing emission described above, the wing emission was fitted with a third order polynomial in the velocity range between 12 and 30 km/s. The fit was subtracted from the observed spectra as is shown in Fig. 5.7. This was necessary in order not to confuse the derivation of the line ratios and the optical depths (see below) with additional emission. Similar to the case of M43, the [^{13}CII] line profile, scaled up by α^+, showed a similar shape to [^{12}CII], within its higher noise, but the intensity was higher than the [^{12}CII] one in positions 0, 2 and 6, indicating an optical depth above 1.

For Mon R2, the scaled up [^{13}CII] line profile had a much higher intensity than the main isotopic line. This suggested that the [^{12}CII] line is clearly optically thick with a significant opacity and the emission dip suggested self-absorption in [^{12}CII], as discussed already by Ossenkopf et al. (2013). Finally, for M17 SW, the [^{13}CII] profile, unlike [^{12}CII], showed a simple, close to Gaussian profile with only one peak at ~ 20 km/s. In a similar way to the other sources, the scaled up [^{13}CII] showed a much higher intensity than the [^{12}CII] one. And similar to Mon R2, the comparison suggested that the M17 SW [^{12}CII] emission is optically thick with emission dips in the [^{12}CII] profile produced by self-absorption.

In summary, the scaled up [^{13}CII] presents a much higher intensity than the [^{12}CII] main isotopic emission in all cases. The match between line profiles is closer in the line wings, but typically the line center emission in [^{13}CII] overshoots the

[^{12}CII] one. This indicated that the implicit assumptions for of low optical depth and a single emission does not apply here.

5.2.1 [^{12}CII]/[^{13}CII] Abundance Ratio and [^{12}CII] Optical Depth

The next step in the zeroth order analysis was the direct estimation of the optical depth, numerically solving Eq. 2.48 from Chapter 2 for $\tau_{12}(v)$ for each velocity bin for all sources. Additionally, the abundance ratio between [^{12}CII] and [^{13}CII] was derived for each velocity bin. The results are plotted below in the lower panel of each mosaic in Figures 5.6 to 5.9. The gray bar histograms give the [^{12}CII]/[^{13}CII] intensity ratio calculated for each velocity bin; the velocity range was restricted to where the [^{13}CII] profiles show an intensity above $1.5\,\sigma$. The derived opacity spectra are shown as blue histograms. The velocity ranges above the [^{13}CII] thresholds for each source are also given.

M43 results are shown in Fig. 5.6. The $1.5\,\sigma$ [^{13}CII] threshold of 0.35 K resulted in a velocity range from 3 km/s to 17 km/s. The [^{12}CII]/[^{13}CII] line ratio ranged typically around 40 in those spectral regimes, where the [^{13}CII] intensity was weak compared to the peak value; closer to the threshold emission level. The deep integrations with upGREAT/SOFIA resulted in high S/N spectra and arose the possibility of measuring directly the [^{12}CII]/[^{13}CII] abundance ratio from these regions of weak [^{13}CII] emission. The opacity derived from the observed [^{12}CII]/[^{13}CII] line ratio showed the presence of optically thick lines along the main emission region for positions 0, 1 and 4, with an optical depth of 2 around the [^{13}CII] peak.

For the Horsehead PDR, the red wing emission visible in the [^{12}CII] was already subtracted. The [^{12}CII] and [^{13}CII] emission profiles were similar and peak at the same LSR-velocity. The velocity range used was 3 km/s to 17 km/s for a [^{13}CII] threshold of 0.22 K (see Fig. 5.7). The [^{13}CII] S/N was not sufficient for a proper estimation of the line ratio outside the line center. The emission was optically thick along the main ridge for positions 0, 3 and 6, with an optical depth of ~ 2. For the outer positions, the low S/N did not allow a good estimate of the optical depth.

For Mon R2, the useful velocity range went from 0 to 25 km/s above a [^{13}CII] threshold of 0.37 K (see Fig. 5.8). The line profiles matched only in the red line wing emission. The [^{12}CII]/[^{13}CII] T$_{\rm mb}$ ratio varied outside the peak, and reached an average values of about 29, lower than the value of $\alpha^+ = 67$ assumed above. The value of the optical depth, derived following the zeroth order analysis, was very high at the line centers of both spectra, reaching up to a value of 7 around the [^{13}CII] peak for both position. The LSR-velocities of the peak emission in [^{13}CII] and [^{12}CII]
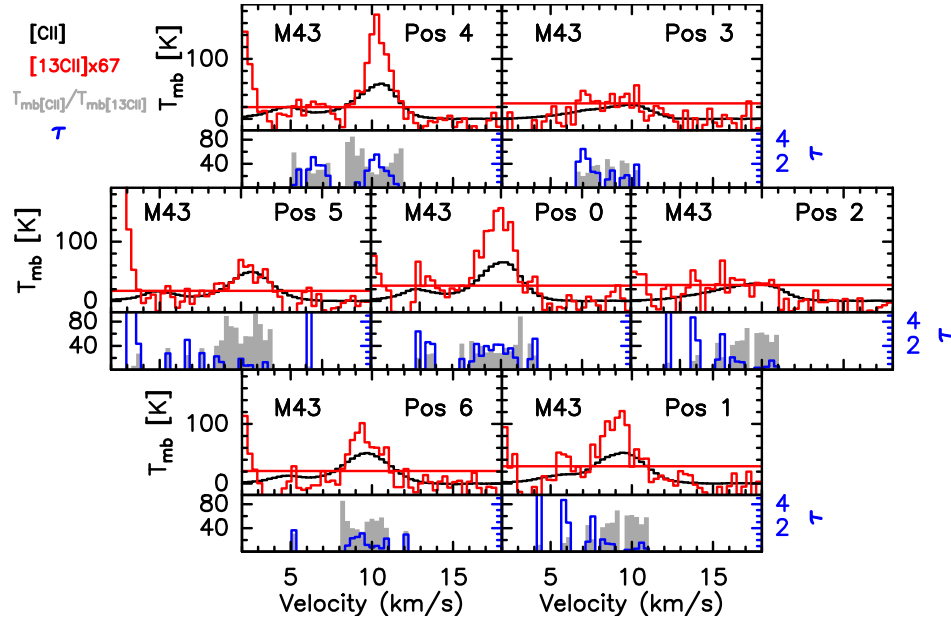
Figure 5.6: M43 mosaic of the seven positions observed by upGREAT. For each position, the top panel shows a comparison between $[^{12}CII]$ (in black) and $[^{13}CII]$ (in red), the latter averaged over the hyperfine satellites and scaled up by α^+. The red line corresponds to 1.5 σ scaled up by α^+. The bottom panel shows the estimation of the optical depth from the zeroth order analysis (blue) and the $[^{12}CII]/[^{13}CII]$ intensity ratio per velocity bin (in gray) for all the observations above 1.5 σ
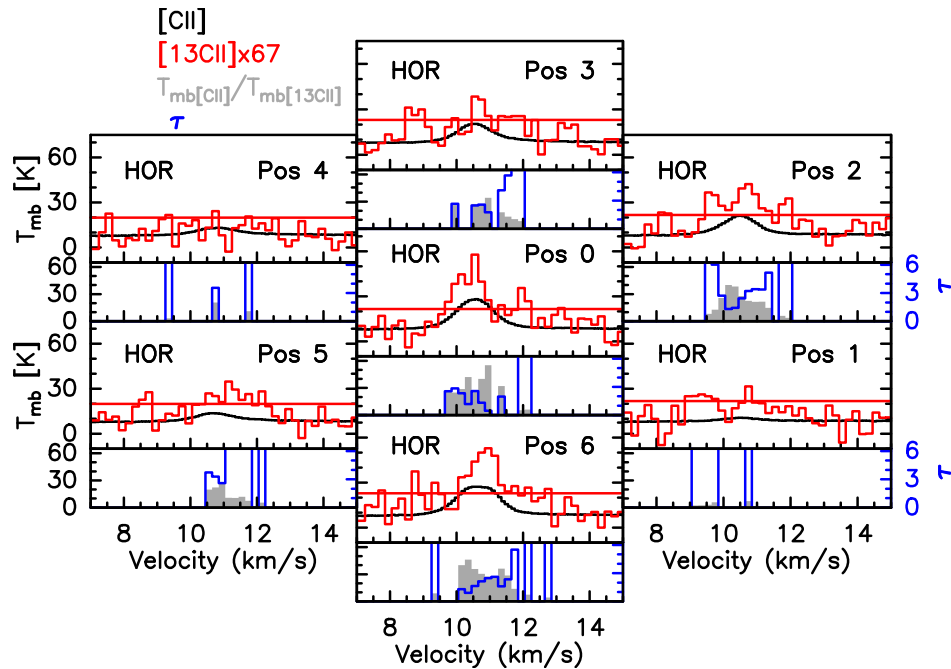
Figure 5.7: Same as Fig. 5.6, but for the Horsehead PDR observations.

63
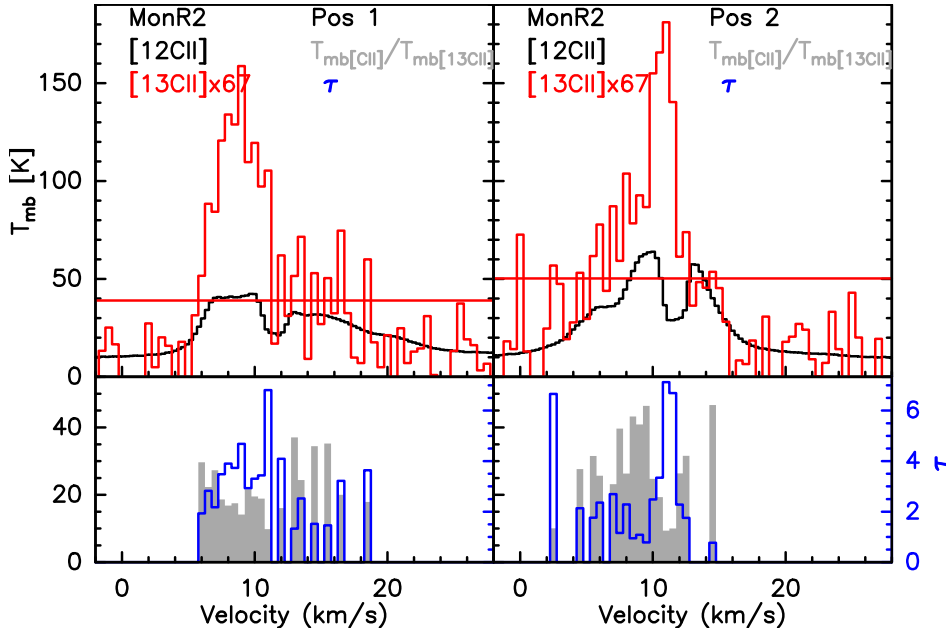
Figure 5.8: Same as Fig. 5.6, but for the 2 positions in Mon R2 observed with GREAT L2.

were slightly shifted with respect to each other. The [^{12}CII] line profile at position 1 was flat topped and both positions showed strong dips in the emission profile. This indicated that the assumption of the zeroth order analysis, namely that of a single component, homogeneous source, is insufficient for explaining the complex line profile of Mon R2.

The situation was similar for M17 SW. For the seven positions observed, the [^{13}CII] spectra, scaled up with the assumed abundance ratio, overshot the [^{12}CII] spectra in the line centers and matched in the line wings. In addition, the [^{12}CII] spectra showed several emission peaks and/or absorption dips, whereas the [^{13}CII] spectra exhibited smooth line profiles. The available velocity range went from 12 km/s to 28 km/s with a [^{13}CII] threshold of 1 K, t (see Fig. 5.9). The [^{12}CII]/[^{13}CII] T_{mb} ratio along the line wings tended to be between 15 and 30 presenting large variations in the values, but in average well below 40 (the value for α^+ assumed above). Correspondingly, the optical depth was still well above unity, even in the wings. In resume, the [^{12}CII] emission was optically thick in the line centers in all positions, with an optical depth between 4 and 7, except at position 5. This position was located outside the main ridge of emission, with an optical depth closer to unity.

For all four sources, the zeroth order analysis showed that the [^{12}CII] emission is optically thick, in particular for Mon R2 and M17 SW. For both of these sources, the [^{12}CII] spectra are partially flat-topped with line profiles showing a complex ve-
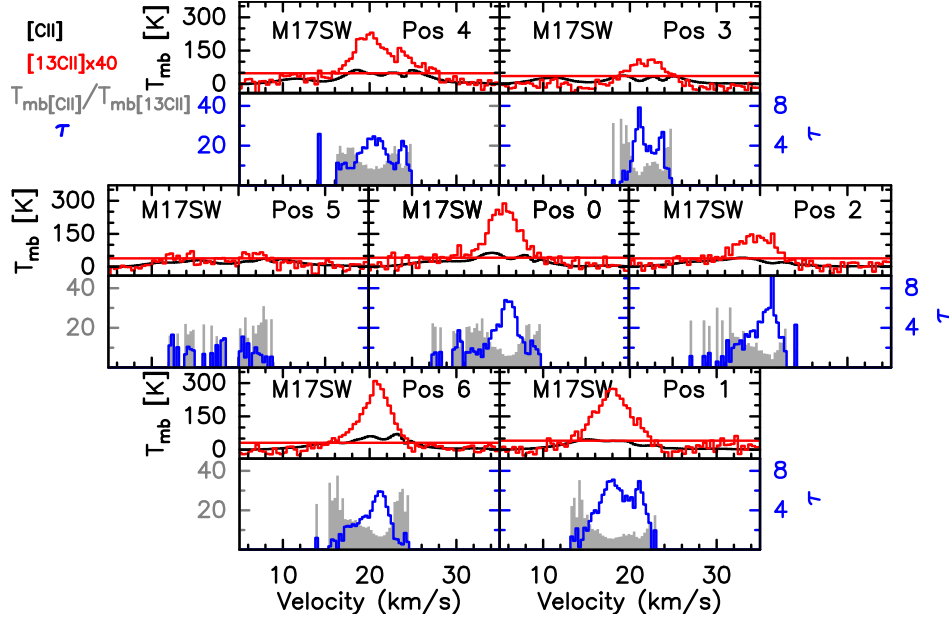
Figure 5.9: Same as Fig. 5.6, but for the M17 SW observations.

locity structure with several emission components and/or absorption dips, clearly indicating that the simplified assumptions of the zeroth order analysis are not met and no further conclusions can be derived. A more sophisticated, multi-component analysis (see Sect. 5.3) had to be used to analyze the complex line profiles.

5.2.2 [^{13}CII] Column Density

The [^{13}CII] minimum column density (N_{min}([^{13}CII])) was estimated from the integrated intensity of [^{13}CII] using 2.55 from Chapter 2 for each position and source. The values are listed below in Table 5.1. From this values, the [^{12}CII] minimum column densities were estimated by scaling the N([^{13}CII]) values with α^+. Additionally, the minimum N([^{12}CII]) was derived directly from the [^{12}CII] integrated intensity assuming optically thin emission (although as it was discussed above, the emission is optically thick), after the subtraction of the [^{13}CII] F=2→1 emission using the [^{13}CII] F=1→0 satellite as a model. Also, the ratio between the N_{min}([^{12}CII]) derived from the scaled-up [^{13}CII] and the N_{min}([^{12}CII]) derived from the assumption of optically thin [^{12}CII] emission was estimated for comparison. This was done to demonstrate how the derived [^{12}CII] column density underestimates the total value by taking into account the optical depth and the self-absorption effects described above. In the following, the derived [^{12}CII] column densities was always converted to an equivalent visual extinction, where the standard value of 1.2×10^{-4} was used for the relative abundance of hydrogen to ionized carbon (Wakelam & Herbst 2008). Also, it was used the canonical conversion factor between hydro-

gen column density and visual extinction of $1.87 \times 10^{21}\,\mathrm{cm}^{-2}/A_V$ (Reina & Tarenghi 1973; Bohlin et al. 1978; Diplas & Savage 1994; Predehl & Schmitt 1995), hence $A_V = N([^{12}CII]) * 0.83 * 10^4/1.87 \times 10^{21}\,\mathrm{cm}^{-2}$. Note that these equivalent extinctions were a lower limit as they assumed that all carbon is the form of C^+.

Table 5.1 shows high column densities and equivalent visual extinctions for the four sources, especially for Mon R2 and M17 SW. Using the [^{13}CII] intensities, the global equivalent A_V peak was 36 magnitudes for one of the position. Also, the minimum column density and the equivalent visual extinction estimated directly for the assumed optically thin [^{12}CII] emission showed much lower values, with a ratio as high as four between the two column densities.

The equivalent visual extinctions derived from [^{13}CII] were in the range of 1 to a few magnitudes for the Horsehead PDR, and reached up to about 7 magnitudes for M43. Note that the Horsehead PDR optical depths estimated above in Section 5.2.1 were similar to the ones derived for M43, whereas the [^{13}CII] column density was lower: the optical depth is given by the column density per velocity element, and hence the smaller line width of the Horsehead PDR compensated for the lower column density. Thus, the derived [^{12}CII] equivalent extinctions and the ratio between both isotopes showed that the scaled-up [^{13}CII] equivalent extinctions were similar or higher than the ones from the assumed optically thin [^{12}CII], specially in the Horsehead PDR. For M43, the ratios around unity likely resulted from a combination of optically thin emission in the outer positions, low sensitivity in the [^{13}CII] wings plus the additional [^{12}CII] emission not traced by [^{13}CII]. For the Horsehead PDR, with its similar optical depth, the higher ratios resulted from the higher noise that tends to increase the estimation of the [^{13}CII] integrated intensity. For Mon R2 and M17 SW, the column densities derived from [^{13}CII] corresponded to an equivalent A_V of 20 and up to 36 mag.

It is important to emphasize that the unexpectedly high [CII] column densities derived here do not change due to the wrong assumption of a single homogeneous layer and the self-absorption effects produced by the high optical depth. In fact, the column densities derived here are the minimum possible, because the column densities were derived in the high excitation temperature limit.

Table 5.1: [^{13}CII] integrated intensity and minimum column density, [^{12}CII] minimum column density scaled up using α and equivalent extinction. [^{12}CII] integrated intensity, minimum column density assuming optically thin emission and equivalent visual extinction. For the derivation of the values, more digits than the one presented here have been used.

Positions	[^{13}CII]				Optically thin [^{12}CII]			Ratio
	[^{13}CII] Int. Intensity (K km/s)	$N_{\min}$([^{13}CII]) (cm^{-2})	$N_{\min}$([CII])[a] [^{13}CII] (cm^{-2})	$A_{v,\min}$[b] [^{13}CII] (mag.)	[^{12}CII] Int. Intensity (K km/s)	$N_{\min}$([CII])[c] [^{12}CII] (cm^{-2})	$A_{v,\min}$[d] [^{12}CII] (mag.)	$\dfrac{A_{v,\min}([^{13}CII])^{b}}{A_{v,\min}([^{12}CII])^{d}}$
M43 0	5.5	2.5E16	1.7E18	7.4	283.1	1.3E18	5.6	1.3
M43 1	4.3	1.9E16	1.3E18	5.7	249.2	1.1E18	4.9	1.2
M43 2	2.6	1.2E16	7.7E17	3.4	172.2	7.7E17	3.4	1.0
M43 3	2.6	1.1E16	7.6E17	3.4	134.0	6.0E17	2.6	1.3
M43 4	5.5	2.5E16	1.7E18	7.4	270.1	1.2E18	5.3	1.4
M43 5	3.7	1.6E16	1.1E18	4.9	227.4	1.0E18	4.5	1.1
M43 6	4.1	1.8E16	1.2E18	5.4	237.9	1.1E18	4.7	1.1
HOR 0	1.2	5.3E15	3.6E17	1.6	39.6	1.8E17	0.8	2.0
HOR 1	0.7	3.1E15	2.1E17	0.9	11.2	5.0E16	0.2	4.2
HOR 2	1.4	6.1E15	4.1E17	1.8	26.6	1.2E17	0.5	3.4
HOR 3	1.0	4.7E15	3.1E17	1.4	25.7	1.1E17	0.5	2.7
HOR 4	0.3	1.2E15	8.4E17	0.4	14.8	6.6E16	0.3	1.3
HOR 5	0.9	3.9E15	2.6E17	1.2	14.7	6.5E16	0.3	4.0
HOR 6	1.6	7.0E15	4.7E17	2.1	41.5	1.9E17	0.8	2.5
MonR2 1	12.2	5.5E16	3.7E18	16.3	410.8	1.8E18	8.1	2.0
MonR2 2	11.4	5.1E16	3.4E18	15.2	477.0	2.1E18	9.5	1.6
M17SW 0	41.6	1.9E17	7.4E18	33.0	657.2	2.9E18	13.1	2.5
M17SW 1	39.1	1.7E17	7.0E18	31.1	460.1	2.1E18	9.1	3.4
M17SW 2	26.9	1.2E17	4.8E18	21.3	458.1	2.0E18	9.1	2.3
M17SW 3	16.5	7.4E16	2.9E18	13.1	489.9	2.2E18	9.7	1.3
M17SW 4	45.1	2.0E17	8.1E18	35.9	722.7	3.2E18	14.4	2.5
M17SW 5	14.1	6.3E16	2.5E18	11.2	521.7	2.3E18	10.4	1.1
M17SW 6	34.3	1.5E17	6.1E18	27.3	617.7	2.8E18	12.3	2.2

[a] [^{12}CII] column density derived from the scaled-up [^{13}CII] column density.

[b] [^{12}CII] equivalent visual extinction derived from the scaled-up [^{13}CII] column density.

[c] [^{12}CII] column density derived directly from the [^{12}CII] integrated intensity assuming optically thin regime.

[d] [^{12}CII] equivalent visual extinction derived directly from the [^{12}CII] integrated intensity assuming optically thin regime.

5.3 Multi-component Analysis: Multi-component Dual Layer Model

From the discussion in the previous section, the four sources had high column density and optically thick emission and, for Mon R2 and M17 SW, additional absorption features. Therefore, it is clear that the simple approximation of a single layer was not adequate. For this reason, an approach similar to the one by Graf et al. (2012) was followed to derive the physical properties of the [CII] emission. The objective was to explain the [^{12}CII] and [^{13}CII] main beam temperature line profiles by a composition of multiple Gaussian source components through a simultaneous least-square fit of both observed profiles. Also, the following assumption was done to explain the discrepancy in the line profiles: the source contained two layers, a background emission layer with a variable number of components adapted to the observed structure of the [^{13}CII] and [^{12}CII] line profile, and, in the case of absorption features in the [^{12}CII] profile, a foreground absorption layer with a different number of Gaussian components.

Additionally, three assumptions were done for the modeling process: The excitation temperature was the same for the [^{12}CII] and all three [^{13}CII] hyperfine structure lines. [^{13}CII] was always optically thin. And, if a [^{12}CII] component did not have a visible [^{13}CII] counterpart above the noise level, the [^{12}CII] component was not affected by self-absorption effects. A superposition of Gaussian line profiles was used for the analysis. Therefore, the line profile $\phi(v)$ from Eq. 2.20 from Chapter 2 was defined for each individual Gaussian source component i, characterized by its LSR-velocity, $v_{\text{LSR},i}$, and full-width-half-maximum line width $\Delta v_{\text{FWHM},i}$ by:

$$\phi_i(v) = \frac{2\sqrt{ln(2)}}{\Delta v_{\text{FWHM},i}\sqrt{\pi}} \exp\left(-\frac{(v - v_{\text{LSR},i})^2 4ln(2)}{(\Delta v_{\text{FWHM},i})^2}\right) \tag{5.1}$$

with the full-width-half-maximum line width $\Delta v_{\text{FWHM},i} = 2\sqrt{ln(2)}\,\Delta v_i/\sqrt{\pi}$, and Δv_i the equivalent width. The combined line profile of each component i for both the [^{12}CII] main line and all three [^{13}CII] hyperfine satellites can be written as:

$$\Phi_i(v) = \phi_i(v) + \sum_{F,F'} \beta_{F\to F'}\phi_i(v - \delta v_{F\to F'}) \tag{5.2}$$

where $\delta v_{\text{F}\to\text{F}'}$ is the [^{13}CII] hyperfine satellite's velocity offset with respect to [^{12}CII] (Table 2.1), and $\beta_{\text{F}\to\text{F}'} = \frac{s_{\text{F}\to\text{F}'}}{\alpha^+}$. For the equation above, the first term corresponds to the line profile of the [^{12}CII] emission and the second one is the com-

bined line profile of the three [^{13}CII] satellites. With these definitions, the optical
depth profile $\tau_i(v)$ can be defined for each individual source component i (using the
optical depth from Eq. 2.51 of Chapter 2) as:

$$\tau_i(v) = \Phi_i(v)\frac{g_{\mathrm{u}}}{g_{\mathrm{l}}}\frac{c^3}{8\pi\nu^3}\,A_{\mathrm{ul}}\,N_{12,i}(CII)\,\frac{\left(1 - e^{-T_0/T_{\mathrm{ex},i}}\right)}{1 + \frac{g_{\mathrm{u}}}{g_{\mathrm{l}}}e^{-T_0/T_{\mathrm{ex},i}}} \tag{5.3}$$

Finally, using Eq. 4.13 from Chapter 4, the observed main beam temperature T_{mb}
can be defined as the combination of the emission from the components i_b of the
background layer and the absorption done by the components i_f of the foreground
layer, plus the emission from the foreground . Hence, $T_{\mathrm{mb}}(v)$ was given by:

$$T_{\mathrm{mb}}(v) = \left[\sum_{i_b}\mathcal{J}_\nu(T_{\mathrm{ex},i_b})\,\left(1 - e^{-\tau_{i_b}(v)}\right)\right]e^{-\sum_{i_f}\tau_{i_f}(v)} +$$
$$\sum_{i_f}\mathcal{J}_\nu(T_{\mathrm{ex},i_f})\,\left(1 - e^{-\tau_{i_f}(v)}\right) \tag{5.4}$$

The multi-component fitting applied Eq. 5.4 in a physically motivated iterative
process. This fitting process is degenerate without any further constraints, as multi-
ple combinations of T_{ex}, $N_{12,i}(CII)$ and $\Delta\mathrm{v}_{\mathrm{LSR}}$ exist for the same optical depth. T_{ex}
and $N_{12,i}(CII)$ are roughly inversely proportional to each other in relation to the
optical depth, as shown in Eq. 5.3. Therefore, T_{ex} was fixed to a reasonable value.

For the background layer, T_{ex} has as a lower limit the Rayleigh-Jeans corrected,
observed T_{mb}, which, to first order, adds $T_0/2 = 45.6\,\mathrm{K}$ to the brightness tempera-
ture. Also, according to PDR models, excitation temperature of 50 K to a few 100 K
maximum are expected. Therefore, the background T_{ex} was fixed to values between
30 and 200 K, depending on the source (see below). This was done for keeping the
background optical depth at reasonable values, closer to unity or a bit higher.

For the foreground layer, T_{ex} must be low to act as an absorption layer without
significant [^{13}CII] emission: an upper boundary is given by the Rayleigh-Jeans cor-
rected brightness temperature in the center of the absorption dips. Lower values
result in lower column densities of the absorbing layer, as less material is needed to
build up sufficient optical depth. Therefore, T_{ex} was fixed for the absorbing layer
with values between 20 K and 40 K. These temperatures were selected because for
lower temperatures, the optical depth is insensitive to changes. Below 20 K, any
change to the excitation temperatures for the same column density affects the opti-
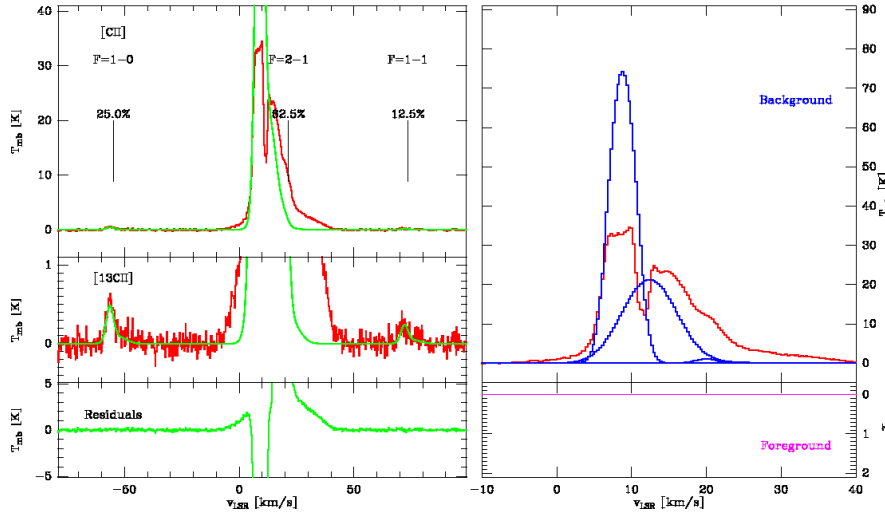
Figure 5.10: Composition of the fitting process. Each plot is built in the same way. *Top Left* - This panel represents the fitted model in green and the observed spectrum in red. *Middle Left* - Zoom of the fitted model and the observed spectrum to better show the [^{13}CII] satellites. *Bottom Left* - Residual between the observed spectrum and the model. *Top Right* - In blue, each emitting component, in cyan the resulting background emitting model from the addition of all the blue components and in red the observed spectrum. *Bottom Right* - Optical depth of each absorbing Gaussian component in pink. First step of the fitting process. Fitting of the [^{13}CII] emission, masking the [^{12}CII] one.

cal depth by less than a 5%. Above 20 K, effects in the optical depth can be seen. Plus, this temperature range fulfills the assumption that the contribution from the foreground layer is insignificant.

In order to illustrate the iterative fitting procedure, position 1 of Monoceros R2 was selected as an example. The procedure is described step by step below:

- Fig. 5.10: The [^{13}CII] emission is fitted as part of the background layer, masking the [^{12}CII] line. The excitation temperature is fixed and the other parameters are left free. As the fitting function models simultaneously both lines, the [^{13}CII] fitting produces a [^{12}CII] profile (scaled by the abundance ratio α^+) that overshoots the observed [^{12}CII] profile. In this example, an excitation temperature of 160 K was used for the background component with an abundance ratio of $\alpha^+ = 67$, keeping the optical depth close to unity.

- Fig. 5.11: The [^{12}CII] remaining emission is fitted by additional background layer components, which, due to their low column density, have a negligi-
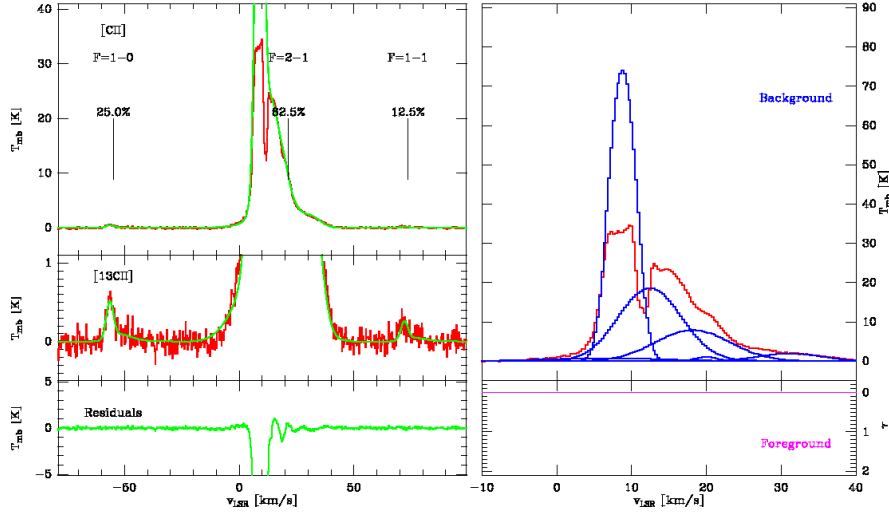
Figure 5.11: Same as Fig. 5.10, but for the second step of the routine, the fitting of the remaining [^{12}CII] background emission

ble contribution to the [^{13}CII] emission, using the smallest possible number of Gaussian components for the fitting. In this example, T_{ex} was fixed to of 150 K for the remaining background components.

- Fig. 5.12: as the fitted line profile of these combined background emission components now overshoots the observed profile in several narrow velocity ranges, the foreground absorption features are fitted, using a fixed low T_{ex}. For this example, T_{ex} was fixed at 20 K for these foreground components. This step is necessary only if the source is affected by self-absorption.

The two layer/multi-component fitting procedure was applied to the [^{12}CII] and [^{13}CII] emission for each position observed in all four sources. The line center optical depth of each component was also calculated from the parameters of the fitting, following Eq. 5.3. For M43 and the Horsehead PDR, as it has seen above, the [^{13}CII] line profiles followed the [^{12}CII] ones and their emissions peaked at the same velocity. Thus, no absorbing foreground layer was needed and the [^{12}CII] and[^{13}CII] emission was modeled by using only a single layer with multiple emission components. In this case, T_{ex} was left as a free fit parameter instead of fixing it. For Mon R2 and M17 SW, the fitting required the inclusion of foreground absorption due to the absorption dips discussed above.

The fitting results are summarized in Tables 5.2 and 5.3. The full set of fit parameters of each component for all positions of the sources is shown in Appendix B.
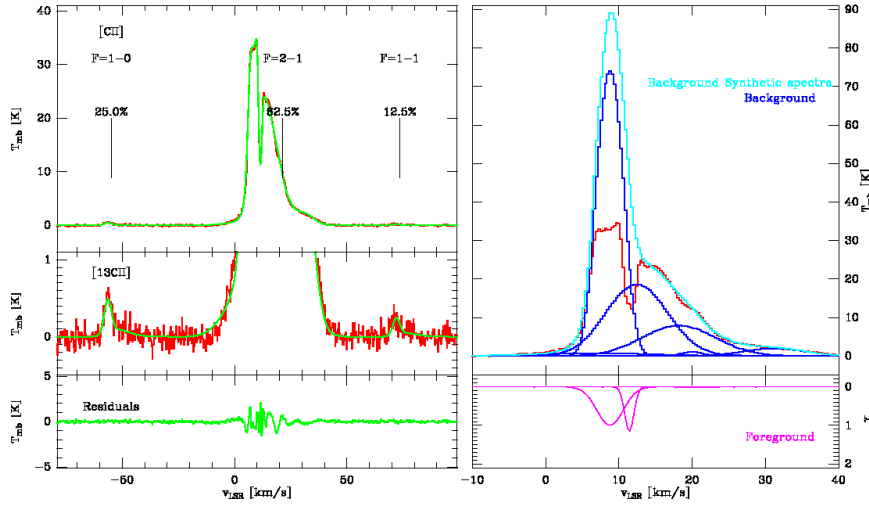
Figure 5.12: Same as Fig. 5.10, but for the last step the routine, the fitting of the
foreground absorbing components

Appendix C shows the resulting components for each fitting. The parameters listed
in each table are the χ^2 of the fit result, a representative excitation temperature for
the background layer ($T_{\text{ex,bg}}$), selected from excitation temperature that traces the
[^{13}CII] emission, and the temperature of the foreground layer component that has
the highest optical depth ($T_{\text{ex,fg}}$). Also, the table shows the total column density
$N_{12}(CII)$ for each layer and the peak optical depth of the component closest in LSR-
velocity to the [^{13}CII] peak temperature for the background (τ^*_{bg}) and foreground
layers (τ^*_{fg}), respectively. These optical depths were selected as representative values
for two reasons: The bulk of the [^{12}CII] emission comes from the material traced
by the [^{13}CII] emission (as shown in Fig. 5.10). And, they are the components that
suffers the largest self-absorption effects. The equivalent visual extinctions corre-
sponding to the [CII] column densities are also shown.

5.3.1   M43 Analysis

The T_{ex} fitted for the components that trace the [^{13}CII] emission was close to 100 K
for the different positions, while the T_{ex} fitted for the [^{12}CII] background emission
not covered within the [^{13}CII] profile was much lower, with values between 30 K and
70 K. Figure 5.13 shows an example of the fitting corresponding to position 0, the
central observed position. The total [^{12}CII] column density for the different positions
varied between 1×10^{18} and 4×10^{18} cm^{-2}, with equivalent visual extinctions between
4.9 and 18.3 mag (Table 5.2).
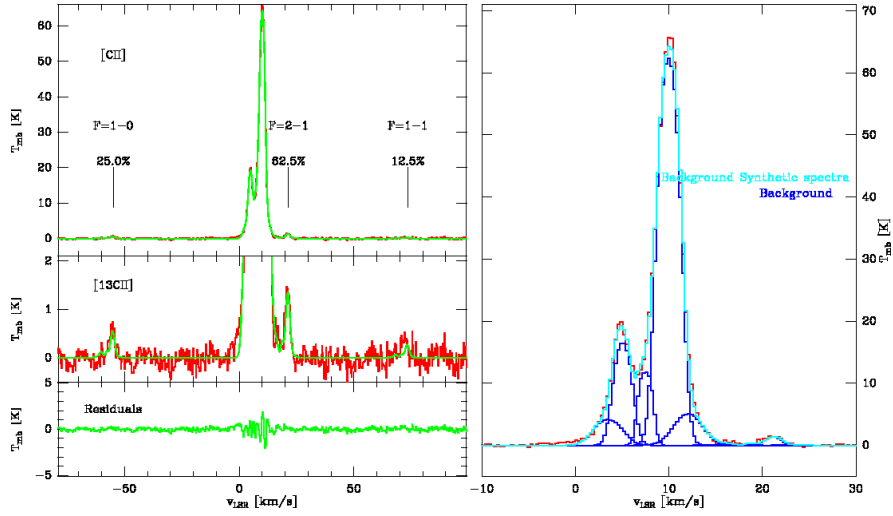
Figure 5.13: Same as Fig. 5.10, but for M43 [^{12}CII] spectra of position 0 with no foreground absorption.

5.3.2 Horsehead PDR Analysis

For the multi-component analysis, the spectra were fitted without applying the wing subtraction through a polynomial. In the Horsehead PDR, due to the blending of the [^{13}CII]$_{F=2\to1}$ satellite with the [^{12}CII] wing at higher LSR-velocities (Fig. 5.3), the wing emission was first fitted with several Gaussian components while masking the [^{13}CII]$_{F=2\to1}$ velocity range. This was necessary because the wing overlapped with the [^{13}CII]$_{F=2\to1}$ emission and it could affect the [^{13}CII] fitting process. Then, the fitting of the [^{12}CII] and [^{13}CII]$_{F=2\to1}$ emission continued. The excitation temperatures were left as a free parameter, resulting in a value for all the components at the different positions of around 30 K. For the positions that are located outside the main interface ridge, positions 1, 4 and 5 (Fig. 4.9), the [^{13}CII]$_{F=2\to1}$ satellite emission was heavily blended with the wing emission, so that column densities fitted for these positions should be considered as a rough estimate, because they are not constrained by the optically thin [^{13}CII] emission. The total [^{12}CII] column densities derived for the different positions were within a range from 3.6×10^{17} cm^{-2} to 1.3×10^{18} cm^{-2} (see Table 5.2), much lower than the ones derived for M43 due to the smaller line widths. The equivalent visual extinctions varied between 1.6 and 5.8 mag. Fig. 5.14 shows an example of the fitting of the position 6.

5.3.3 Monoceros R2 Analysis

For Mon R2, the background T_{ex} was fixed to 150 K and the foreground T_{ex} to 20 K. The total [CII] column density was determined for both positions and each layer.
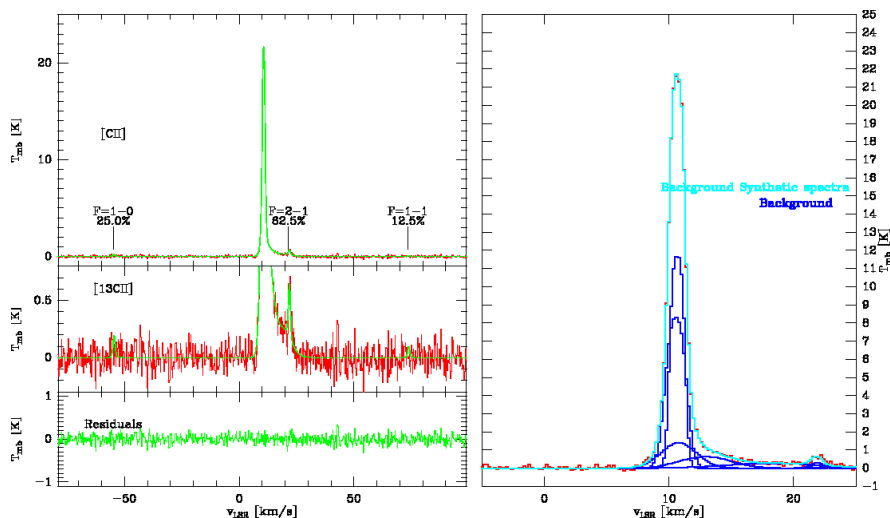
Figure 5.14: Same as Fig. 5.10, but for the Horsehead [^{12}CII] spectra of position 6
with no foreground absorption.

Table 5.2: M43 and the Horsehead PDR column density for the background components

Positions	No. Back. Comp.	χ^2	T_{ex} (K)	Background N_{12}(CII) (cm^{-2})	τ^*	Back. A_V CII (mag.)
M43 0	5	1.7	110.7	4.1E18	2.07	18.3
M43 1	5	1.6	97.3	2.9E18	1.75	12.9
M43 2	2	1.6	60.0	2.5E18	1.43	11.2
M43 3	2	1.2	70.0	1.1E18	0.43	4.9
M43 4	6	1.1	108.4	2.7E18	1.68	12.0
M43 5	4	1.5	108.0	2.0E18	0.96	9.0
M43 6	5	1.1	101.04	3.0E18	1.66	13.4
HOR 0	4	1.2	38.0	7.9E17	2.16	3.6
HOR 1	4	1.1	26.7	5.7E17	0.78	2.5
HOR 2	4	1.2	37.2	8.5E17	1.80	3.8
HOR 3	4	1.4	38.0	6.2E17	1.34	2.8
HOR 4	4	1.3	35.5	4.3E17	0.75	1.9
HOR 5	4	1.4	48.0	3.6E17	0.52	1.6
HOR 6	5	1.0	43.0	1.3E18	2.84	5.8
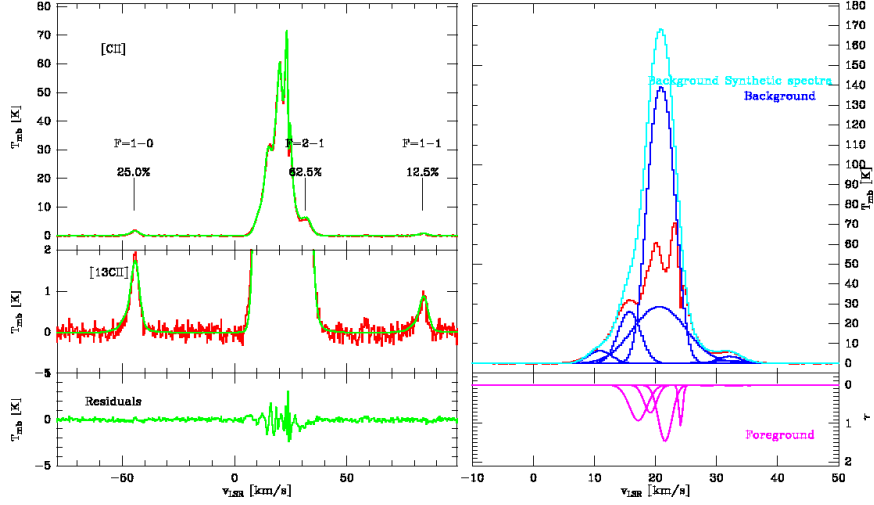
Figure 5.15: Same as Fig. 5.10, but for M17 SW [^{12}CII] spectra of position 6.

For each position, the total background column densities were 4.2×10^{18} cm^{-2} and 4.7×10^{18} cm^{-2} and the total foreground column densities were 8.3×10^{17} cm^{-2} and 6.4×10^{17} cm^{-2}, respectively. The equivalent visual extinction at the positions observed corresponded to 18.7 mag and 21.0 mag for the background, and 3.7 mag and 2.9 mag for the foreground, respectively.

5.3.4 M17 SW Analysis

For M17 SW, the [^{13}CII] emission was fitted using a fixed excitation temperature of 200 K for the background components. A brighter temperature than Mon R2 was selected, because the brighter [^{13}CII] emission required a larger temperature for keeping the optical depth close to unity. For the foreground components, a fixed temperature between 25 and 45 K was used. Figure 5.15 shows the fit results for position 6 as an example; the other positions are shown in detail in Appendixes B and C. Table 5.3 shows the total column density for each of the seven positions. The column densities ranged from 3.0×10^{18} cm^{-2} to 9.2×10^{18} cm^{-2} for the background layer, and from 3.9×10^{17} cm^{-2} to 3×10^{18} cm^{-2} for the foreground layer. The equivalent visual extinctions were between 13.4 mag and 41.0 mag for the background layer, and 1.7 mag to 13.4 mag for the foreground layer.

The multi-component analysis have shown for the sources with absorption dips, that the background layer is composed by high temperature broad emission components with extremely high column density, covering a wide velocity range; and a foreground layer composed by low temperature narrow absorption notches with high column density, restricted to velocities closer to the [^{13}CII] peak. The possible mechanism for reaching high column densities as well as the origin of the fore-

Table 5.3: MonR2 and M17 SW column density for the background and foreground components for the dual layer model

Positions	No. Back. Comp.	No. Fore. Comp.	χ^2	$T_{ex,bg}$ (K)	Background N_{12}(CII) (cm^{-2})	τ^*_{bg}	Back. A_V CII mag.	$T_{ex,fg}$ (K)	Foreground N_{12}(CII) (cm^{-2})	τ^*_{fg}	Fore. A_V CII mag.
MonR2 1	5	2	3.1	160	4.2E18	0.98	18.7	20	8.3E17	0.99	3.7
MonR2 2	6	4	4.1	150	4.7E18	1.03	21.0	20	6.4E17	1.52	2.9
M17SW 0	4	6	1.8	250	9.2E18	1.43	41.0	40	2.0E18	1.63	9.2
M17SW 1	5	4	1.2	200	8.0E18	1.61	35.6	30	1.7E18	1.52	7.6
M17SW 2	4	5	1.3	200	5.6E18	0.84	24.9	30	3.0E18	1.58	13.4
M17SW 3	4	2	3.5	180	4.4E18	0.66	19.6	25	7.7E17	1.61	3.5
M17SW 4	5	5	1.9	200	7.6E18	1.14	33.9	30	1.3E18	0.90	5.8
M17SW 5	4	3	4.5	200	3.0E18	0.24	13.4	30	3.9E17	0.63	1.7
M17SW 6	5	4	1.3	250	7.7E18	1.11	34.3	45	1.8E18	1.46	8.0

ground gas is discussed below in Sect. 5.10.

5.4 Alternative Scenario: Multi-component Single Layer Model

In the multi-component dual-layer scenario, the complex line profiles of Mon R2 and M17 SW have been interpreted as broad emission from the background and narrow absorption notches from cold foreground material. This was not the only possible way of fitting the profiles. An alternative scenario is explored here: a multi-component, but single emission layer model. In order to match the observed profiles, this scenario required the observed [^{13}CII] smooth profiles to be reflected by a similarly broad, but highly optically thick, and therefore flat-topped [^{12}CII] emission profiles. The corresponding gas had to be relatively cold to not overshoot the observed emission. The complex profile shape was then achieved by adding additional narrow line emission components. This alternative scenario is discussed in this section and it was perfectly feasible in terms of obtaining a reasonable fit solution. However, the follow up analysis of the resulting column densities compared to other tracers, as well as the resulting physical scenario, made this solution physically unrealistic.

The resulting multi-component fit, assuming this single layer model, is summarized In Table 5.4, with the number of components per position for each source, the χ^2 of the fitting, the [CII] column density, the peak optical depth and the equivalent visual extinction. As an example of the results, position 2 for Mon R2 is shown in Fig. 5.16 and position 6 for M17 SW is shown in Fig. 5.17. As indicated above, the components were separated into two types. The first type was cold high density gas showing a flat-top [^{12}CII] profile due to high optical depth that contributes to the [^{13}CII] emission. The other type was warmer, lower density gas with much narrower [^{12}CII] profiles tracing the velocity peaks of the [^{12}CII] emission and, due to their low column density, negligible in [^{13}CII].

M17 SW followed this scenario. On the one hand, it had cold components with a $T_{\text{ex}} \sim$ of 50 K, extremely high [CII] column density and a peak optical depth of 14. On the other hand, it had narrow warmer components with an T_{ex} between 50 and 70 K and lower column density, on the order of 10^{17} cm^{-2} per individual component, fitting the [^{12}CII] peaks. The composition was similar for Mon R2 (see the Appendixes B and C for a description of each source).

Note that in this scenario the warm, narrow line components are only visible,
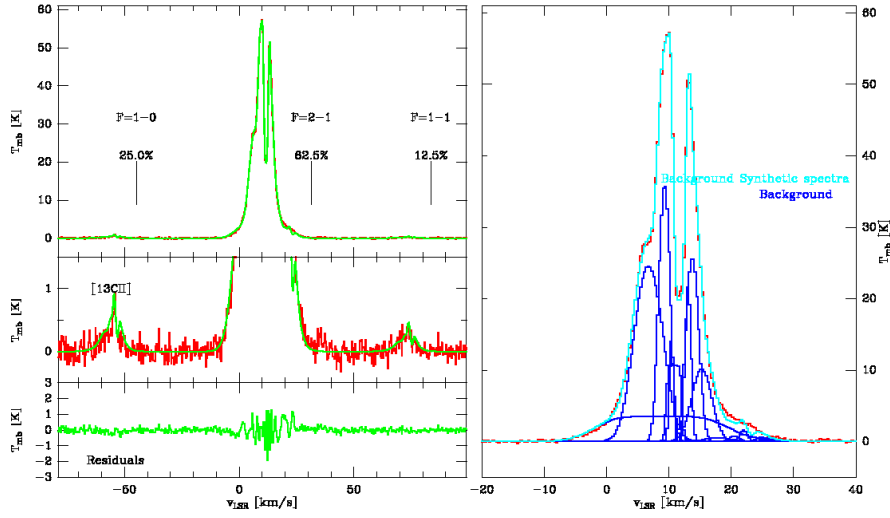
Figure 5.16: Same as Fig. 5.10, but for M17 SW [^{12}CII] spectra of position 6 with no foreground absorption.

when they are located in front of the optically thick low-temperature central emission, as they would otherwise be absorbed away by the central component.

5.5 [^{12}CII]/[^{13}CII] Abundance Ratio

It has been discussed above that the assumption of a simple, single layer PDR model was consistent only for M43 and the Horsehead PDR, due to the absence of self-absorption dips. For Mon R2 and M17 SW, a more complex dual layer model was considered, obtained through the multi-component analysis. The model showed a more consistent picture to illustrate the self-absorption effects through a foreground absorbing layer. The large equivalent visual extinctions imply, at least, several PDR layers along the line of sight in the framework of PDR models. The existence of these layers requires the assumption of clumpiness and the piling of several PDR surfaces along the line of sight. A key point for all this analysis is the assumed [^{12}CII]/[^{13}CII] abundance ratio for the scaling of the [^{13}CII] intensity.

In Section 5.2.1 above, it was discussed how the observed [^{12}CII]/[^{13}CII] abundance ratio is much lower in the line centers than the one assumed for each source. This can be interpreted as an optical depth effect due to self-absorption in the line centers. Towards the line wings the ratio increased, but only in the case of M43, it reached a value close to the assumed abundance ratio for this source. For Mon R2 and M17 SW, the ratio towards the line wings only reached up to about half of the assumed abundance. This is of course linked to the S/N threshold that was applied
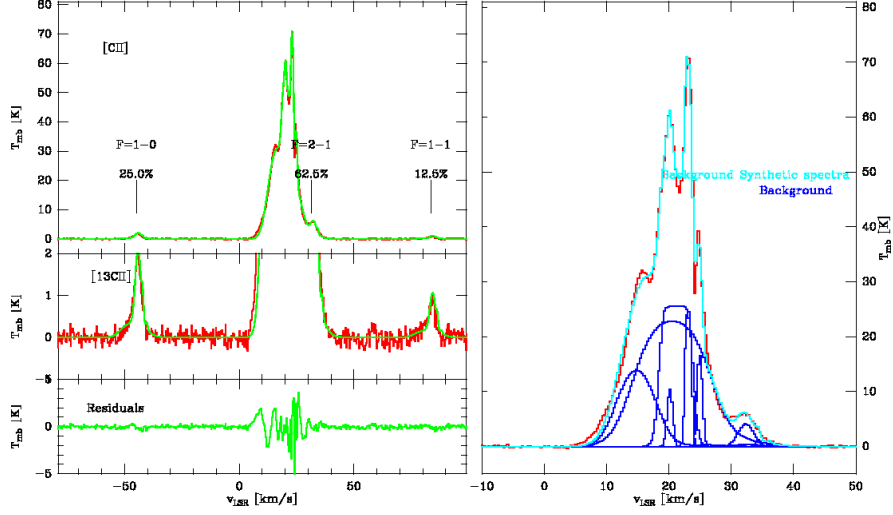
Figure 5.17: Same as Fig. 5.10, but for Mon R2 [^{12}CII] spectra of position 2 with no foreground absorption.

Table 5.4: Mon R2 and M17 SW column density and equivalent extinction for the single layer model

Positions	No. Comp.	χ^2	T_{ex} (K)	N_{12}(CII) (cm^{-2})	τ^*	A_V [CII] (mag.)
MonR2 1	5	12.8	35	7.1E18	2.62	31.7
MonR2 2	8	3.8	40	1.7E19	10.17	75.8
M17SW 0	11	1.3	50	2.6E19	13.88	115.9
M17SW 1	4	1.8	50	2.5E19	14.02	111.4
M17SW 2	7	1.5	45	1.6E19	8.04	71.3
M17SW 3	12	8.0	40	1.1E19	7.26	49.0
M17SW 4	12	1.4	55	1.8E19	7.59	80.2
M17SW 5	9	3.6	55	7.7E18	1.54	34.3
M17SW 6	7	2.9	60	1.5E19	11.26	66.8

to define the useful velocity range: better signal to noise would allow to derive also a ratio further out in the line wings. In fact, for the case of the Horsehead PDR with its relatively weak lines, the signal to noise was sufficient only near the line center and an increase toward the line wings was not observed, because there was no valid data there above the selected threshold.

If the abundance ratio in the source were in fact lower than the assumed literature value, the derived optical depths would be correspondingly lower. Thus, the important question is, whether the derived high optical depths are an artifact, based on an assumed high abundance ratio, or they are real values. Higher sensitivity would increase the useful velocity range and would thus allow to trace the line intensity ratio further out in the line wings. Therefore, it is essential to verify whether the intensity ratio in this regime keeps increasing until it reaches a plateau at the (assumed) value for the ^{12}C$^+$/^{13}C$^+$ abundance ratio, namely α^+.

This scenario was checked for the case of M17 SW by averaging 6 of the 7 positions observed (the ones with high intensity, i.e. excluding position no. 5) and by analyzing the average spectrum. Figure 5.18 shows this average spectrum. For this spectrum, the useful velocity range with a [^{13}CII] intensity above $1.5\,\sigma$ was extended to a range between 10 and 28 km/s. The intensity ratio in the outer wings clearly rose up to values ≈ 45, close to the assumed abundance ratio of 40. This value is higher than the one assumed before, and this could be a sign of fractionation, but the abundance ratio plateau was not reached so the results are not conclusive yet. Also, the value of 40 was derived from analysis of the abundance ratio gradient and not from direct estimations. Further analysis would require direct estimations of the abundance ratio, for both neutral carbon and ionized carbon. Neutral carbon can be estimated from the observations of isotopologues of molecular species that contain carbon, such as CO, HNCO or HCO$^+$. The ionized carbon ratio could be estimated from modeling of the physical conditions of the gas through PDR codes, such as the KOSMA-τ model.

Unfortunately, it was possible to do this test only for the case of M17 SW. For Mon R2, the other source with significant optical depth even in the line wings, and therefore an [^{12}CII]/[^{13}CII] intensity ratio in the wings still below the assumed abundance ratio, there were only two spectra observed with the GREAT L2 single pixel instrument. The average of these two positions did not give a sufficient increase in S/N to allow the tracing of the line intensity ratio further out in the wings. Future observations are needed to check on the assumed abundance ratio also in this and the other sources, as well as further analysis to study this fractionation sign in
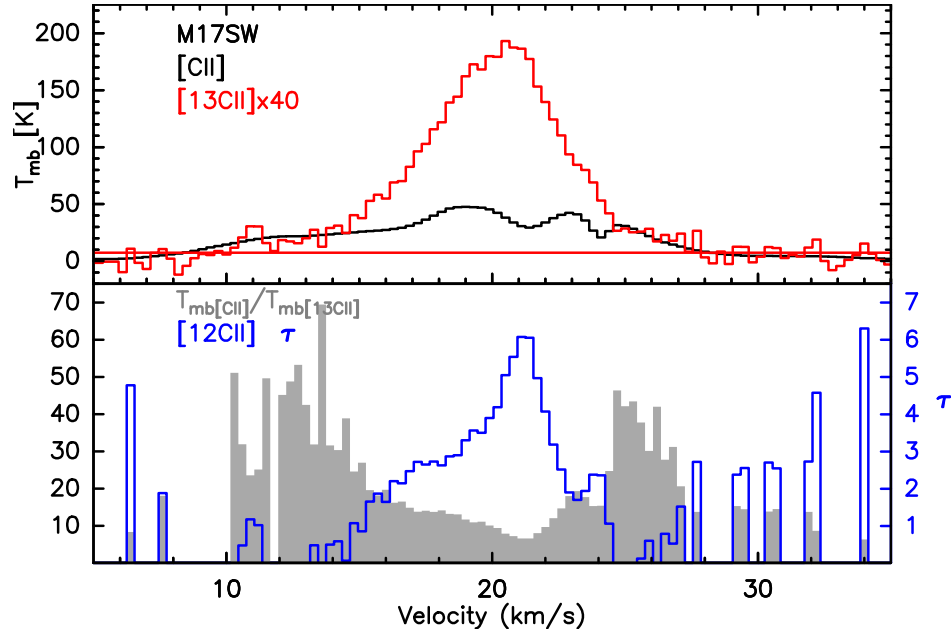
Figure 5.18: Same as Fig. 5.6, but for the M17 SW average spectra of six positions observed by upGREAT.

M17 SW.

5.6 Comparison Between the Single and the Dual Layer Model Against CO

So far, only the physical properties of the [^{12}CII]-emitting gas has been considered. In order to compare the [CII] with the molecular gas traced by CO and its isotopologues, low-J CO rotational line data, including the rare isotopologues of C^{18}O 1-0 for all sources and C^{17}O 1-0 in one source, were used to perform this comparison. The sources available for this were M43, Mon R2 and M17 SW.

For M43, CO data was observed with the Combined Array for Millimeter-Wave Astronomy (CARMA), within the CARMA-NRO Orion Survey project (Kong et al. 2018). The molecular lines observed were ^{13}CO J = 1-0 and C^{18}O J = 1-0 for the seven positions observed in [CII]. Figure 5.19 shows a comparison of the different CO isotopic line profiles against the [^{12}CII] and [^{13}CII] emission. On the one hand, the line profiles of the CO isotopologues and [CII] tended to be similar for the main emission located at 10 km/s, with the [CII] peak shifted to the blue part of the spectra. On the other hand, there was no molecular counterpart to the secondary peak at 4 km/s. The [NII] peaked at the same velocity of the secondary peak (see the analysis below) and the integrated intensity map at that velocity range showed a ring-like
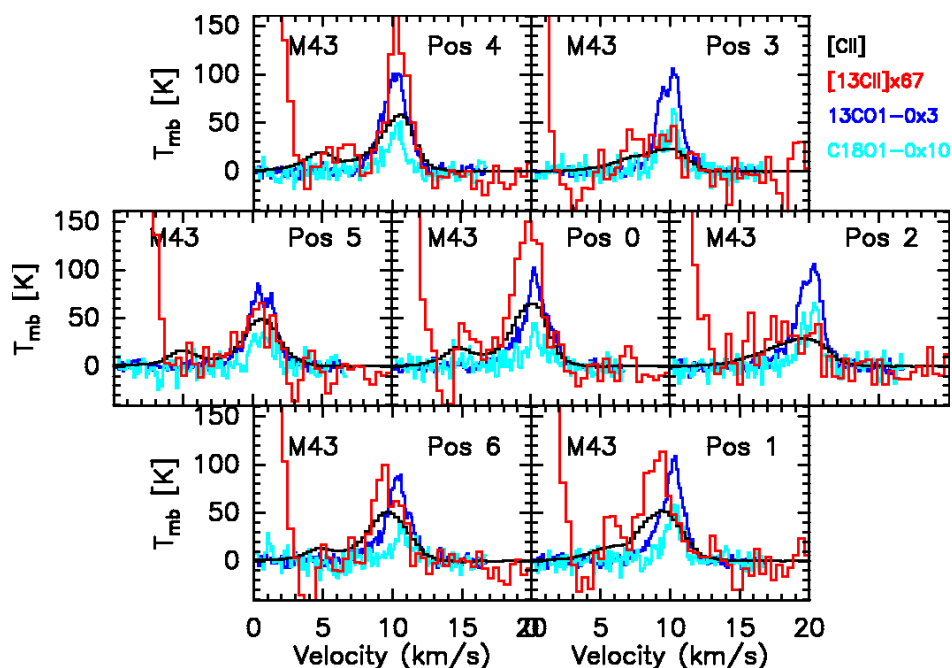
Figure 5.19: M43 line profile comparison between [^{12}CII] (in black), [^{13}CII] (in red),
scaled up by α^+, CO (1-0) (in green), ^{13}CO (1-0) (in blue) and C^{18}O (1-0) (in cyan).
CO and its isotopologues have been scaled up by the factors indicated only to be
compared with [^{13}CII].

structure, see Fig. 5.20. This can be interpreted as that the gas at the secondary peak
corresponds to ionized material, meanwhile the gas at 10 km/s correlates with the
molecular region traced by CO.

For Mon R2, the published data by Ginard et al. (2012) at the two positions ob-
served in [CII] was used. The molecular lines available were ^{13}CO J = 1-0 and C^{18}O
J = 1-0 observed with the EMIR receiver (Carter et al. 2012) at the IRAM 30 m tele-
scope. The CO isotopologues (Fig. 5.21) showed a similar profile to the [^{13}CII] emis-
sion at the 10 km/s peak, with the [CII] emission more extended at higher velocities.
There was no molecular emission at 15 km/s; so, it is safe to assume that this higher
velocity gas correlates with ionized gas due to the absence of molecular gas.

For M17 SW, the published data from Pérez-Beaupuits et al. (2015b) at the seven
positions observed in [CII] were used. The CO isotopologue lines available were
^{13}CO J = 3-2, observed with FLASH (Heyminck et al. 2006) at the APEX telescope
(Güsten et al. 2006), C^{18}O J = 1-0 and C^{17}O J = 1-0, observed with the EMIR re-
ceiver at the IRAM 30 m telescope. Even if the molecular tracers were low-J CO,
Pérez-Beaupuits et al. (2015a) compared the CO emission of different transitions for
different positions from CO J = 1-0 up to CO J = 16-15. The line profile of the differ-
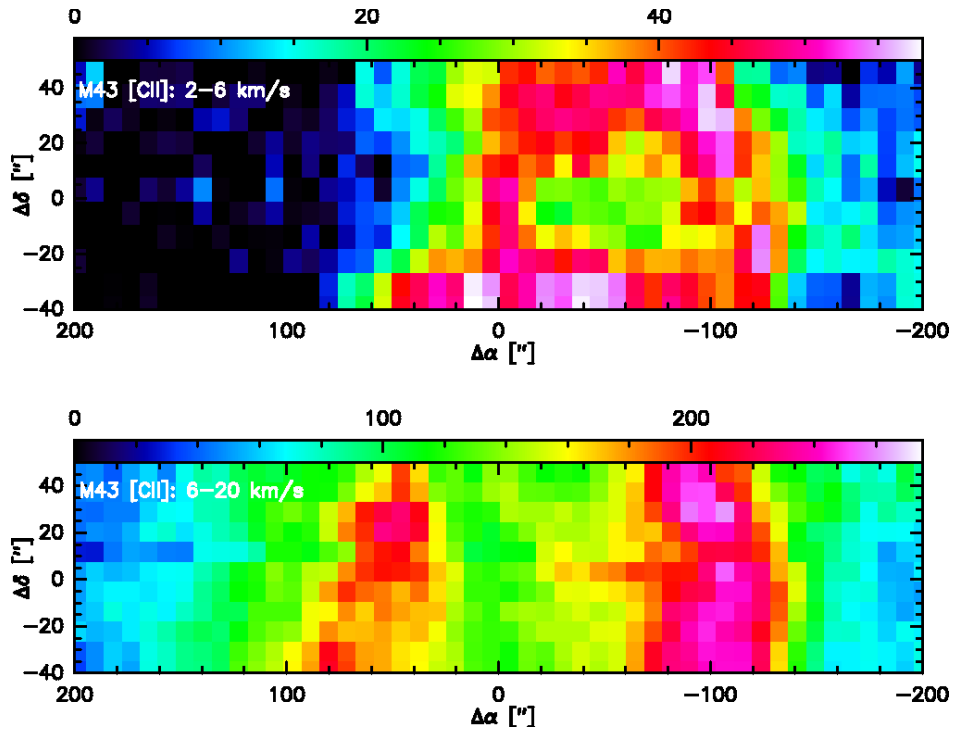
Figure 5.20: *Top* - M43 [CII] integrated intensity map between 2 and 6 km/s. *Bottom* - Same as before but between 6 and 20 km/s.
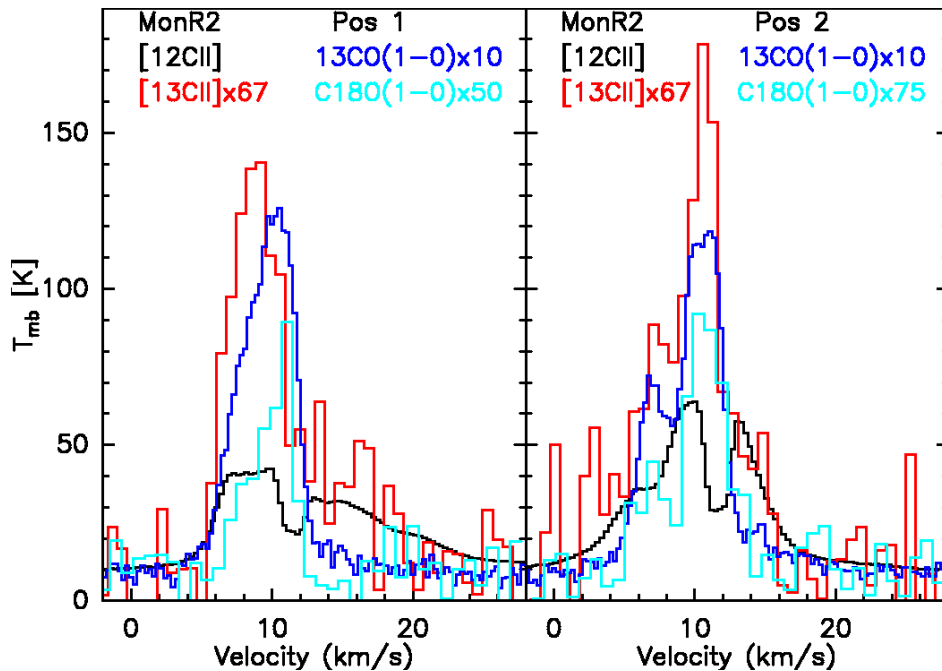
Figure 5.21: Mon R2 comparison between [^{12}CII] in black, [^{13}CII] in red scaled up using α, ^{13}CO (1-0) in blue and C^{18}O (1-0) in cyan. CO and its isotopologues has been scaled up only to be compared with [^{13}CII]. [^{13}CII] has been smoothed for display purposes.
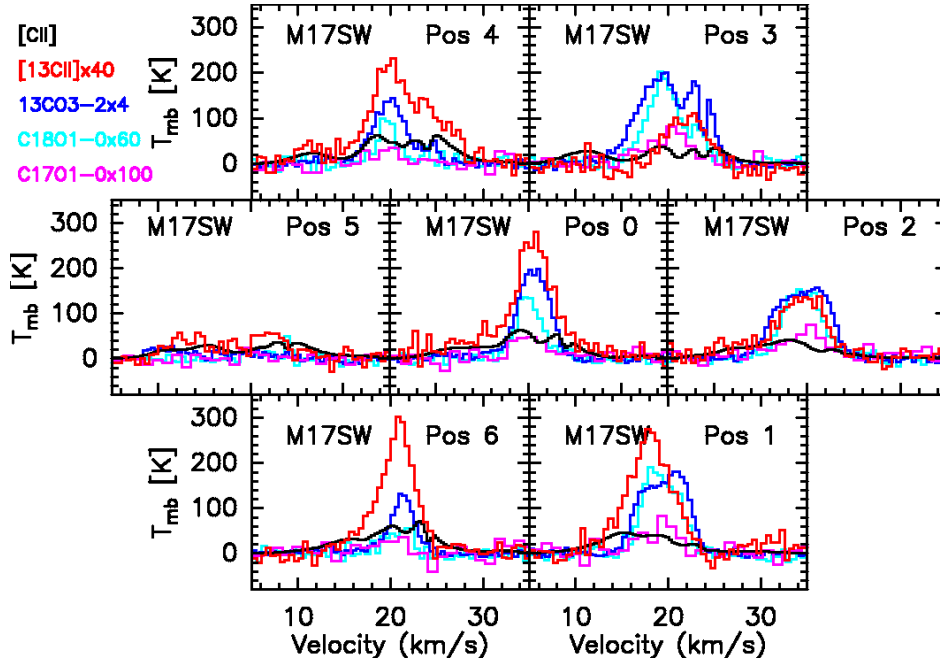
Figure 5.22: M17 SW comparison between [^{12}CII] in black, [^{13}CII] in red scaled up using α, ^{13}CO (3-2) in blue, C^{18}O (1-0) in cyan and C^{17}O (1-0) in purple. CO and its isotopologues has been scaled up only to be compared with [^{13}CII].

ent CO transitions were similar among them. This allowed to use the available low-J CO data with confidence for the comparison with [CII]. Figure. 5.22 shows the comparison between the different line profiles of the different species. The comparison between the molecular and the [CII] showed that the molecular emission correlated with the [CII] gas only in the central velocities where the [^{13}CII] emission peaks. But at lower velocities (lower than 15 km/s) there was no molecular emission. From the comparison against [NII], as can be seen below, [NII] peaked at 0 km/s, with a long wing from 0 to 20 km/s. Therefore, this correlation suggested that the ionized gas is located at 0 km/s and has only weak [CII] emission associated. For larger velocities, the emission got associated with the molecular region, showing the transition from the ionized to the molecular regime. This scenario had already been studied by Pérez-Beaupuits et al. (2015b). They found correlations between [CII] and HI emission at 10 km/s, with molecular material at 20 km/s and ionized at 30 km/s from the residuals. In comparison, from the observations available for this work, HII was found 0 km/s (traced by [NII]), molecular H$_2$ at 20 km/s and HI at 10 km/s from the remaining emission. For velocities higher than 25 km/s is only possible to affirm that [CII] does not correlate with any other tracer.

Figures 5.23 and 5.24 show the M17 SW line profiles of the dual and the single layer [^{12}CII] models against the C^{18}O 1-0 emission profiles (scaled up to match
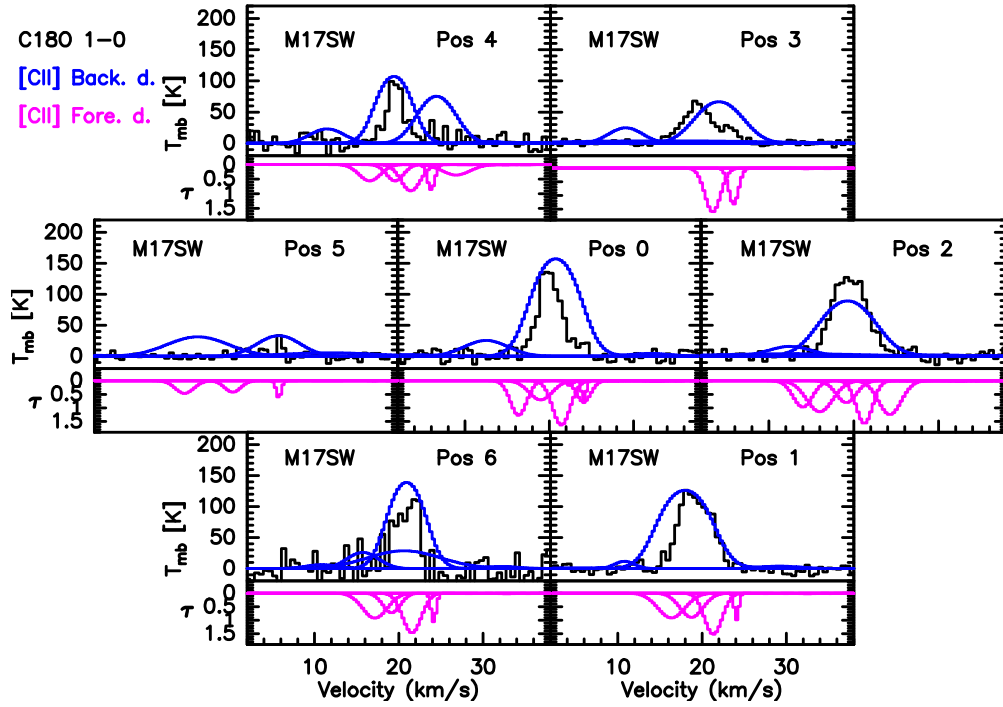
Figure 5.23: Comparison between $C^{18}O$ J = 1-0 and the $[^{12}CII]$ Gaussian components from the dual layer model. Scaled up $C^{18}O$ observations are in black, $[^{12}CII]$ background components are in blue and $[^{12}CII]$ foreground optical depth components are in pink.

the [CII] components), respectively. The comparison between the dual layer and the molecular emission showed that, in the dual layer model, the brightest background emission component in $[^{12}CII]$ had a line profile that, though wider in velocity, shared a similar line profile with the $C^{18}O$ emission profile at the central line velocities that correlate with the molecular emission. The $[^{12}CII]$ absorption dips also showed profiles that partially match the $C^{18}O$ emission. On the contrary, the single layer model needed cold and high density [CII] emission components without any correlation to the $C^{18}O$ emission profile. In particular, it would be expected that the high density cold components (labeled "[CII] high d." in Fig. 5.24) would correlate with the molecular gas, being closer in their physical conditions. Similarly, the bright, narrow, lower density and warmer emission ([CII] low d.) notches at various velocities did not correlate with the $C^{18}O$ emission. This comparison suggests that the single layer model, even if formally providing a good fit, is physically less plausible.

From the $C^{18}O$ J = 1-0 observations, the $C^{18}O$ column density was estimated for all available sources and each position, following Mangum & Shirley (2015) and Schneider et al. (2016b). For the excitation temperature, the values of the dust tem-
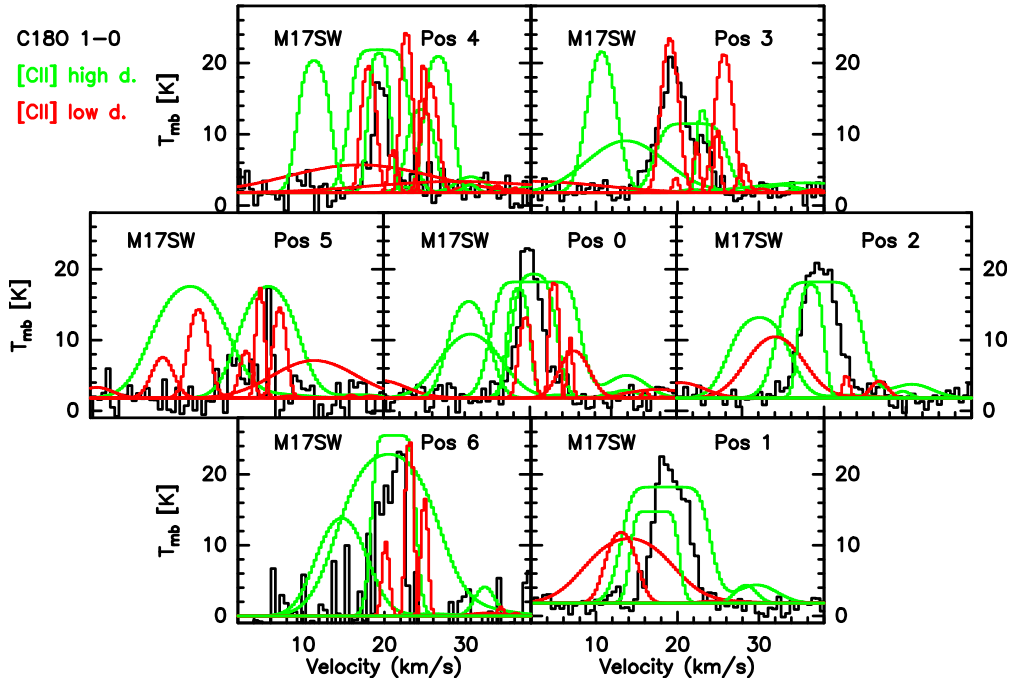
Figure 5.24: Comparison between C^{18}O J = 1-0 and the [^{12}CII] Gaussian components from the single layer model. Scaled up C^{18}O observations are in black, [^{12}CII] high density low temperature components are in green ([CII] high d.) and [^{12}CII] low density high temperature components are in red ([CII] low d.

peratures were used, obtained from the Herschel Gould Belt (André et al. 2010) and HOBYS (Motte et al. 2010) imaging key programs and published by Stutz & Kainulainen (2015) for M43, Rayner et al. (2017) for Mon R2, and Schneider, priv. comm. for M17 SW. Typical dust temperatures in regions of peak [CII] emission are 16 K for M43, 26 K for Mon R2 and 35 K for M17 SW, respectively. Using these dust temperatures as the C^{18}O excitation temperature (assuming the gas and dust are well mixed), the C^{18}O column densities were derived and listed in Table 5.5. The column densities were also converted to an equivalent H$_2$ column density, assuming an ^{16}O/^{18}O ratio of 490 for M43, 500 for Mon R2 and 425 for M17 SW according to Wilson & Rood (1994), and an assumed CO/H$_2$ ratio of 1.2×10^{-4} (Wakelam & Herbst 2008). Also, it was assumed that all carbon in the molecular region is in molecular form as CO. Finally, the equivalent visual extinctions were estimated knowing that 2N(H$_2$) = 1.87×10^{21} cm^{-2} A$_V$. As an independent verification, the dust column densities derived from Herschel were checked. The dust column densities agreed within 30% with the values determined from C^{18}O using these excitation temperatures.

From here, a comparison was done between the equivalent extinctions (or for that matter, the derived H$_2$ column densities) estimated from [CII] and the CO isotopologues lines for both models. The comparison is shown in Figure 5.25. For po-

Table 5.5: M43, Mon R2 and M17 SW $C^{18}O$ 1-0 column density and equivalent extinction

Positions	$N(C^{18}O)$	$N(H_2)$ $C^{18}O$	A_V $C^{18}O$
	(cm^{-2})	(cm^{-2})	(mag.)
M43 0	1.16E16	4.75E22	50.8
M43 1	1.44E16	5.88E22	62.9
M43 2	1.50E16	6.13E22	65.6
M43 3	1.42E16	5.80E22	62.1
M43 4	9.89E15	4.03E22	43.2
M43 5	7.46E15	3.05E22	32.6
M43 6	8.00E15	3.27E22	34.9
MonR2 1	8.98E15	3.74E22	40.0
MonR2 2	9.99E15	4.16E22	44.5
M17SW 0	2.00E16	7.07E22	75.6
M17SW 1	3.39E16	1.20E23	128.2
M17SW 2	3.33E16	1.18E23	126.1
M17SW 3	3.82E16	1.35E23	144.6
M17SW 4	1.67E16	5.92E22	63.3
M17SW 5	2.49E15	8.83E21	9.4
M17SW 6	6.20E15	2.19E22	23.5

sition 5 and 6, the [CII] equivalent A_V were higher, for both model scenarios, than the ones estimated from $C^{18}O$. This was no surprise, because from velocity channel maps between the molecular and ionized line observations (Pérez-Beaupuits et al. 2015b), these positions were located off the main molecular ridge and hence, dominated by PDR material. For the other positions, the equivalent A_V of the [CII] layer estimated for the single layer model were similar or even higher than the ones derived from the $C^{18}O$ emission, whereas the dual layer [CII] emission model gave much lower equivalent [CII] column densities, on average 25% of the molecular column densities.

This comparison showed that the single layer model requires extremely high column densities for [CII] in comparison to CO. These conditions are unlikely to be present in a dense, high extinction cloud core traced by $C^{18}O$ and $C^{17}O$. This would require to have molecular column densities corresponding to visual extinctions of up to 100 A_V. In addition, these high column densities of [CII] for the single layer model, would be required to have, in the bulk of the emission, low excitation temperature of around 50 K (see above); there is no reasonable physical scenario that can explain these properties. In a PDR, it is expected that the largest amount of hydrogen is located in the molecular core in molecular form. The single layer scenario
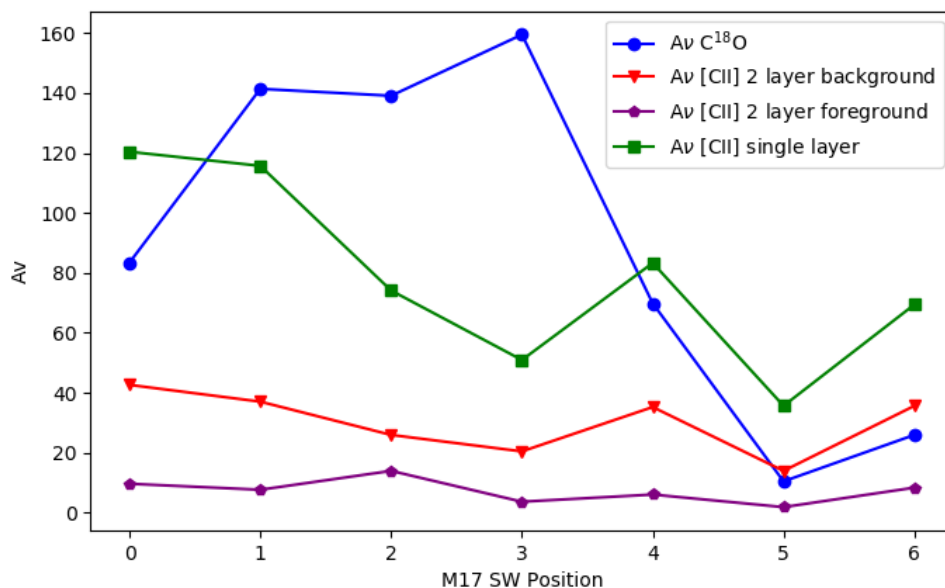
Figure 5.25: M17 SW Av comparison between the extinction of C^{18}O, the [CII] from
both the background and foreground layers of the dual layer model and the [CII]
from the single layer model.

showed the opposite scenario, with large amounts of material in the form of CO-
dark gas. But, it is known that for M17 SW, even when it is affected by a strong UV
field, the molecular gas is clumpy and the CO presents high column density and
optically thick emission, proof enough that the molecular gas is shielded from the
UV field. Hence, the single layer model was ruled out for M17 SW.

For Mon R2, the situation was similar. The equivalent visual extinctions of the
molecular gas traced by C^{18}O were 40.0 for position 1 and 44.5 mag for position 2,
whereas the single layer scenario gave an equivalent A$_V$ of the [CII] emission of 31.7
and 75.8 mag, respectively. The dual layer scenario had significantly lower, although
still relatively high equivalent visual extinctions, 21 mag for the warm background
and 3 mag for the foreground [CII] emission. As in the case of M17 SW, the single
layer scenarios would thus require to have a column of [CII] emission at relatively
low T$_{\text{ex}}$ that is about equally large to that of the molecular gas.

In resume, the single layer model can be ruled out for several reasons. The phys-
ical conditions required to model the [^{12}CII] line profile are extremely improbable,
with low temperature and high column density [CII] components accompanied by
warmer and narrow low density bright notches. This would require the presence of
extended and cold high density ionized gas surrounded by small clumps of bright

low density ionized material, a scenario physically very unlikely. Also, the molecular line emission profile traced in CO do not match the single layer model [CII] emission profile, the latter showing high column density velocity components that are not at all matched by the molecular emission. In contrast, the velocity components with the bulk of the column density, matched much better between the molecular emission and the [CII] emission for the dual layer scenario. Moreover, the equivalent visual extinction derived for the [CII] emission in the single layer model would be equal or even exceeding the one derived from molecular emission, with the implausible scenario of much more hydrogen in the form of CO-dark gas gas visible in CO, therefore, the single layer model was discarded, although it provided a formally fitting scenario, as physically unlikely.

5.7 [NII] Observations

[NII] 205 μm fine structure line observations were done for the central position of M43, the Horsehead PDR and M17 SW during the [CII] SOFIA/upGREAT observations. For this reason, a simply analysis was made for these observations, with a discussion about their line profiles and a estimation of the [NII] column density. A comparison between the [NII] and [CII] line profiles are shown in Fig. 5.26. For M43, the [NII] emission was shifted to the blue side of the spectra with respect to the [^{12}CII] peak and it had a T_{peak} of 0.5 K at 4 km/s. For the Horsehead PDR, the [NII] emission was shifted to the red side of the spectra with respect to the [^{12}CII] peak. And for M17 SW, the [NII] emission was shifted to the blue side of the spectra with respect the [^{12}CII] emission. The different velocity distributions were an indication that the [NII] emission originates in a separate component of the cloud, likely the HII region.

The [NII] column densities were estimated from Eq. 2.59 in the optically thin limit. Due to the dependency of the fractional population of the different N^+ states to the electron density of the gas, a kinetic temperature of 8000 K and a fractional population of 0.45 were assumed. The assumed values for the estimation of the column density can only give a lower limit. Additionally, assuming that all the nitrogen is ionized, the ionized hydrogen column density and its equivalent visual extinction were estimated. Using a N/H abundance ratio of 5.1×10^{-5} (Jensen et al. 2007) and an $A_V = N(H)/1.87E21$, the above mentioned values were derived and they are given in Table 5.6.

The [NII] emission for the three sources had, compared to [CII], much lower column densities and hence, lower equivalent visual extinctions. Thus, the [NII]
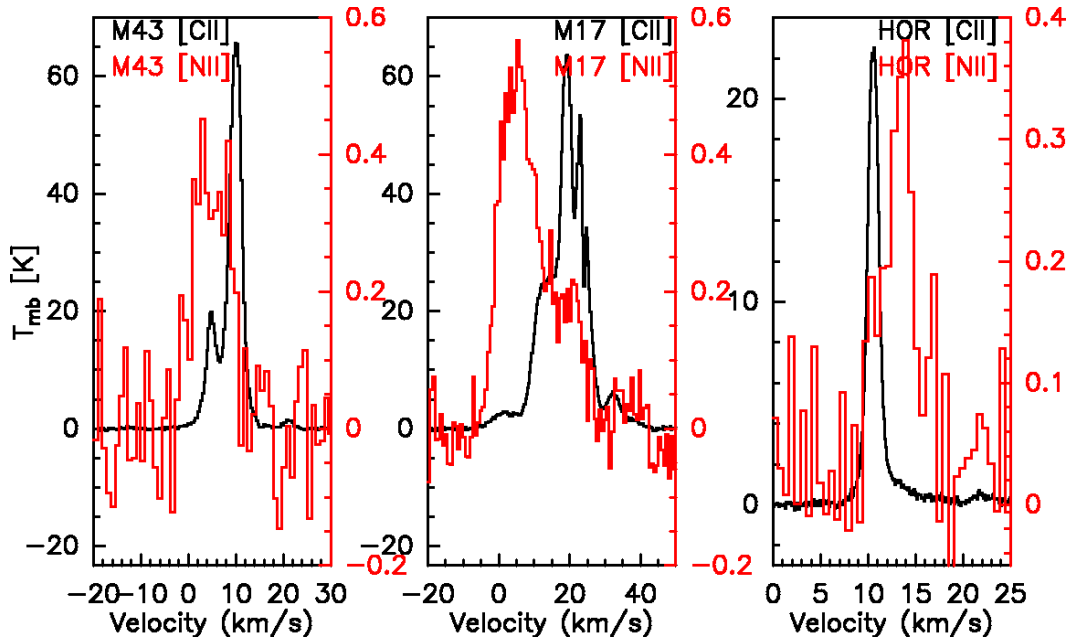
Figure 5.26: [CII] and [NII] emission for the central pixel for the 3 sources, M43,
M17 SW and the Horsehead PDR.

Table 5.6: M43, the Horsehead PDR and M17 SW [NII] column densities and equiv-
alent extinction for the central pixel of the upGREAT array.

Sources	N(NII)	N(H$^+$) [NII]	A$_V$ [NII]
	(cm^{-2})	(cm^{-2})	(mag.)
M43	1.43E16	2.80E20	0.14
HOR PDR	1.21E16	2.37E20	0.13
M17 SW	3.84E16	7.53E20	0.40

emission was consistent with its origin in the HII region. When the HII region is visible in the optical, it is located in front of the molecular emission and its emission is expected to be displaced to the blue side of the spectra; this is indeed what was found for M43 and M17 SW. The Horsehead PDR, in contrast, is visible as a dark cloud against the background HII region, which is located behind the molecular cloud; correspondingly, its [NII] emission was red-shifted with respect to [CII].

An interesting question is whether the ionized emission originates from inside the HII region, or whether it is part of an ionized photoevaporation flow. Such flows are ionized material that come from the molecular region and flow back into the ionized region as a result of the hit of the ionization front into the the molecular region. As a result, a shift for the emission in velocity with respect to the molecular gas is expected. Facchini et al. (2016) estimated a shift in velocity of 1 km/s for the ionized emission when molecules are dissociated, but for the case of protoplanetary disks. Henney et al. (2005) estimated a shift of 10 km/s over large volumes of material, and even up to 17 km/s in dense and magnetized molecular globules (Henney et al. 2009). It was found that the [NII] emission was shifted 8 km/s for M43 and 15 km/s for M17 SW with respect to the molecular emission, inside the range discussed above. For the Horsehead PDR, the [NII] emission was shifted 5 km/s with respect to [CII]. The most probable scenario for an origin of the [NII] emission is a combination of ionized gas from the HII region, and from a photoevaporation flow. For M17 SW, in particular, it could be that the emission peaking at 0 km/s originates from the HII region, whereas the emission at 15 km/s where there is a secondary peak or even a plateau, originates from the photoevaporation flow. However, this is speculative and more evidence is required.

5.8 M17 SW HI Comparison

In the case of M17 SW, an HI absorption spectrum was extracted from the HI-OH-Recombination line survey of the inner Milky Way (THOR, Beuther et al. 2016), and compared the velocity profile with its corresponding counterparts in [CII] and [NII]. The position corresponded to the [CII] position 0 (Fig. 4.11). Figure 5.27 shows that the HI emission is much more extended in velocity, embracing both the [CII] and [NII] emissions. The HI spectrum peaked at 20 kms/s, the same velocity as the [CII] peak emission, and it had an asymmetric profile with a long wing at lower velocities, matching at 0 kms/s the low intensity emission of the weak [NII].
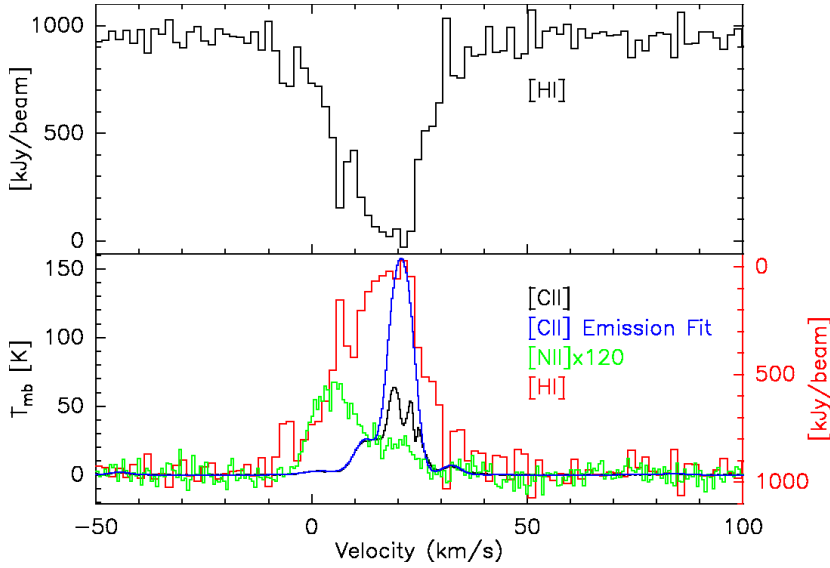
Figure 5.27: *Top* - M17 SW position 0 HI absorption spectra. *Bottom* - M17 SW po-
sition 6 [CII] spectra for the observed and calculated background emission, respec-
tively, [NII] and an inverted HI spectra for profile comparison.

5.9 Beam Filling and Absorption Factor Effects

In the following, there is a discussion of how a beam filling factor Φ_{ff} (fraction of
the telescope beam filled by the source defined in Section 4.1) smaller than unity
changes the derived physical properties. The multi-component source model has to
consider, in principle, individual beam filling factors for each component. However,
this would result in a too large number of free parameters in the fitting. Hence, the
discussion was restricted to using one single beam filling factor that was applied
to all background emission components in common. For the background emis-
sion component, the main effect of a beam filling factor smaller than unity was to
raise the source intrinsic brightness, thus requiring higher excitation temperatures
and/or higher optical depth to reach the higher brightness. To first order, both ef-
fects resulted in a larger column density of the emitting material, raising inversely
proportional to the beam filling factor, so that the beam average column density
stayed constant to first order.

To quantify this, as a first step, a multi-component fit was performed, adding as
an extra parameter a fixed value Φ_{ff} for the background layer in emission, decreas-
ing it step by step. Position 6 of the Horsehead PDR was used for the beam filling
factor analysis. As expected, a decrease in Φ_{ff} increased the excitation temperature,
column density and optical depth of the background emission. For example, fix-
ing Φ_{ff} at 0.5 increased the T_{ex} from the original fit ($\Phi_{ff} = 1$) between 15 K and 20
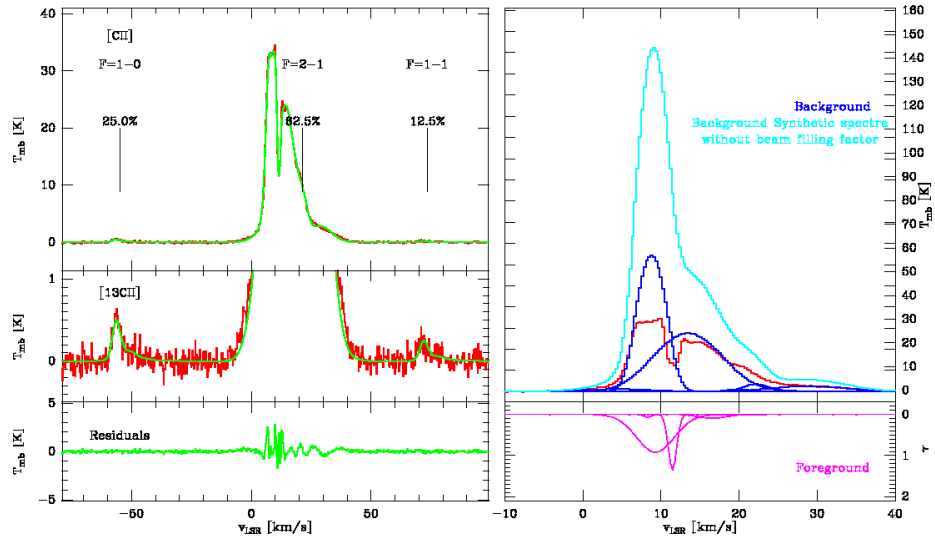
Figure 5.28: Same as Fig. 5.10, but for Mon R2 [^{12}CII] spectra at position 1 fitted with a beam filling factor of 0.5

K (from 43 K to 60 to 65 K) and the total column density changes from 1.3×10^{18} to 1.4×10^{18} cm^{-2}. An even lower value of $\Phi_{ff} = 0.3$, resulted in an increment for the T_{ex} between 20 and 30 K and a [CII] column density of 1.7×10^{18} cm^{-2}. Table 5.7 shows a summary of the effects of the variations over Φ_{ff}.

Then, the next step was to consider that foreground absorption was present. For this, position 1 of Mon R2 was used as a test case. The resulting fits are shown in Fig. 5.28 and Table 5.7. Fixing Φ_{ff} to 0.5 produced the same changes for the background layer as expected from the Horsehead PDR analysis, namely an increase of 50% for the excitation temperature, and 100% for the column density and the optical depth. Then, for the foreground layer, there was also an increase of the column density and optical depth similar to the ones of the background layer, 50% and 100%, respectively. This was because the increase in the background required a corresponding increase in the absorption of the foreground to obtain the same observed T_{mb}. Due to the higher brightness of the background, even a slightly increased excitation temperature of the foreground absorbing layer can be tolerated to give the same beam average brightness in the center of the absorption dip. Therefore, the introduction of a Φ_{ff} allowed to increase the excitation temperature and in particular, the column density of the background layer, as well as both parameters for the foreground layer, without affecting the observed main beam temperature.

Then, a even more complex case for the analysis was considered. The case was that the foreground absorption material only partially covers the background emission. To take this into account, an absorption factor Φ_{af} was defined. The absorption factor represents the fraction of the background emission layer absorbed by the fore-
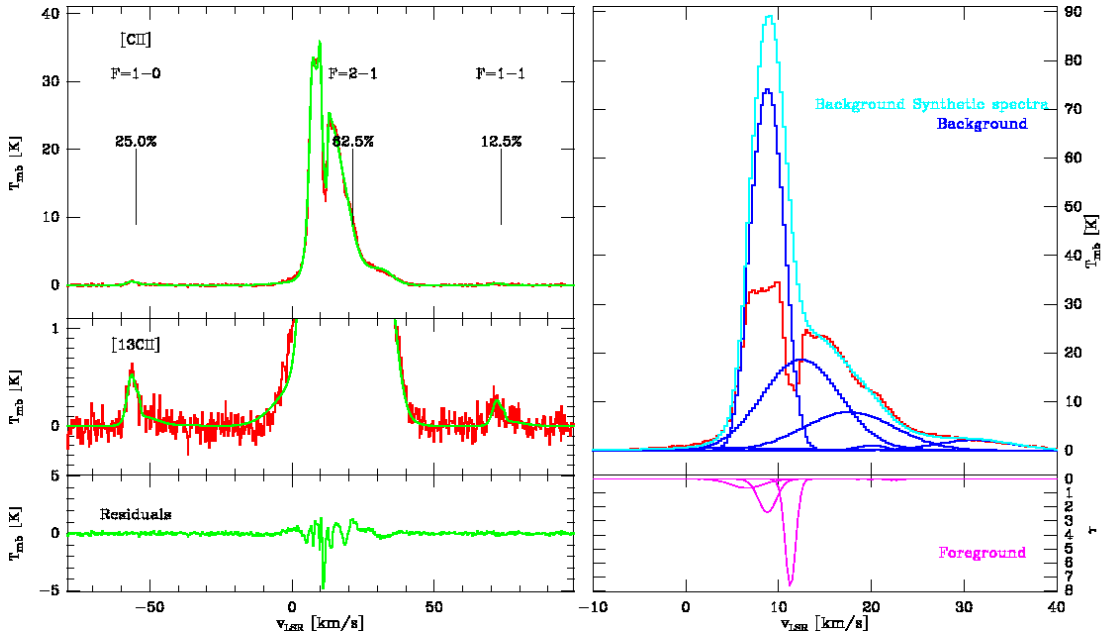
Figure 5.29: Same as Fig. 5.10, but fot MonR2 [^{12}CII] spectra at position 1, fitted with an foreground absorption factor of 0.75 for the 3 main background components

ground layer. Position 1 from Mon R2 was selected as a source with self-absorption to study this effect, similar to before.

The analysis started with a value of 0.9 for Φ_{af} for the three main background components. It was found that, naturally, the background remained the same, and the foreground column density and optical depth increased. The foreground $N_{12,i}$(CII) increased from 8.3×10^{17} to 2.0×10^{18} cm^{-2} and the optical depth from 0.99 to 6.26. This was plausible, as the smaller fraction of absorption had to compensate the fact that a fraction of the bright background emission was not absorbed by the foreground. Then, Φ_{af} was decreased further down to 0.75. This was the lowest limit possible, because for values lower than this one, the 25% of the background that was not absorbed could not be compensated even, by a complete absorption (down to zero brightness) of the foreground layer. In this limiting case, the foreground $N_{12,i}$(CII) increased even more, to 2.9×10^{18} cm^{-2}, same situation as the optical depth that increased to 7.72. In resume, the introduction of an absorption factor Φ_{af} increases the column density and the optical depth of the foreground material, without affecting much the excitation temperature, becoming the foreground layer much more massive and thick.

In conclusion, the introduction of both a foreground and background filling factor less than unity leads to an increase in the excitation temperature of the background component and the column density for both layers, in particular the foreground absorbing layer. With the current beam resolution, it is not possible to con-

Table 5.7: Fit parameters derived for the case of background and foreground filling factors as discussed in the text for position 6 in the Horsehead PDR and position 1 of MonR2.

Sources	No. Back. Comp.	No. Fore. Comp.	χ^2	$T_{ex,bg}$ (K)	Background $N_{12,i}$(CII) (cm^{-2})	τ^*_{bg}	Back. A_V CII (mag.)	$T_{ex,fg}$ (K)	Foreground $N_{12,i}$(CII) (cm^{-2})	τ^*_{fg}	Fore. A_V CII (mag.)
HOR Φ_{ff} 0.5	5	-	1.5	57.0	1.4E18	3.07	7.1	-	-	-	-
HOR Φ_{ff} 0.3	4	-	1.5	73.4	1.7E18	3.19	9.0	-	-	-	-
MonR2 Φ_{ff} 0.5	5	2	2.3	220.0	8.4E18	1.28	44.9	40.0	1.2E18	1.34	6.4
MonR2 Φ_{af} 0.9	5	4	1.6	160.0	4.2E18	0.98	22.6	35.0	2.0E18	6.26	10.8
MonR2 Φ_{af} 0.75	5	3	3.4	160.0	4.2E18	0.98	22.6	30.0	2.9E18	7.72	15.3

strain the beam filling factor for the [CII] emission, neither the absorption factor. The analysis above, however, showed that the excitation temperatures and column densities of the background layers are lower limits, and for the absorbing foreground, the excitation temperatures derived with a unity filling factor are upper limits, while the absorbing foreground column densities are lower limits.

5.10   Origin of the Gas

The high column densities of the warm background layer in M43, Mon R2 and M17 SW are difficult to explain in the context of standard PDR-models and ISM phases. In this scenario, the C$^+$ layer in a single PDR layer has typically an A$_v$ of a few magnitudes(Hollenbach & Tielens 1997). The large values for the C$^+$ column density derived here, with equivalent visual extinctions up to 43 mag, thus require tens of layers of C$^+$ stacked on top of each other along the line of sight. This may be possible if the cloud material is very clumpy and fractal with a large fraction of the total cloud material being located in UV-affected clump surfaces. This scenario can be possible, in particular for M17 SW with its edge-on geometry and known complex structure. Non standard PDR scenarios might apply; for example, Pellegrini et al. (2007) proposed for M17 SW that a high column density of the PDR layer can be obtained by including magnetic fields, raising the pressure and density of the heated gas.

For the foreground material, the situation is much more puzzling: the observed line profiles need ionized gas with high column densities of C$^+$ at an T$_{ex}$ much lower than possible in PDR scenarios. It is only possible to speculate about its origin: a high X-ray or cosmic ray emission might keep a high fraction of ionized carbon in dense, cold clouds, as long as cooling is efficient to avoid heating through the ionization. For all three sources, for which foreground [^{12}CII] absorption was observed, namely the two presented in this work, Mon R2 and M17 SW, and also NGC 20204 (Graf et al. 2012), there is evidence for a high Y-ray and/or CR flux: M17 SW shows strong emission of X-rays due to the large number of young stars (Broos et al. 2007), Mon R2, has an enhanced X-rays flux coming from T Tauri stars (Gregorio-Hetem et al. 1998; Nakajima et al. 2003), and NGC-2024 also has strong X-ray activity (Skinner et al. 2003).

Even if the nature of the high column density foreground gas is unknown, there is evidence that it is not diffuse, low T$_{ex}$ ionized gas. There are variations in both the line profiles and the absorption patterns between the different observed positions, separated by only 30″. Figures 5.30 and 5.31 show the line profile for the

optical depth for Mon R2 and M17 SW, respectively. It can be seen, even if certain positions share similarities between them, that there are variations in intensity and velocity between the different components. The separation between the positions corresponded to a distance of 0.27 pc for M17 SW and 0.12 pc for Mon R2. The spatial extend of the absorption feature thus has to be of this order. In combination with values of the column density of the order of 7×10^{21} cm^{-2} for the foreground gas derived above (and being a lower limit), the absorbing layer has thus to have, as a minimum, a density around 1.3×10^4 cm^{-3} for M17 SW and 2.9×10^4 cm^{-3} for Mon R2. Therefore, the origin of the gas is still unknown and the observation of additional tracers, such as [OI] would be required to disentangle the origin of the gas.
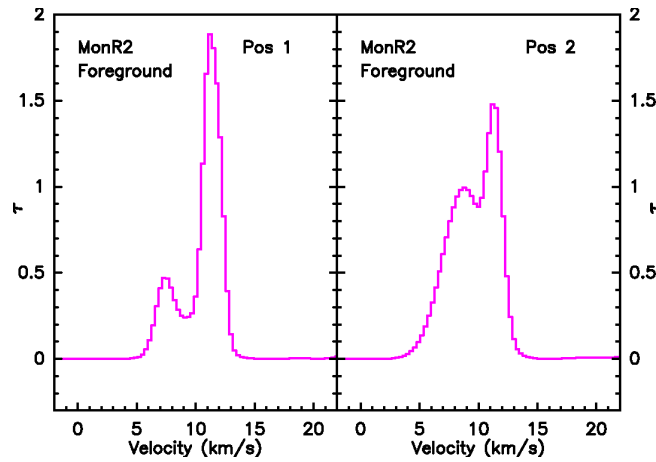
Figure 5.30: Mon R2 line profile for the optical depth for the foreground component derived from the multi-component dual layer model in pink.
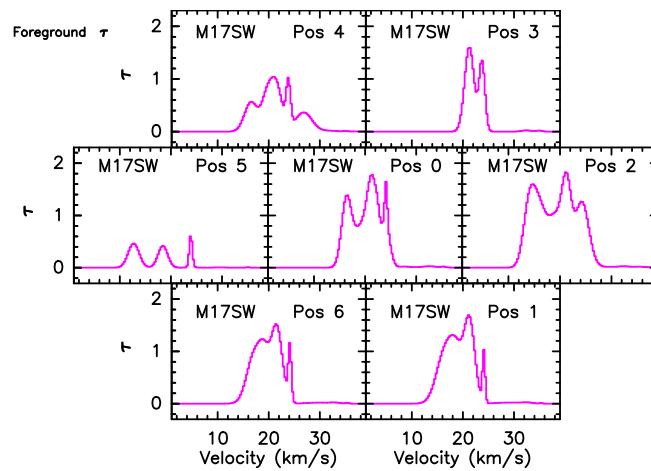
Figure 5.31: Same as Fig. 5.30 but for M17 SW.

6 | M17 [CI] $^3P_1$-$^3P_0$ Observations

This chapter shows the results of these observations towards the M17 complex, the velocity structure of the region and the column density and equivalent visual extinction for the [CI] $^3P_1$-$^3P_0$ atomic fine structure line. Finally, both regions are separated for the discussion of their particular characteristics in detail.

6.1 The M17 Complex

The [CI] $^3P_1$-$^3P_0$ atomic fine structure line observations towards the massive M17 complex covered an area of approximately 680 x 1360 arcsec^2, as shown in Fig. 6.1. The cloud is separated into two regions, M17 North (M17 N) in the northern area and M17 South West (M17 SW) in the southwestern area. M17 SW is located next to the young cluster of OB stars and gathers the largest amount of gas. Both regions have been studied as separated entities in the millimetric and submillimetric regimes, probably due to the small size of the maps available in the past. The small size of the maps can be attributed to the observing capabilities of past heterodyne receivers, with lower mapping speed due to single pixel receivers and higher noise for their observations. Now, that there is a large scale map of the region, it can be seen that both regions are connected and they are part of a larger gas complex. Appendix D shows integrated intensity maps by velocity bins of 1 km/s.

6.2 Momenta Maps and Velocity Structure of M17

The first and second momenta maps were created for the M17 complex from the [CI] $^3P_1$-$^3P_0$ emission. The first momenta map shows the velocity peak of the [CI] line (Fig. 6.2) for an intensity above 3 K. The objective was to use the first momenta map as a velocity bin identifier, allowing the identification of velocity structures of interest. In general, the average velocity peak was around 21 km/s, specially for M17 SW. North of M17 SW, the velocity peaks of the [CI] spectra decreased to
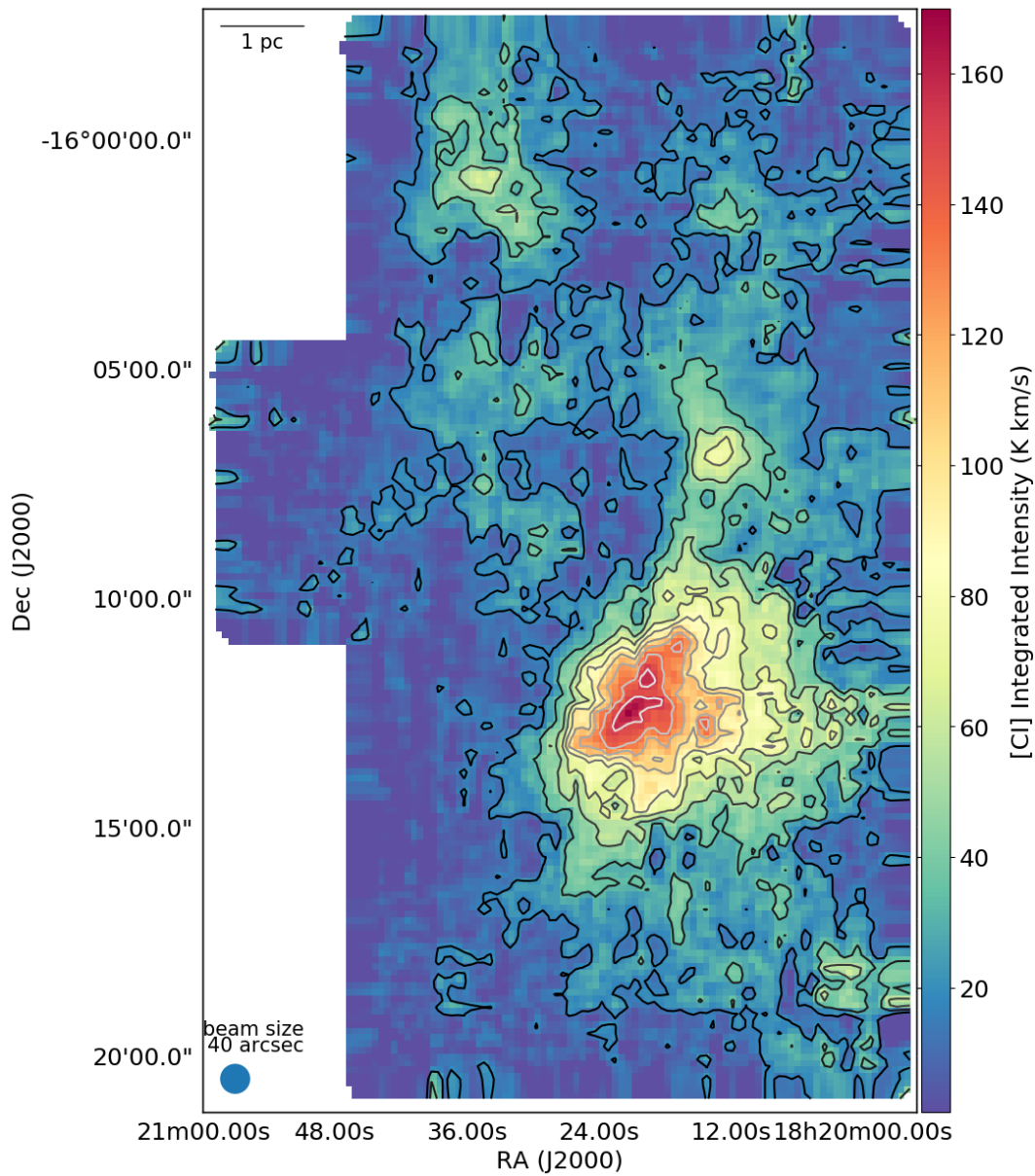
Figure 6.1: M17 [CI] $^3P_1$-$^3P_0$ integrated intensity map between 10 and 30 km/s. The contour levels increase in steps of 10% with respect to the peak integrated intensity value of 170 K km/s.
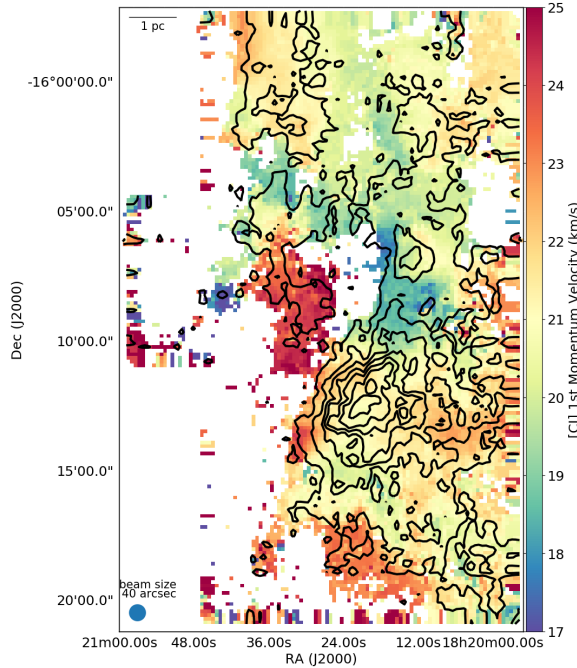
Figure 6.2: M17 [CI] first momentum (velocity) map in colors and [CI] integrated intensity in contours. The momentum map has been calculated for temperatures over 3 K.

18 km/s. Also, an individual cloud was visible with a velocity peak of 24 km/s, Northeast of M17 SW. Therefore, three characteristic velocity bins were identified, at 18, 21 and 24 km/s.

The second momenta map shows the characteristic width of the [CI] $^3P_1$-$^3P_0$ line emission for the whole map. As expected, M17 SW presented broader lines, between 4 and 6 km/s meanwhile M17 N had a much narrower line emission. The velocity width were within what is expected for a PDR.

From the three velocities identified above, the [CI] emission was separated into three distinctive velocity structures. At lower velocities, between 17 and 19 km/s with a central velocity of 18 km/s (Fig. 6.4), the complex showed an elongated, edge-on and narrow structure along M17 SW and part of M17 N, plus some individual clouds to the East. At central velocities, between 20 and 22 km/s with a central velocity of 21 km/s (Fig. 6.5, the main peak velocity of the [CI] emission was located, where the main intensity is concentrated. M17 SW showed a more rounded profile at the core, with extended emission from M17 SW to M17 N. Finally, at higher velocities, between 23 and 25 km/s with a central velocity of 24 km/s (Fig. 6.6), the cloud presented an elongated horizontal shape for M17 SW and additional emission in the northern part.
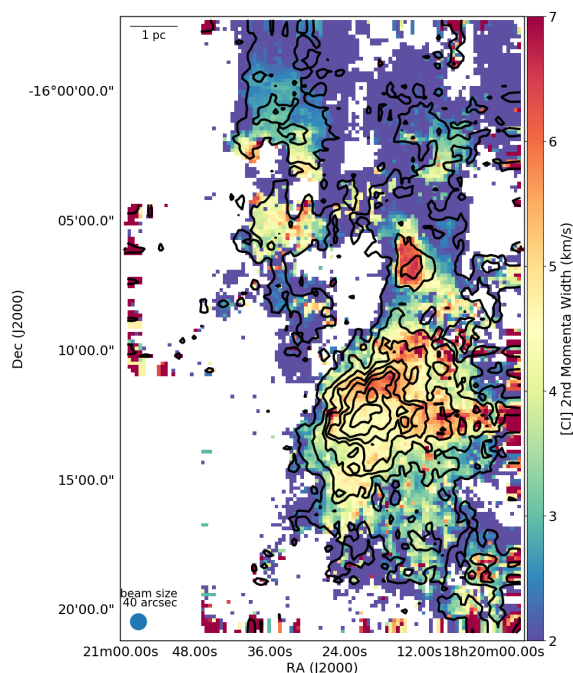
Figure 6.3: M17 [CI] second momentum (width) map in colors and [CI] integrated intensity in contours. The momentum map has been calculated for temperatures over 3 K.

M17 has been considered as a blister HII region, with the ionization front carving out into the molecular cloud (eg. Meixner et al. 1992; Pellegrini et al. 2007). Pérez-Beaupuits et al. (2015b) compared a large set of atomic and molecular data in M17 SW and the correlation between them to disentangle the ionized, atomic and molecular components along the velocity. They have found that the the ionized HII gas is located at velocities below 20 km/s and above 24 km/s, meanwhile the atomic neutral HI is located in a velocity range between 5 and 17 km/s with some emission between 23 and 30 km/s, and the molecular H_2 gas can be found along the whole velocity range, between 0 and 40 km/s, with a peak at 20-21 km/s. This velocity distribution can provide some insight for the interpretation of the different structures for the whole M17 in [CI] $^3P_1$-$^3P_0$. The lower velocity [CI] structure can be associated with the HI emission alongside the PDR, showing its characteristic edge-on structure. The velocity structure at 21 km/s can be associated closer to the molecular component, explaining its rounded shape, deeper into the cloud. Finally, the cloud at 24 km/s has been previously identified as a local foreground cloud detected in CO that obscures the M17 complex (Meixner et al. 1992). This fact accounts for its independent structure, with respect to the other two distributions.
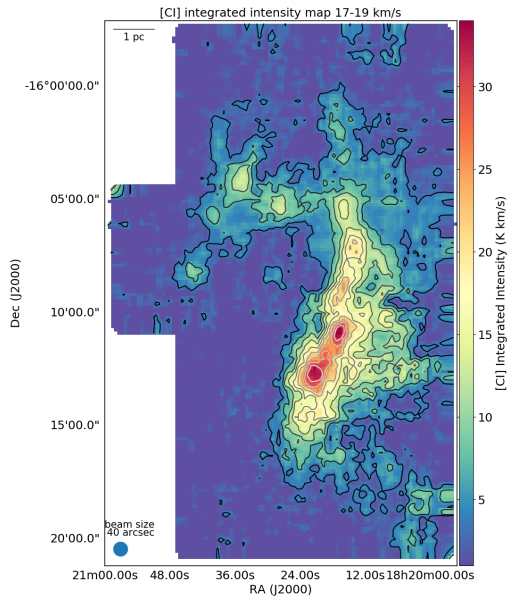
Figure 6.4: [CI] $^3P_1$-$^3P_0$ integrated intensity map between 17 and 19 km/s.
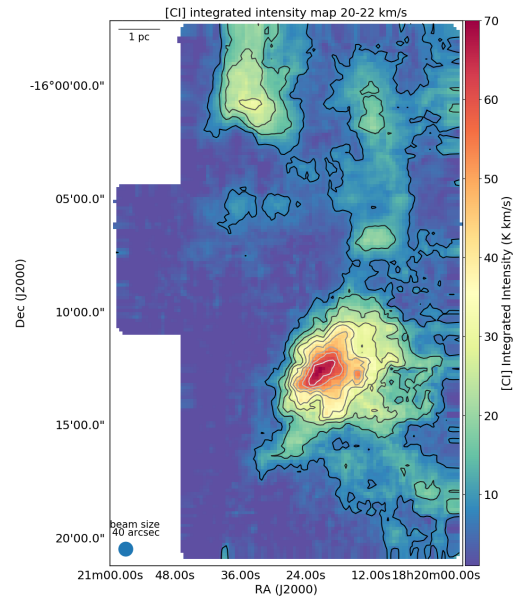
Figure 6.5: [CI] $^3P_1$-$^3P_0$ integrated intensity map between 20 and 22 km/s.
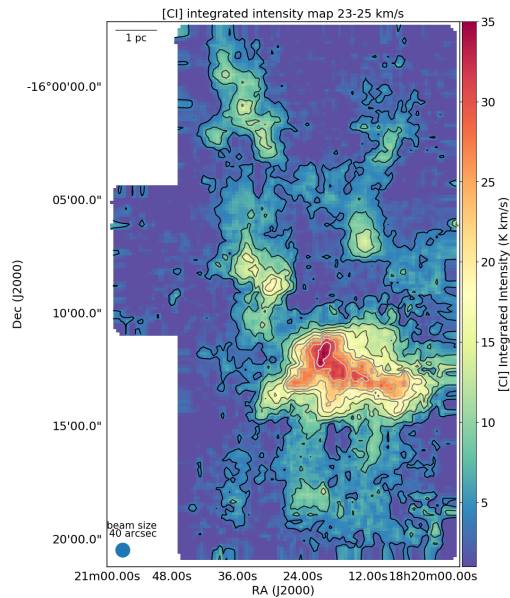
Figure 6.6: [CI] $^3P_1$-$^3P_0$ integrated intensity map between 23 and 25 km/s.

6.3   Column Density Maps

The atomic carbon column density was estimated from the [CI] $^3P_1$-$^3P_0$ emission using Eq. 2.57. Hence, a carbon column density map was generated, as shown in Fig. 6.7. Pérez-Beaupuits et al. (2015b) derived the excitation temperature of [CI] for M17 SW from the ratio of both [CI] atomic line transitions, with an excitation temperatures that ranged between 40 and 100 K for the molecular region, that was in concordance with previous analysis (Genzel et al. 1988; Pérez-Beaupuits et al. 2010). The early analysis indicated that the [CI] gas arises from the interclump medium with a kinetic temperature of 50 K and $n(H_2) \sim 3$ x 10^3 cm^{-3}). Therefore, a kinetic temperature of 50 K was assumed for the whole complex, as a first approximation to the column density derivation. For a more precise derivation, the [CI] $^3P_2$-$^3P_1$ atomic transition line would be needed.

As expected, the largest column densities were located in M17 SW, with an average of 1.03×10^{18} cm-2 for the whole region. M17 N had an average column density almost 5 times lower, with an average value of 2.67×10^{17} cm-2. The average values for both regions, as well as selected positions in them, can be seen below in Table 6.1.

It has also been estimated the column density of the hydrogen, derived from the [CI] $^3P_1$-$^3P_0$ atomic line emission as shown in Fig. 6.7. A H/C ratio of 1.2×10^{-4} (Wakelam & Herbst 2008) has been used, assuming that all the carbon is in atomic neutral form. Therefore, the column density derived was a lower limit and results could be higher. From there, the peak hydrogen column density corresponded to 1.87×10^{22} cm^{-2}.

Then, knowing the hydrogen column density, the equivalent visual extinction traced by the [CI] $^3P_1$-$^3P_0$ atomic line emission was estimated. The canonical value of 1.87×10^{21} cm$^{-2}/A_v$ has been used (Reina & Tarenghi 1973; Bohlin et al. 1978; Diplas & Savage 1994; Predehl & Schmitt 1995). The visual extinction map is shown in Fig. 6.7. The peak visual extinction was located in M17 SW with a value of 10 magnitudes. The region also had an average visual extinction of 4.6 magnitudes. M17 N, on the contrary, presented much lower values, with an average visual extinction of 1.2 magnitudes.
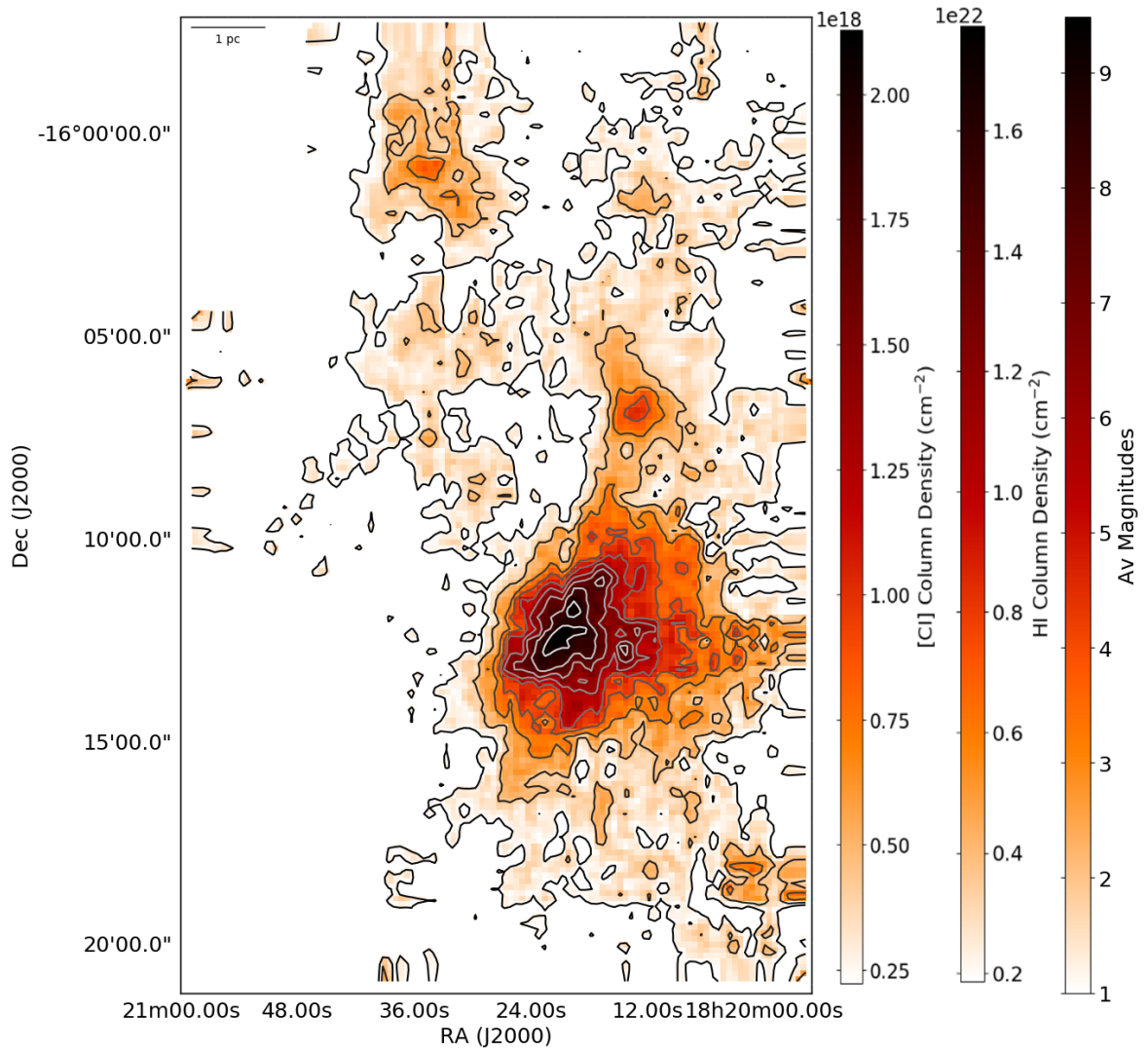
Figure 6.7: M17 composite map formed by the [CI] column density map, hydrogen column density map derived from the carbon emission and equivalent visual extinction map. The contour levels increase in steps of 10% with respect to the peak.

Table 6.1: Observational parameters for the sources.

Positions	Relative Coordinates[a] (ra,dec)	Integrated Intensity (K km/s)	[CI] Column Density (cm^{-2})	H Column Density[b] (cm^{-2})	Av[c] (mag.)
M17SW (1)	-100″,-25″	161.1	2.11×10^{18}	1.76×10^{22}	9.4
M17SW (2)	-120″,15″	153.4	2.01×10^{18}	1.68×10^{22}	9.0
M17SW (3)	-160″,55″	130.0	1.70×10^{18}	1.42×10^{22}	7.6
M17SW (4)	-200″,-45″	117.2	1.54×10^{18}	1.28×10^{22}	6.8
M17SW (5)	-60″,0″	105.1	1.38×10^{18}	1.15×10^{22}	6.1
<M17SW>		79.0	1.03×10^{18}	8.6×10^{21}	4.6
M17N (6)	-220″,305″	77.6	1.02×10^{18}	8.48×10^{21}	4.5
M17N (7)	110″,670″	54.6	7.16×10^{17}	5.97×10^{21}	3.2
<M17N>		20.4	2.67×10^{17}	2.22×10^{21}	1.2

[a] Relative coordinates from reference position ra: 18 h 20 m 27.60 s & dec: -16° 12′ 00.9″.
[b] H/C = 1.2×10^{-4}.
[c] Av = HI/1.87×10^{21} magnitudes.

6.4   M17 Regions

Traditionally, both regions has been separated for analysis, and this is the approach followed here, for taking into account their individual characteristics. Points of interest and local peaks has been labeled with consecutive Arabic numbers. The peak integrated intensity emission for the whole map, located in M17 SW (see Fig. 6.8 below) was labeled as 1, meanwhile the local M17 SW peaks were labeled as 2, 3 and 4 respectively. Also, it was labeled as position 5, the selected M17 SW position in which the [CI] $^3P_1$-$^3P_0$ spectrum and equivalent visual extinctions were compared with complementary tracers. In M17 N, the local peaks were labeled as positions 6 and 7 respectively (see Fig. 6.12 below). Table 6.1 summarizes the [CI] integrated intensities, [CI] column densities, H column densities and equivalent visual extinction of the recently listed selected positions, as well as the average values for each region.

6.4.1   M17 Southwest

M17 SW, as said above, presents an edge-on geometry with clumpy gas, as can be seen in Fig. 6.8. The OB stars cluster is situated to the East, with the ionization front coming from this direction. It has the largest [CI] $^3P_1$-$^3P_0$ column density with a peak value of 2.11×10^{18} cm^{-2} (Table 6.1). Its structure is basically a large core of material with larger density, with a sharp profile to the East, and a more extended tail to the West, product of the ionization front probably.
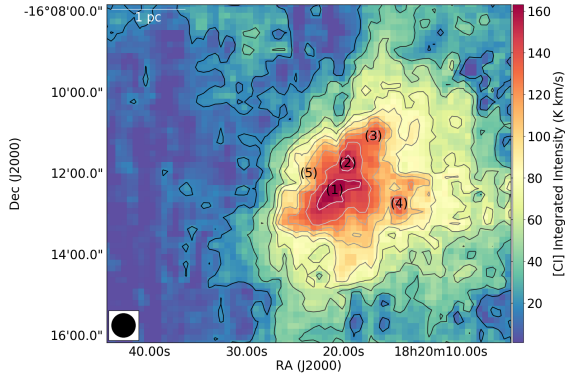
Figure 6.8: M17 SW [CI] $^3P_1$-$^3P_0$ integrated intensity map between 10 and 30 km/s.
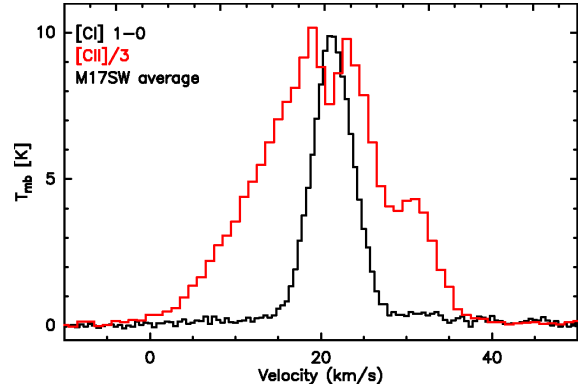
Figure 6.9: M17 SW average [CI] $^3P_1$-$^3P_0$ spectrum in black and [CII] average spectrum scaled down in red.

The average spectrum for the whole region is shown in Fig. 6.9. The average M17 SW [CI] emission presented only one Gaussian component, with a velocity range from 12 to 28 km/s and a velocity peak at 21 km/s. Also, the [CI] average spectrum was compared with the [CII] 158 μm average spectrum for M17 SW, from Pérez-Beaupuits et al. (2012). [CII] showed a double peak profile, with the [CI] peak intensity located between the two peaks, but as it will be discussed in Chapter 5, [CII] is affected by self-absorption effects with absorption dips that mimic velocity components, hence the comparison of the velocity profiles should be take with caution. Fig. 6.10 shows a comparison of the integrated intensity line maps for both lines. [CI] $^3P_1$-$^3P_0$ is plotted in contours for a velocity range between 10 and 30 km/s, and [CII] 158 μm is plotted in color scale for a velocity range between 0 and 50 km/s. It can be seen that there is stratification, even in the clumpy environment of M17 SW. [CII] emission peaked closer to the East of the OB cluster, compared to the [CI] peak.

As it was said above, a comparison has also been made for position 5. The [CI] $^3P_1$-$^3P_0$ spectrum was compared with complementary data of different tracers covering a wide range of conditions, from ionized to molecular emission. The available tracers were [^{12}CII] and [^{13}CII] atomic line emission, and ^{13}CO (3-2) and C^{18}O (1-0) rotational molecular emission. The comparison of the spectra is shown in Fig. 6.11. The complementary data is analyzed in Chapter 5, where it is offered a study of the [CII] optical depth and the physical conditions of the gas using the [^{13}CII] isotopic line. The equivalent visual extinction traced by [CI] for this position corresponded to 6.1 magnitudes, but for [CII], it corresponded to 41 magnitudes (see Section 5.3) and 75.6 magnitudes for the C^{18}O (1-0) molecular line (Section 5.6). There is a large
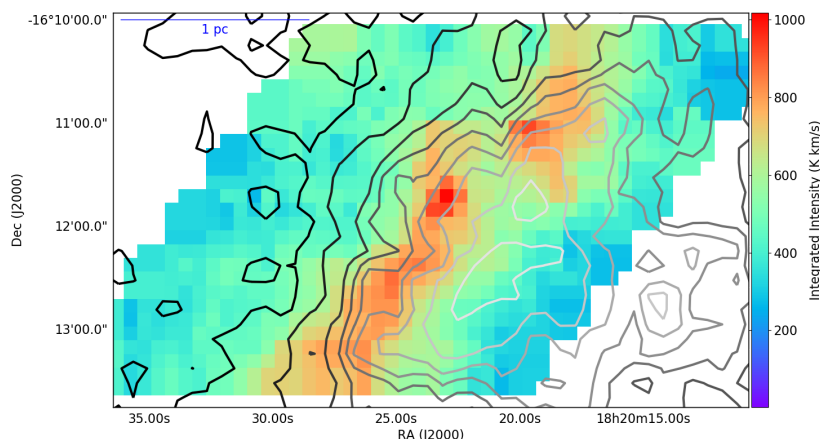
Figure 6.10: M17 SW [CII] integrated intensity map between 0 and 50 km/s from Pérez-Beaupuits et al. (2012). In contours [CI] $^3P_1$-$^3P_0$ integrated intensity between 10 and 30 km/s.

discrepancy between [CI] and the other tracers, situation discussed below in the next section.

Then, the position 5 [CI] $^3P_1$-$^3P_0$ line profile peaked at 21 km/s and was shifted to the red part of the spectrum compared to the other lines. First of all, the [CI] line was compared with the ionized emission, and it can be seen that the [CI] spectrum is much narrower than [^{12}CII] and, in particular, to the optically thin [^{13}CII] line. The [^{13}CII] completely enveloped the [CI] emission, and their wings between 22 and 28 km/s matched. This suggested us that both species coexists at different velocities in the clumpy medium of M17. Also, for the foreground cloud at 24 km/s detected in CO named above, [CII] and [CI] are well mixed with each other.

The situation was different with the molecular components. Their velocity peaks were displaced with respect to each other and their profiles were also different. Both molecular lines showed a symmetric profile with respect to the velocity peak; on the other hand, the [CI] profile was asymmetric, with a long wing towards lower velocities, between 17 and 20 km/s. At these lower velocities, the molecular emission wings and the [CI] line emission matched well, where the hydrogen atomic gas is predominant. This match suggested that only in the atomic part of the cloud both species behave in a similar way, but closer to the molecular layer at 20 km/s, it is
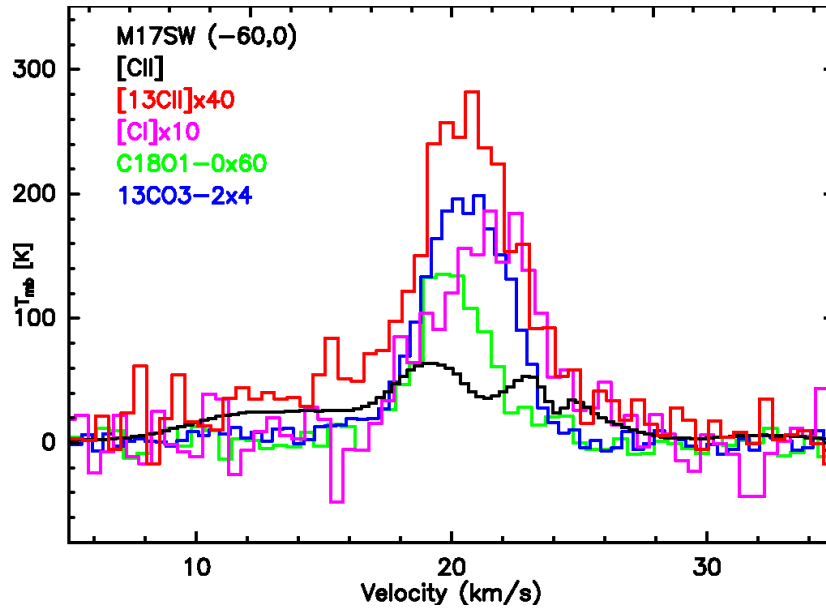
Figure 6.11: M17 SW comparison between [CI] $^3P_1$-$^3P_0$ and [CII], ^{13}CO (3-2) and C^{18}O (1-0) from Chapter 5.

not the case. It has been suggested that [CI] could work as a good tracer for column density for molecular clouds (eg. Glover et al. 2015; Clark et al. 2019), but as it can be seen here from the line profiles, M17SW does not behave in this way. The profiles are completely different at the molecular velocities and only match in the atomic side of the spectrum. This discrepancy could be explained due to the massiveness and clumpiness of M17, with cold molecular clumps surrounded by warmer atomic gas in different layers.

6.4.2 M17 North

M17 N is ionized by the OB cluster located to the South of it, but from a larger distance than M17 SW, as can be seen in Fig. 6.12. It presented two local [CI] $^3P_1$-$^3P_0$ column density peaks, with a column density of 1.02×10^{18} and 7.16×10^{17} cm^{-2} respectively, or 4.5 and 3.2 magnitudes in equivalent extinction (Table 6.1). The region was less dense than M17 SW and its morphology presented a much more extended emission along the map with respect to M17 SW. The average spectrum for the whole region is shown in Fig. 6.13. The emission was less intense than M17 SW, with the main emission showing a single Gaussian component with a velocity between 15 and 25 km/s. There was additional components visible in the spectra, in emission around 40 km/s and in absorption at 60 km/s. The emission in absorption is due to contamination in the OFF position. These components has also been identified from ^{12}CO 1-0 and ^{13}CO 1-0 observations of the whole M17 complex observed with the Nobeyama 45m telescope (Nguyen Luong, in prep.) as emission associated
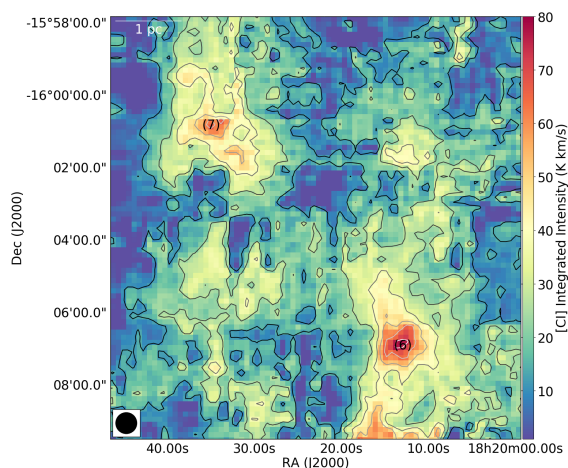
Figure 6.12: M17 N [CI] $^3P_1$-$^3P_0$ integrated intensity map between 10 and 30 km/s.
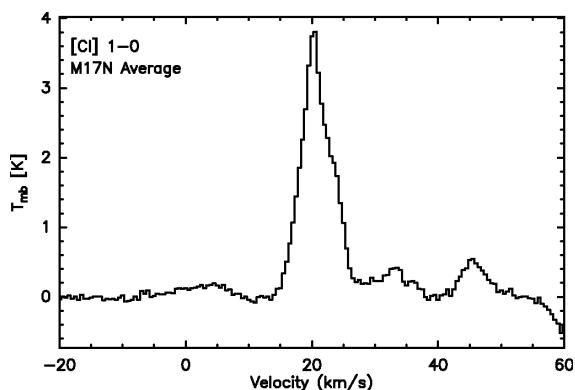
Figure 6.13: M17 N average [CI] $^3P_1$-$^3P_0$ spectrum.

with the Scutum and Norma arms respectively.

6.5 Carbon Column Density Deficit

There is a large discrepancy in the equivalent visual extinction estimated for the [CI], compared to [CII] and $C^{18}O$ 1-0, in almost one order of magnitude of difference, with the [CI] tracing much less emission than the others. This situation could be explained probably due to the lower abundance of carbon, compared to the other traces. From Röllig & Ossenkopf (2013) for example, Fig. 6.14 shows a model of the chemical abundance for the different tracers in ionized, neutral and molecular form.

In the outer parts of the PDR, photoionization is the dominant process, turning almost all carbon into ionized one, with some carbon remaining in neutral form through recombinations with electrons. Here, neutral carbon abundance is almost one order of magnitude lower than the ionized carbon one. Then, when the FUV field attenuates and the dust increases, recombination dominates over photoionization and carbon is distributed along many species, including neutral carbon. But at $A_V \gtrsim$ of 1 mag., the majority of carbon becomes carbon monoxide. Hence, carbon becomes just a transitional species between C^+ and CO, with a much lower abundance ratio than C^+ or CO. In the estimations of the carbon column density, it was assumed that all carbon is in neutral form. This order of magnitude of difference could account for part of the visual extinction missing by the tracer. Additionally, neutral carbon is really sensitive to changes in the physics and chemistry of the gas,
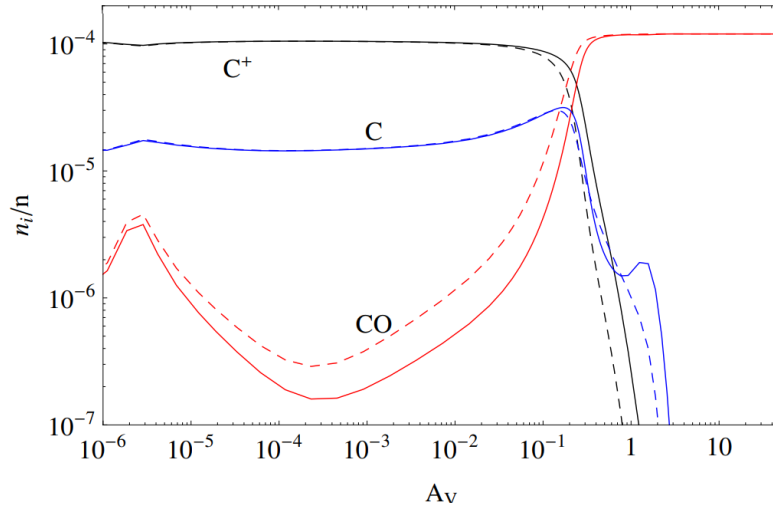
Figure 6.14: Chemical abundance of a modeled clump for a density of 10^5 cm^{-3}, a mass of 100 M$_o$ and $\chi = 10$, from Röllig & Ossenkopf (2013).

unlike C$^+$ and CO, and M17 with its clumpyness an high density has particular characteristics that makes it different from the standard PDR.

A precise estimation of the local abundance of carbon for the local physical conditions of M17 would require a direct comparison of the different tracers using PDR models, to derive the physical properties of the gas and its chemical abundance along the cloud. Due to the clumpiness of M17, a model such as the KOSMA TAU model would be an excellent tool for analysis. But, this would require large scale maps of the whole M17 complex, to analyze the different regions and their physical conditions in detail. Just recently, there have been released observations of CO 1-0 and ^{13}CO 1-0 from the Nobeyama 45m telescope of the whole M17 complex, giving access to molecular data. Also, is planned a large public survey of PDRs using the SOFIA/upGREAT receiver to observe large scale maps of the [CII] fine structure line, and one of the sources in this survey is the M17 complex. For this reason, the modeling of the M17 complex will remain as a future project, when both maps will be available.

7 | Summary

In this thesis, two large datasets of fine structure atomic lines have been presented: First, [^{12}CII] fine structure line and [^{13}CII] hyperfine structure line observations with the SOFIA/upGREAT array receiver at signal to noise and high spectral resolution towards four selected PDRs covering a wide range of physical conditions, namely M43, the Horsehead PDR, Monoceros R2 and M17 SW. The [CII] observations are key to unravel the question about the optical depth of the [CII] line through the observations of the optically thin [^{13}CII] isotope. And second, large scale observations of the [CI] ^{3}P$_1$-^{3}P$_0$ fine structure line transition with the NANTEN2/SMART heterodyne array receiver at high spectral and spatial resolution towards the M17 complex tracing the neutral atomic gas in the PDR. These observations are an important test case and a pathfinder for the new generation of radio telescopes and multipixel heterodyne receivers.

7.1 [^{12}CII] and [^{13}CII] Observations

The [^{12}CII] and [^{13}CII] observations and analyses confirmed the long standing suspicion (Russell et al. 1980; Langer et al. 2016), already proven for the single case of Orion-B (Graf et al. 2012) that [^{12}CII] emission is heavily affected by high optical depth and self-absorption effects. The observed [^{13}CII] emission, if scaled up by the abundance ratio of ^{12}C/^{13}C (α^+) in all cases overshot the observed [^{12}CII] intensities, giving a first indication that the [^{12}CII] emission has an optical depth above unity. Moreover, the line profiles of the optically thin [^{13}CII] emission for Mon R2 and M17 SW were completely different than their complex counterparts in [^{12}CII]. This showed clear indications of self-absorption effects at the line centers or an otherwise non-homogeneous source structure.

A zeroth order analysis, assuming a homogeneous single layer source, gave an [^{12}CII] optical depth of about 2 for M43 and the Horsehead PDR; for the other two sources, Mon R2 and M17 SW, the thus derived optical depths were much higher,

around 5 to 7. It was possible to derive a minimum [^{13}CII] column density from the integrated intensity line for the case of high excitation temperature limit of the C$^+$ fine structure levels. Assuming a T_{ex} large enough that tends to infinity, the thus derived value was a lower limit, rapidly increasing for temperatures lower than 100 K. And from there, the [^{12}CII] column density was derived scaling-up the [^{13}CII] column density with the abundance ratio α^+. Additionally, an estimation of the [^{12}CII] column density was done directly from the [^{12}CII] integrated intensity line, ignoring the knowledge given by the observed [^{13}CII] emission and following the standard approach of assuming that the [^{12}CII] emission is optically thin. The directly derived [^{12}CII] minimum column density systematically underestimated the C$^+$ column density, by a factor as high as 4.

The complexity of the sources, the high optical depth and the large discrepancy between the C$^+$ column densities derived directly from [^{12}CII] and [^{13}CII] gave rise to the need of a more sophisticated approach than the simple single layer assumption. For these reasons, a multi-component Gaussian source model with two layers has been developed, with an emitting background layer and an absorbing foreground one, in particular for Mon R2 and M17 SW. When fitting the [^{13}CII] and [^{12}CII] emission simultaneously in a multi-component source model, the emission of the first two sources (M43 and the Horsehead PDR) could be fitted by emission components only, allowing also to determine the excitation temperature. The resulting T_{ex} turned out to be around 100 K, thus obtaining a higher column density than the ones derived from the [^{13}CII] integrated intensity using an extremely high T_{ex}.

For the other two sources, the complex line profiles with the apparent self absorption notches visible in [^{12}CII] required to include a low temperature absorbing foreground layer. These dual layer, multi-component fits could reproduce the combined [^{13}CII] and [^{12}CII] profiles. Due to the high number of free parameters, it was required to assume a fixed value for T_{ex}, both for the background and the foreground layer. For the background components, typical values for the C$^+$ layer in PDRs were used, from 150 to 250 K; for the foreground, the brightness temperatures in the center of the absorption notches gave an upper limit to the T_{ex} between 20 and 40 K. In these fits, the [^{12}CII] optical depth of the individual components was much lower than the one derived in the zeroth order analysis, covering a range up to 2. This was plausible because the unjustified assumption of a constant, uniform T_{ex} for the whole spectrum in the zeroth order analysis (clearly not applicable with the complex line profiles) was now released. The total C$^+$ column densities derived for the sources that present absorption dips were slightly larger in the multi-component analysis, compared to the ones derived from the [^{13}CII] integrated intensity. The

bulk of the column density was, of course, constrained by the [^{13}CII] emission, but the multi-component source models now added additional components, which were not visible in [^{13}CII], as their optical depth or excitation temperature were too low for being visible above the noise level. This included the additional emission components and the foreground absorption components. The latter typically contributed 10 to 50% of the total column density. The multi-component analysis has established a scenario with two layers. A background layer where broad components with high temperature and extremely high column density produce emission over a wide range of LSR-velocities. And a foreground layer composed by low temperature and high column density narrow components of ionized gas that absorb the background at velocities closer to the [^{13}CII] peak.

Formally, a second scenario for the source model, namely a single layer, pure emission model, could also reproduce the observed [^{13}CII] and [^{12}CII] emission. Here, the [^{13}CII] emission component was represented on the [^{12}CII] side by an extremely high optical depth (and column density) component, that had a relatively low T_{ex}. This resulted in a broad, flat topped [^{12}CII] emission. The complex line profiles in Mon R2 and M17 SW then required a set of additional narrow line and higher temperature emission components that were not visible in [^{13}CII] due to their lower column density. This model was ruled out as being physically unlikely, because the extremely large column of low-temperature C$^+$ emission was physically implausible and, in addition, the comparison with the low-J CO isotopologues line profiles showed that the individual components traced in [CII] and CO isotopologues do not match.

The value of the isotopic abundance ratio α^+ is, of course, an important parameter. A lower ratio would imply a lower [^{12}CII]/[^{13}CII] intensity ratio in the optically thin limit, and correspondingly lower optical depths derived in the zeroth order analysis and vice versa for a higher value. Although the S/N was not sufficient in the individual spectra of the present observations, it has been shown that for the average spectrum of M17 SW, the S/N was high enough that it was possible to derive a value higher than the one assumed before. Although, a consistent value in the wings was not reached, showing still large variations between different bins. This may indicate fractionation effects for the ionic and the molecular isotopic species. Observations with higher sensitivity both for the ionized fine structure lines and the molecular lines, a well as direct derivation of the abundance ratio through the observation of isotopologues that contain carbon or through modeling, may resolve this issue in the future.

The [^{12}CII] and [^{13}CII] analysis presented here showed that the origin of [CII] emission is somewhat more complex than simple model scenarios suggest. The complex line profiles and high optical depth visible in particular in the bright sources of strong [CII] emission in the Milky Way revealed substantially higher [CII] column densities than the ones estimated in the optically thin approximation from integrated line profiles. The self-absorption implied significant column densities of C^+ at low temperatures of, at present, unknown origin. Therefore, line integrated intensities and line integrated intensity ratios, derived from velocity unresolved spectra ignoring these effects, often used to derive the physical parameters of the source in comparison with, for instance a standard PDR scenario, have to be regarded with caution, in particular for external galaxies. Interesting issues to solve will be how empirical correlations between the [CII] integrated line intensity and bulk parameters like star formation rate are affected by this more complex origin of the [CII] emission; and to study if the other cooling [OI] lines are affected also by self-absorption effects.

7.2   [CI] ^{3}P$_1$-^{3}P$_0$ Observations

The first momenta map have shown three distinctive velocity structures for the M17 complex in CI] ^{3}P$_1$-^{3}P$_0$. The first velocity bin centered at 18 km/s showed an elongated edge-on structure with a direction from north to south between M17 SW and M17 N that correlated with the neutral atomic emission of the HI gas. The second velocity bin centered at 21 km/s showed a rounded core for M17 SW that extended towards the north and correlated with the molecular gas. The third velocity bin centered at 24 km/s showed an elongated east to west ridge for M17 SW that spread towards M17 N and it has been identified as a foreground cloud associated to the M17 complex. The peak [CI] column density was found in M17 SW, with a value of 2.11×10^{18} cm^{-2}, whereas the average column density for M17 SW was 1.03×10^{18} cm^{-2} and for M17 N 2.67×10^{17} cm^{-2}, 5 times lower than in M17 SW. The equivalent visual extinction was 9.4, 4.6 and 1.2, respectively.

M17 SW showed some stratification between [CI] and [CII], found from the comparison between the integrated intensity map of both of them. The [CI] main peak and emission ridge was located further West of the [CII] one. The average spectra peaked at 21 km/s and showed a symmetric profile. One position was available for comparison with complementary data in [^{12}CII], [^{13}CII], C^{18}O 1-0 and ^{13}CO 4-3. The [CI] peak was shifted to the red part of the spectrum compared to the rest of the species. The optically thin [^{13}CII] completely embraced the narrower [CI] spectrum and matched towards the wings, showing that both species are well mixed. The

situation was different for the molecular tracers, their line profiles were different, with the [CI] showing an asymmetric profile with a longer wing towards the lower velocities that matched with the molecular tracers and where the neutral atomic HI is located.

M17 N had a much lower column density and equivalent visual extinction compared to M17 SW. The average spectrum showed an asymmetric line profile with additional emission at 22 km/s, where the foreground cloud is located. Also, there were additional components at high velocities outside the velocity range of M17. These contributions have been identified as emission from the Scutum and Norma arms.

In general, the [CI] column density was much lower compared to the other species, namely [CII] and CO. This phenomenon can be partially explained due to the lower abundance of neutral carbon in PDRs, with C^+ and CO the dominant species in the outer and inner layers of PDRs, respectively. Also, for the estimation of the hydrogen column density, all carbon was assumed as being in atomic neutral form, lowering the ratio between hydrogen and carbon; and consequently, the estimation of the hydrogen column density and equivalent extinction. An estimation of the real abundance of carbon for the local conditions of M17 would require the modeling of the PDR through numerical simulations and the derivation of the physical properties. This would need a large set of different tracers for the whole M17 complex, situation that is not available at the moment but it will be in the near future thanks to future projects and telescopes.

Bibliography

Abergel, A., Teyssier, D., Bernard, J. P., et al. 2003, A&A, 410, 577

Abrahamsson, E., Krems, R. V., & Dalgarno, A. 2007, ApJ, 654, 1171

Abt, H. A., Wang, R., & Cardona, O. 1991, ApJ, 367, 155

André, P., Men'shchikov, A., Bontemps, S., et al. 2010, A&A, 518, L102

Bally, J., Chambers, E., Guzman, V., et al. 2018, AJ, 155, 80

Barinovs, Ğ., van Hemert, M. C., Krems, R., & Dalgarno, A. 2005, ApJ, 620, 537

Becklin, E. E. & Gehrz, R. D. 2009, in Astronomical Society of the Pacific Conference Series, Vol. 417, Submillimeter Astrophysics and Technology: a Symposium Honoring Thomas G. Phillips, ed. D. C. Lis, J. E. Vaillancourt, P. F. Goldsmith, T. A. Bell, N. Z. Scoville, & J. Zmuidzinas, 101

Beetz, M., Elsaesser, H., Weinberger, R., & Poulakos, C. 1976, A&A, 50, 41

Berné, O., Fuente, A., Goicoechea, J. R., et al. 2009, ApJl, 706, L160

Betz, A. & Zmuidzinas, J. S. 1984, in Airborne Astronomy Symposium, ed. H. A. Thronson, Jr. & E. F. Erickson

Beuther, H., Bihr, S., Rugel, M., et al. 2016, A&A, 595, A32

Blum, R. D. & Pradhan, A. K. 1991, Physical Review A, 44, 6123

Bohlin, R. C., Savage, B. D., & Drake, J. F. 1978, ApJ, 224, 132

Boreiko, R. T., Betz, A. L., & Zmuidzinas, J. 1988, ApJl, 325, L47

Boselli, A., Gavazzi, G., Lequeux, J., & Pierini, D. 2002, A&A, 385, 454

Brogan, C. L. & Troland, T. H. 2001, ApJ, 560, 821

Brogan, C. L., Troland, T. H., Roberts, D. A., & Crutcher, R. M. 1999, ApJ, 515, 304

Broos, P. S., Feigelson, E. D., Townsley, L. K., et al. 2007, ApJS, 169, 353

Brown, J. M., Varberg, T. D., Evenson, K. M., & Cooksy, A. L. 1994, ApJl, 428, L37

Buchel, D., Putz, P., Jacobs, K., et al. 2015, IEEE Transactions on Terahertz Science and Technology, 5, 207

Burbidge, E. M., Burbidge, G. R., Fowler, W. A., & Hoyle, F. 1957, Reviews of Modern Physics, 29, 547

Carter, M., Lazareff, B., Maier, D., et al. 2012, A&A, 538, A89

Chen, Z., Jiang, Z., Wang, Y., et al. 2012, PASJ, 64, 110

Chini, R., Nielbock, M., & Beck, R. 2000, A&A, 357, L33

Choi, M., Evans, II, N. J., Tafalla, M., & Bachiller, R. 2000, ApJ, 538, 738

Clark, P. C., Glover, S. C. O., Ragan, S. E., & Duarte-Cabral, A. 2019, MNRAS, 486, 4622

Colbert, J. W., Malkan, M. A., Clegg, P. E., et al. 1999, ApJ, 511, 721

Contursi, A., Poglitsch, A., Grácia Carpio, J., et al. 2013, A&A, 549, A118

Cooksy, A. L., Blake, G. A., & Saykally, R. J. 1986, ApJl, 305, L89

Cormier, D., Madden, S. C., Lebouteiller, V., et al. 2015, A&A, 578, A53

Crawford, M. K., Genzel, R., Townes, C. H., & Watson, D. M. 1985, ApJ, 291, 755

Crawford, M. K., Lugten, J. B., Fitelson, W., Genzel, R., & Melnick, G. 1986, ApJl, 303, L57

Davies, J. I., Baes, M., Bendo, G. J., et al. 2010, A&A, 518, L48

de Graauw, T., Helmich, F. P., Phillips, T. G., et al. 2010, A&A, 518, L6

De Looze, I., Baes, M., Bendo, G. J., Cortese, L., & Fritz, J. 2011, MNRAS, 416, 2712

Diplas, A. & Savage, B. D. 1994, ApJ, 427, 274

Draine, B. T. 1978, ApJs, 36, 595

Draine, B. T. 2011, Physics of the Interstellar and Intergalactic Medium

Draine, B. T. & Bertoldi, F. 1999, in The Universe as Seen by ISO, Vol. 427, 553

Elia, D., Strafella, F., Schneider, N., et al. 2014, ApJ, 788, 3

Facchini, S., Clarke, C. J., & Bisbas, T. G. 2016, MNRAS, 457, 3593

Felli, M., Churchwell, E., & Massi, M. 1984, A&A, 136, 53

Ferland, G. J., Korista, K. T., Verner, D. A., et al. 1998, PASP, 110, 761

Flower, D. R. 1988, Journal of Physics B Atomic Molecular Physics, 21, L451

Flower, D. R. & Launay, J. M. 1977, Journal of Physics B Atomic Molecular Physics, 10, L229

Gaia Collaboration, Brown, A. G. A., Vallenari, A., et al. 2016, A&A, 595, A2

Galavis, M. E., Mendoza, C., & Zeippen, C. J. 1997, Astronomy and Astrophysics Supplement Series, 123, 159

García, P., Simon, R., Stutzki, J., et al. 2016, A&A, 588, A131

Genzel, R., Crawford, M. K., Townes, C. H., & Watson, D. M. 1985, ApJ, 297, 766

Genzel, R., Harris, A. I., Stutzki, J., & Jaffe, D. T. 1988, ApJ, 332, 1049

Genzel, R., Watson, D. M., Townes, C. H., et al. 1984, ApJ, 276, 551

Gerin, M., Phillips, T. G., Keene, J., Betz, A. L., & Boreiko, R. T. 1998, ApJ, 500, 329

Giannetti, A., Wyrowski, F., Brand, J., et al. 2014, A&A, 570, A65

Gillespie, C. M., J. 1981, in Society of Photo-Optical Instrumentation Engineers (SPIE) Conference Series, Vol. 265, Shuttle Pointing of Electro-Optical Experiments, ed. W. Jerkovsky, 1–7

Ginard, D., González-García, M., Fuente, A., et al. 2012, A&A, 543, A27

Glover, S. C. O., Clark, P. C., Micic, M., & Molina, F. 2015, MNRAS, 448, 1607

Goicoechea, J. R., Teyssier, D., Etxaluze, M., et al. 2015, ApJ, 812, 75

Goldsmith, P. F., Yıldız, U. A., Langer, W. D., & Pineda, J. L. 2015, ApJ, 814, 133

Goudis, C., ed. 1982, Astrophysics and Space Science Library, Vol. 90, The Orion complex: A case study of interstellar matter

Graf, U. U., Heyminck, S., Michael, E. A., et al. 2003, in SPIE Proceedings, Vol. 4855, Millimeter and Submillimeter Detectors for Astronomy, ed. T. G. Phillips & J. Zmuidzinas, 322–329

Graf, U. U., Simon, R., Stutzki, J., et al. 2012, A&A, 542, L16

Gratier, P., Pety, J., Guzmán, V., et al. 2013, A&A, 557, A101

Green, S. & Thaddeus, P. 1976, ApJ, 205, 766

Gregorio-Hetem, J., Montmerle, T., Casanova, S., & Feigelson, E. D. 1998, A&A, 331, 193

Guan, X., Stutzki, J., Graf, U. U., et al. 2012, A&A, 542, L4

Güsten, R., Henkel, C., & Batrla, W. 1985, A&A, 149, 195

Güsten, R., Nyman, L. Å., Schilke, P., et al. 2006, A&A, 454, L13

Güsten, R., Wiesemeyer, H., Neufeld, D., et al. 2019, Nature, 568, 357

Guzmán, V., Pety, J., Gratier, P., et al. 2012, A&A, 543, L1

Guzmán, V. V., Goicoechea, J. R., Pety, J., et al. 2013, A&A, 560, A73

Guzmán, V. V., Pety, J., Goicoechea, J. R., et al. 2015, ApJl, 800, L33

Habing, H. J. 1968, Bull. Astron. Inst. Netherlands, 19, 421

Haken, H. & Wolf, H. 2000, The Physics of Atoms and Quanta (Springer-Verlag)

Haken, H. & Wolf, H. 2004, Molecular Physics and Elements of Quantum Chemistry (Springer-Verlag)

Hanel, A. 1987, A&A, 176, 347

Harju, J., Sipilä, O., Brünken, S., et al. 2017, ApJ, 840, 63

Henkel, C., Güsten, R., & Gardner, F. F. 1985, A&A, 143, 148

Henney, W. J., Arthur, S. J., de Colle, F., & Mellema, G. 2009, MNRAS, 398, 157

Henney, W. J., Arthur, S. J., & García-Díaz, M. T. 2005, ApJ, 627, 813

Henning, T., Klein, R., Launhardt, R., Lemke, D., & Pfau, W. 1998, A&A, 332, 1035

Herbst, W. & Racine, R. 1976, AJ, 81, 840

Herrera-Camus, R., Bolatto, A. D., Wolfire, M. G., et al. 2015, ApJ, 800, 1

Heyminck, S., Graf, U. U., Güsten, R., et al. 2012, A&A, 542, L1

Heyminck, S., Kasemann, C., Güsten, R., de Lange, G., & Graf, U. U. 2006, A&A, 454, L21

Hoffmeister, V. H., Chini, R., Scheyda, C. M., et al. 2008, ApJ, 686, 310

Hollenbach, D. J. & Tielens, A. G. G. M. 1997, ARA&A, 35, 179

Hollenbach, D. J. & Tielens, A. G. G. M. 1999, Reviews of Modern Physics, 71, 173

Houck, J. R. & Ward, D. 1979, PASP, 91, 140

Hudson, C. E. & Bell, K. L. 2004, MNRAS, 348, 1275

Ibar, E., Lara-López, M. A., Herrera-Camus, R., et al. 2015, MNRAS, 449, 2498

Jensen, A. G., Rachford, B. L., & Snow, T. P. 2007, ApJ, 654, 955

Kaufman, M. J., Wolfire, M. G., & Hollenbach, D. J. 2006, ApJ, 644, 283

Kawamura, A., Mizuno, N., Yonekura, Y., et al. 2005, in IAU Symposium, Vol. 235, 275

Keenan, F. P., Lennon, D. J., Johnson, C. T., & Kingston, A. E. 1986, MNRAS, 220, 571

Khallesse, B., Pallister, W. S., Warren-Smith, R. F., & Scarrott, S. M. 1980, MNRAS, 190, 99

Klein, B., Hochgürtel, S., Krämer, I., et al. 2012, A&A, 542, L3

Klein, R., Henning, T., & Cesarsky, D. 1999, A&A, 343, L53

Kleinmann, D. E. 1973, Astrophys. Lett., 13, 49

Kong, S., Arce, H. G., Feddersen, J. R., et al. 2018, The Astrophysical Journal Supplement Series, 236, 25

Kounkel, M., Covey, K., Suárez, G., et al. 2018, AJ, 156, 84

Kramer, C. 1997, Calibrations of spectral line data at the IRAM 30m radio telescope, Version 2.1, January 24th, Tech. Rep. V. 2.1, IRAM

Kramer, C., Stutzki, J., & Winnewisser, G. 1996, A&A, 307, 915

Kutner, M. L. & Ulich, B. L. 1981, ApJ, 250, 341

Lada, C., Dickinson, D., & Penfield, H. 1974, ApJl, 189, L35

Lada, C. J., Depoy, D. L., Merrill, K. M., & Gatley, I. 1991, ApJ, 374, 533

Langer, W. D., Goldsmith, P. F., & Pineda, J. L. 2016, A&A, 590, A43

Langer, W. D., Goldsmith, P. F., Pineda, J. L., et al. 2015, A&A, 576, A1

Langer, W. D., Graedel, T. E., Frerking, M. A., & Armentrout, P. B. 1984, ApJ, 277, 581

Langer, W. D. & Penzias, A. A. 1990, ApJ, 357, 477

Langer, W. D. & Penzias, A. A. 1993, ApJ, 408, 539

Langer, W. D., Velusamy, T., Pineda, J. L., Willacy, K., & Goldsmith, P. F. 2014, A&A, 561, A122

Launay, J. M. & Roueff, E. 1977a, A&A, 56, 289

Launay, J. M. & Roueff, E. 1977b, Journal of Physics B Atomic Molecular Physics, 10, 879

Le Petit, F., Nehmé, C., Le Bourlot, J., & Roueff, E. 2006, ApJS, 164, 506

Lebouteiller, V., Péquignot, D., Cormier, D., et al. 2017, A&A, 602, A45

Lennon, D. J. & Burke, V. M. 1994, Astronomy and Astrophysics Supplement Series, 103, 273

Loren, R. B., Peters, W. L., & Vanden Bout, P. A. 1974, ApJl, 194, L103

Luhman, M. L., Satyapal, S., Fischer, J., et al. 1998, ApJl, 504, L11

Malhotra, S., Helou, G., Stacey, G., et al. 1997, ApJl, 491, L27

Mangum, J. G., Emerson, D. T., & Greisen, E. W. 2007, A&A, 474, 679

Mangum, J. G. & Shirley, Y. L. 2015, PASP, 127, 266

Meixner, M., Haas, M. R., Tielens, A. G. G. M., Erickson, E. F., & Werner, M. 1992, ApJ, 390, 499

Mendoza, C. 1983, in IAU Symposium, Vol. 103, Planetary Nebulae, ed. D. R. Flower, 143–172

Milam, S. N., Savage, C., Brewster, M. A., Ziurys, L. M., & Wyckoff, S. 2005, ApJ, 634, 1126

Mills, B. Y. & Shaver, P. A. 1968, Australian Journal of Physics, 21, 95

Monteiro, T. S. & Flower, D. R. 1987, MNRAS, 228, 101

Mookerjea, B., Israel, F., Kramer, C., et al. 2016, A&A, 586, A37

Motte, F., Zavagno, A., Bontemps, S., et al. 2010, A&A, 518, L77

Nakagawa, T., Yui, Y. Y., Doi, Y., et al. 1998, ApJS, 115, 259

Nakajima, H., Imanishi, K., Takagi, S.-I., Koyama, K., & Tsujimoto, M. 2003, PASJ, 55, 635

Nishimura, A., Minamidani, T., Umemoto, T., et al. 2018, PASJ, 70, S42

Ochsendorf, B. B., Cox, N. L. J., Krijt, S., et al. 2014, A&A, 563, A65

O'Dell, C. R. 2001, AJ, 122, 2662

O'Dell, C. R. & Harris, J. A. 2010, AJ, 140, 985

Ossenkopf, V., Röllig, M., Neufeld, D. A., et al. 2013, A&A, 550, A57

Pabst, C. H. M., Goicoechea, J. R., Teyssier, D., et al. 2017, A&A, 606, A29

Parshley, S. C., Kronshage, J., Blair, J., et al. 2018, in Society of Photo-Optical Instrumentation Engineers (SPIE) Conference Series, Vol. 10700, Ground-based and Airborne Telescopes VII, 107005X

Pellegrini, E. W., Baldwin, J. A., Brogan, C. L., et al. 2007, ApJ, 658, 1119

Penzias, A. A. 1980, Science, 208, 663

Pérez-Beaupuits, J. P., Güsten, R., Spaans, M., et al. 2015a, A&A, 583, A107

Pérez-Beaupuits, J. P., Spaans, M., Hogerheijde, M. R., et al. 2010, A&A, 510, A87

Pérez-Beaupuits, J. P., Stutzki, J., Ossenkopf, V., et al. 2015b, A&A, 575, A9

Pérez-Beaupuits, J. P., Wiesemeyer, H., Ossenkopf, V., et al. 2012, A&A, 542, L13

Pety, J., Gratier, P., Guzmán, V., et al. 2012, A&A, 548, A68

Philipp, S. D., Lis, D. C., Güsten, R., et al. 2006, A&A, 454, 213

Pilbratt, G. L., Riedinger, J. R., Passvogel, T., et al. 2010, A&A, 518, L1

Pilleri, P., Fuente, A., Cernicharo, J., et al. 2012, A&A, 544, A110

Pilleri, P., Fuente, A., Gerin, M., et al. 2014, A&A, 561, A69

Pilleri, P., Treviño-Morales, S., Fuente, A., et al. 2013, A&A, 554, A87

Pineda, J. L., Langer, W. D., & Goldsmith, P. F. 2014, A&A, 570, A121

Pineda, J. L., Langer, W. D., Velusamy, T., & Goldsmith, P. F. 2013, A&A, 554, A103

Poglitsch, A., Beeman, J. W., Geis, N., et al. 1990, in Liege International Astrophysical Colloquia, ed. B. Kaldeich, Vol. 29, 149–152

Poglitsch, A., Waelkens, C., Geis, N., et al. 2010, A&A, 518, L2

Pound, M. W. & Wolfire, M. G. 2008, in Astronomical Society of the Pacific Conference Series, Vol. 394, Astronomical Data Analysis Software and Systems XVII, ed. R. W. Argyle, P. S. Bunclark, & J. R. Lewis, 654

Predehl, P. & Schmitt, J. H. M. M. 1995, A&A, 293, 889

Preibisch, T., Balega, Y., Hofmann, K.-H., Weigelt, G., & Zinnecker, H. 1999, New A, 4, 531

Pütz, P., Honingh, C. E., Jacobs, K., et al. 2012, A&A, 542, L2

Racine, R. 1968, AJ, 73, 233

Rayner, T. S. M., Griffin, M. J., Schneider, N., et al. 2017, A&A, 607, A22

Reid, M. A. & Wilson, C. D. 2006, ApJ, 644, 990

Reina, C. & Tarenghi, M. 1973, A&A, 26, 257

Reipurth, B. & Bouchet, P. 1984, A&A, 137, L1

Risacher, C., Güsten, R., Stutzki, J., et al. 2016, A&A, 595, A34

Rizzo, J. R., Fuente, A., Rodríguez-Franco, A., & García-Burillo, S. 2003, ApJl, 597, L153

Roeser, H. P., Schaefer, F., Schmid-Burgk, J., et al. 1987, International Journal of Infrared and Millimeter Waves, 8, 1541

Röllig, M., Abel, N. P., Bell, T., et al. 2007, A&A, 467, 187

Röllig, M. & Ossenkopf, V. 2013, A&A, 550, A56

Röllig, M., Ossenkopf, V., Jeyakumar, S., Stutzki, J., & Sternberg, A. 2006, A&A, 451, 917

Russell, R. W., Melnick, G., Gull, G. E., & Harwit, M. 1980, ApJl, 240, L99

Russell, R. W., Melnick, G., Smyers, S. D., et al. 1981, ApJl, 250, L35

Rybicki, G. B. & Lightman, A. P. 1979, Radiative processes in astrophysics

Savage, C., Apponi, A. J., Ziurys, L. M., & Wyckoff, S. 2002, ApJ, 578, 211

Saykally, R. J. & Evenson, K. M. 1980, ApJl, 238, L107

Schneider, N., Bontemps, S., Motte, F., et al. 2016a, A&A, 591, A40

Schneider, N., Bontemps, S., Motte, F., et al. 2016b, A&A, 587, A74

Scoville, N. Z. & Solomon, P. M. 1974, ApJl, 187, L67

Shaw, G., Ferland, G. J., Abel, N. P., Stancil, P. C., & van Hoof, P. A. M. 2005, ApJ, 624, 794

Simón-Díaz, S., García-Rojas, J., Esteban, C., et al. 2011, A&A, 530, A57

Skinner, S., Gagné, M., & Belzer, E. 2003, ApJ, 598, 375

Smith, D. & Adams, N. G. 1980, ApJ, 242, 424

Smith, D. J. B., Dunne, L., da Cunha, E., et al. 2012, MNRAS, 427, 703

Smith, J., Harper, D. A., & Loewenstein, R. F. 1987, ApJ, 314, 76

Smith, N., Bally, J., Licht, D., & Walawender, J. 2005, AJ, 129, 382

Snell, R. L., Howe, J. E., Ashby, M. L. N., et al. 2000, ApJl, 539, L97

Stacey, G. J., Lugten, J. B., & Genzel, R. 1987, ApJ, 313, 859

Stacey, G. J., Townes, C. H., Geis, N., et al. 1991, ApJl, 382, L37

Stutz, A. M. & Kainulainen, J. 2015, A&A, 577, L6

Stutzki, J. & Güsten, R. 1990, ApJ, 356, 513

Stutzki, J., Stacey, G. J., Genzel, R., et al. 1988, ApJ, 332, 379

Subrahmanyan, R. 1992, MNRAS, 254, 291

Tachiev, G. & Froese Fischer, C. 2001, Canadian Journal of Physics, 79, 955

Tayal, S. S. 2011, The Astrophysical Journal Supplement Series, 195, 12

Thum, C., Lemke, D., Fahrbach, U., & Frey, A. 1978, A&A, 65, 207

Tielens, A. G. G. M. 2005, The Physics and Chemistry of the Interstellar Medium

Tielens, A. G. G. M. & Hollenbach, D. 1985, ApJ, 291, 722

Timmes, F. X., Woosley, S. E., & Weaver, T. A. 1995, ApJS, 98, 617

Treviño-Morales, S. P., Fuente, A., Sánchez-Monge, Á., et al. 2016, A&A, 593, L12

Treviño-Morales, S. P., Pilleri, P., Fuente, A., et al. 2014, A&A, 569, A19

van Dishoeck, E. F. & Black, J. H. 1988, ApJ, 334, 771

Velusamy, T. & Langer, W. D. 2014, A&A, 572, A45

Visser, R., van Dishoeck, E. F., & Black, J. H. 2009, A&A, 503, 323

Wakelam, V. & Herbst, E. 2008, ApJ, 680, 371

Watson, W. D., Anicich, V. G., & Huntress, W. T., J. 1976, ApJ, 205, L165

Wiese, W. L. & Fuhr, J. R. 2007, Journal of Physical and Chemical Reference Data, 36, 1287

Wilson, C. D., Howe, J. E., & Balogh, M. L. 1999, ApJ, 517, 174

Wilson, N. J. & Bell, K. L. 2002, MNRAS, 337, 1027

Wilson, N. J., Bell, K. L., & Hudson, C. E. 2005, A&A, 432, 731

Wilson, T. L. 1999, Reports on Progress in Physics, 62, 143

Wilson, T. L., Hanson, M. M., & Muders, D. 2003, ApJ, 590, 895

Wilson, T. L. & Matteucci, F. 1992, A&AR, 4, 1

Wilson, T. L., Rohlfs, K., & Hüttemeister, S. 2009, Tools of Radio Astronomy (Springer-Verlag)

Wilson, T. L. & Rood, R. 1994, ARA&A, 32, 191

Woods, P. M. & Willacy, K. 2009, ApJ, 693, 1360

Wouterloot, J. G. A. & Brand, J. 1996, A&As, 119, 439

Xu, Y., Moscadelli, L., Reid, M. J., et al. 2011, ApJ, 733, 25

Yau, A. W. & Dalgarno, A. 1976, ApJ, 206, 652

Young, E. T., Becklin, E. E., Marcum, P. M., et al. 2012, ApJl, 749, L17

Zhou, S., Jaffe, D. T., Howe, J. E., et al. 1993, ApJ, 419, 190

A │ OFF Contamination Procedure

The ubiquitous presence of C^+ ISM and the new conditions of observation established by the use of multi-pixels arrays, together with the large size of the observed sources have brought the challenge of selecting a good OFF position, being necessary now not only for a single beam-size position free from emission but also for the whole array. Using the observation of the OFF against a second far away OFF in some cases, or the SKY-HOT spectra in others, a weak contamination in [CII] was detected, and the observed spectra was corrected by adding this emission to the ON-OFF spectra.

A direct addition of the identified OFF emission would add the relative high noise of each spectral element in to the corrected spectra. This can be avoided by first determining a good, few parameter fit to the identified OFF-emission and then add this OFF-source emission model to correct the ON-OFF spectra. For this reason, it was decided to fit a profile composed of multiple gaussians to the OFF positions. Examples of the OFF spectra and their respective gaussian multi-component fits are shown in Figures A.1, A.2 and A.3

Next, with the different OFF gaussian profiles fitted for each pixel of the array, the fit was added to each contaminated spectrum channel by channel, correcting the contamination and recovering the lost emission.

Table A.1: Gaussian parameters for the OFF positions

Source	Gaussian number	Position	Width (FWHM)	T_{peak}
M43 Pos. 0	1	11.4	5.1	1.27
M43 Pos. 0	2	7.7	3.3	1.74
M43 Pos. 1	1	12.6	5.3	0.88
M43 Pos. 1	2	7.3	3.9	1.71
M43 Pos. 2	1	8.2	2.8	1.71
M43 Pos. 2	2	10.8	5.8	1.11
M43 Pos. 3	1	11.0	6.2	0.59

Continued on next page

Table A.1 – *Continued from previous page*

Source	Gaussian number	Position	Width (FWHM)	T_{peak}
M43 Pos. 3	2	9.5	3.8	1.68
M43 Pos. 4	1	11.2	5.2	0.86
M43 Pos. 4	2	8.8	3.4	1.81
M43 Pos. 5	1	12.8	4.3	0.75
M43 Pos. 5	2	8.0	3.3	1.16
M43 Pos. 6	1	9.9	3.2	1.11
M43 Pos. 6	2	6.8	2.5	1.88
MonR2	1	12.1	2.8	1.71
MonR2	2	5.2	8.0	0.46
MonR2	3	10.2	3.4	0.40
MonR2	4	9.0	2.4	2.13
M17SW Pos. 0	1	20.5	4.8	2.18
M17SW Pos. 0	2	15.2	12.7	0.93
M17SW Pos. 0	3	11.1	3.6	0.76
M17SW Pos. 1	1	20.1	4.5	1.58
M17SW Pos. 1	2	15.2	10.8	0.96
M17SW Pos. 1	3	10.7	2.6	0.99
M17SW Pos. 1	4	21.6	1.1	0.29
M17SW Pos. 2	1	19.6	4.1	2.62
M17SW Pos. 2	2	20.3	14.6	0.55
M17SW Pos. 2	3	10.5	4.4	0.71
M17SW Pos. 2	4	23.0	2.1	0.14
M17SW Pos. 3	1	20.5	4.4	3.53
M17SW Pos. 3	2	10.2	7.1	0.42
M17SW Pos. 3	3	9.2	4.1	0.55
M17SW Pos. 3	4	24.4	2.0	0.56
M17SW Pos. 4	1	20.6	3.9	4.70
M17SW Pos. 4	2	11.3	7.5	0.83
M17SW Pos. 4	3	10.6	7.1	0.47
M17SW Pos. 5	1	20.2	5.4	2.62
M17SW Pos. 5	2	12.5	11.9	0.39
M17SW Pos. 5	3	15.0	9.7	1.04
M17SW Pos. 5	4	10.6	2.4	1.17
M17SW Pos. 5	5	21.2	2.3	1.11
M17SW Pos. 6	1	19.0	5.9	2.99

Table A.1 – *Continued from previous page*

Source	Gaussian number	Position	Width (FWHM)	T_{peak}
M17SW Pos. 6	2	23.5	7.3	0.16
M17SW Pos. 6	3	17.4	14.1	0.45
M17SW Pos. 6	4	9.7	5.4	1.20
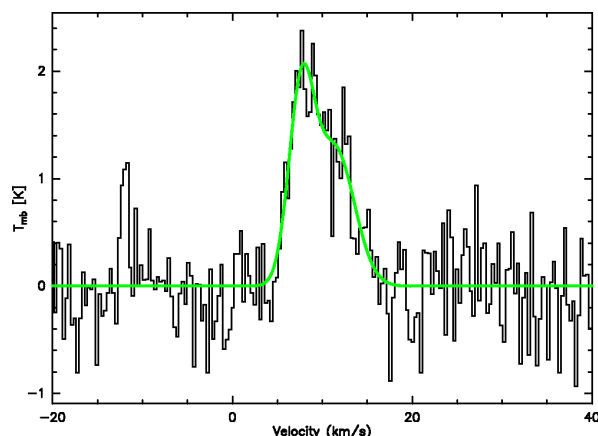
Figure A.1: M43 S-H observation of position 0. The green fit represents the multi-component Gaussian profile fitted to the OFF and added back into the ON-OFF spectra.
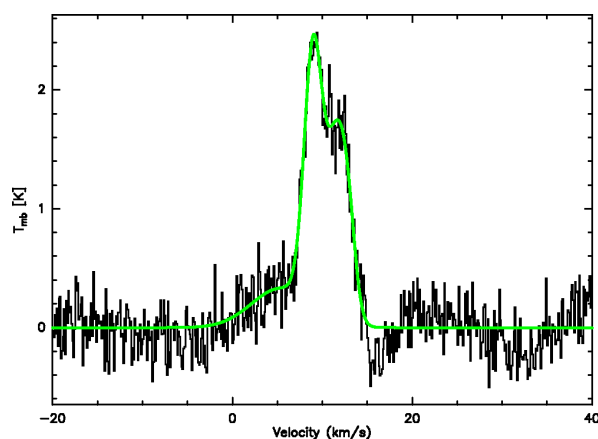
Figure A.2: Mon R2 S-H observation. As in Figure A.1, the green line shows the OFF-correction.
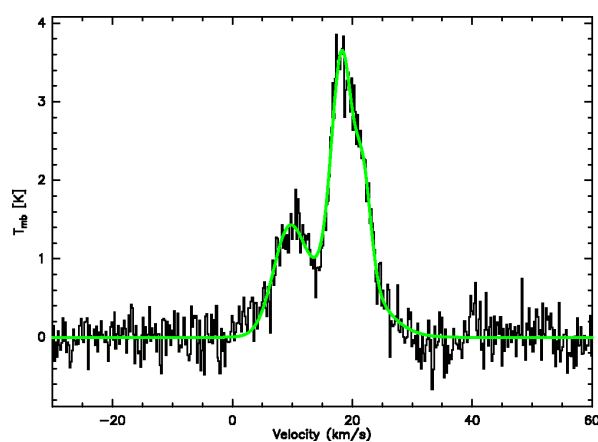
Figure A.3: M17 SW OFF observation of position 6. As in Figure A.1, the green line shows the OFF-correction.

B │ [^{13}CII] Gaussian Fitting Tables

Here we list the multicomponent analysis fit parameters for each position of the different sources.

Table B.4: Gaussian components parameters for M17 SW for the double layer model

Components	T_{ex} (K)	$N_{12,i}$(CII) 10^{18} (cm^{-2})	Vel (km/s)	ΔV (km/s)	τ	A_V
0 Background 1	250.0	8.13	20.8	5.4	1.43	45.19
0 Background 2	200.6	0.14	2.5	9.4	0.02	0.77
0 Background 3	200.0	0.06	33.0	4.5	0.02	0.33
0 Background 4	250.0	0.82	12.5	5.9	0.13	4.58
0 Foreground 1	40.6	0.74	21.4	2.5	1.63	4.09
0 Foreground 2	40.7	0.09	24.1	0.6	0.81	0.48
0 Foreground 3	40.7	0.03	22.4	0.8	0.17	0.14
0 Foreground 4	53.7	0.65	16.4	2.2	1.28	3.61
0 Foreground 5	30.6	0.35	19.0	3.2	0.71	1.96
0 Foreground 6	30.6	0.24	24.1	2.0	0.77	1.34
1 Background 1	200.0	7.76	18.0	5.7	1.61	43.09
1 Background 2	200.0	0.17	10.8	2.7	0.08	0.96
1 Background 3	200.0	0.05	5.1	6.5	0.01	0.27
1 Background 4	200.0	0.02	25.9	1.6	0.01	0.11
1 Background 5	200.0	0.01	8.2	1.4	0.01	0.08
1 Foreground 1	30.0	0.09	24.1	0.6	0.98	0.52
1 Foreground 2	30.0	0.58	21.3	2.5	1.52	3.24
1 Foreground 3	30.0	0.53	16.4	3.7	0.91	2.97
1 Foreground 4	30.9	0.45	18.7	3.2	0.89	2.51
2 Background 1	200.0	4.66	19.3	6.6	0.84	25.90
2 Background 2	200.0	0.51	12.5	5.8	0.11	2.84
2 Background 3	200.0	0.43	12.5	19.5	0.03	2.41
2 Background 4	200.0	0.04	34.8	6.2	0.01	0.21
2 Foreground 1	30.0	0.61	24.3	3.1	1.24	3.38

Continued on next page

Table B.4 – *Continued from previous page*

Components	T_{ex}	$N_{12,i}$(CII)	Vel	ΔV	τ	A_V
	(K)	10^{18} (cm^{-2})	(km/s)	(km/s)		
2 Foreground 2	30.0	0.55	21.2	2.2	1.58	3.03
2 Foreground 3	52.2	0.91	16.0	3.6	1.14	5.06
2 Foreground 4	50.0	0.55	14.0	2.7	0.97	3.07
2 Foreground 5	30.0	0.35	19.1	2.8	0.80	1.93
3 Background 1	180.0	2.92	22.0	5.9	0.66	16.23
3 Background 2	150.0	0.69	15.4	29.4	0.04	3.82
3 Background 3	150.0	0.72	10.9	4.5	0.26	4.00
3 Background 4	150.0	0.04	46.2	12.3	0.01	0.25
3 Foreground 1	25.0	0.51	21.3	2.2	1.61	2.85
3 Foreground 2	25.0	0.26	23.7	1.4	1.32	1.45
4 Background 1	200.0	4.00	19.4	4.2	1.14	22.22
4 Background 2	200.0	2.63	24.5	4.8	0.65	14.58
4 Background 3	200.0	0.62	11.5	4.6	0.16	3.42
4 Background 4	200.0	0.27	20.6	40.5	0.01	1.52
4 Background 5	200.0	0.04	31.3	3.4	0.01	0.23
4 Foreground 1	30.0	0.38	21.4	2.7	0.90	2.12
4 Foreground 2	30.0	0.14	23.8	1.0	0.86	0.76
4 Foreground 3	41.0	0.26	26.8	3.8	0.36	1.42
4 Foreground 4	30.9	0.27	16.6	3.0	0.56	1.47
4 Foreground 5	30.0	0.21	19.6	2.3	0.56	1.14
5 Background 1	200.0	1.14	23.9	5.7	0.24	6.32
5 Background 2	200.0	0.38	29.8	12.4	0.04	2.09
5 Background 3	200.0	1.52	14.3	8.2	0.22	8.42
5 Background 4	200.0	0.03	2.5	3.8	0.01	0.17
5 Foreground 1	30.0	0.14	18.4	2.2	0.42	0.80
5 Foreground 2	30.0	0.07	23.9	0.7	0.63	0.38
5 Foreground 3	30.0	0.18	12.7	2.5	0.46	1.02
6 Background 1	250.0	5.20	20.9	4.4	1.11	28.89
6 Background 2	200.0	1.65	20.6	9.8	0.20	9.15
6 Background 3	200.0	0.15	10.9	4.5	0.04	0.85
6 Background 4	200.0	0.64	15.7	4.2	0.18	3.55
6 Background 5	200.0	0.04	31.7	5.7	0.01	0.25
6 Foreground 1	40.5	0.32	19.1	2.4	0.72	1.79
6 Foreground 2	45.3	0.76	21.6	2.6	1.46	4.20
6 Foreground 3	39.9	0.57	17.2	3.4	0.92	3.18

Continued on next page

Components	T_{ex}	$N_{12,i}$(CII)	Vel	ΔV	τ	A_V
	(K)	10^{18} (cm^{-2})	(km/s)	(km/s)		
6 Foreground 4	41.5	0.14	24.1	0.7	1.06	0.79

Table B.6: Gaussian components parameters for M17 SW considering a single layer model

Components	T_{ex}	$N_{12,i}$(CII)	Vel	ΔV	τ	A_V
	(K)	10^{18} (cm^{-2})	(km/s)	(km/s)		
0 Background 1	52.0	3.21	20.5	3.6	4.03	17.84
0 Background 2	50.0	16.22	20.7	5.5	13.88	90.12
0 Background 3	50.0	0.14	35.7	8.8	0.08	0.79
0 Background 4	50.0	1.30	12.7	7.6	0.80	7.20
0 Background 5	50.0	0.27	1.5	7.5	0.17	1.48
0 Background 6	50.0	1.64	12.5	4.3	1.78	9.09
0 Background 7	50.0	1.29	18.6	2.1	2.92	7.15
0 Background 8	50.0	0.40	19.5	1.6	1.20	2.24
0 Background 9	50.0	0.11	24.9	0.7	0.74	0.60
0 Background 10	50.0	0.82	23.0	0.8	4.67	4.56
0 Background 11	50.0	0.43	25.5	3.9	0.52	2.41
1 Background 1	50.0	13.15	18.6	5.6	10.96	73.04
1 Background 2	45.0	2.33	14.1	9.7	1.22	12.97
1 Background 3	45.0	8.14	17.2	2.9	14.02	45.20
1 Background 4	45.0	1.01	13.1	3.4	1.49	5.60
2 Background 1	50.0	9.86	19.5	5.7	8.04	54.76
2 Background 2	45.0	2.44	12.1	5.9	2.12	13.57
2 Background 3	50.0	1.13	14.0	7.1	0.75	6.30
2 Background 4	50.0	1.73	18.4	2.1	3.87	9.61
2 Background 5	50.0	0.20	2.6	6.5	0.14	1.09
2 Background 6	50.0	0.08	26.7	2.3	0.16	0.43
2 Background 7	50.0	0.04	22.7	0.9	0.22	0.24
3 Background 1	40.0	6.57	21.7	5.0	7.26	36.52
3 Background 2	45.0	0.53	23.1	1.2	2.28	2.97
3 Background 3	75.3	0.89	10.7	3.6	0.79	4.93
3 Background 4	70.0	0.29	2.1	19.7	0.05	1.61
3 Background 5	70.0	0.80	13.7	10.7	0.26	4.45
3 Background 6	70.0	0.69	19.1	2.1	1.14	3.83
3 Background 7	70.0	0.61	25.7	2.2	0.94	3.37

Table B.6 – *Continued from previous page*

Components	T$_{ex}$	N$_{12,i}$(CII)	Vel	ΔV	τ	A$_V$
	(K)	10^{18} (cm^{-2})	(km/s)	(km/s)		
3 Background 8	70.0	0.02	19.8	0.8	0.07	0.09
3 Background 9	70.0	0.20	35.9	15.9	0.04	1.13
3 Background 10	70.0	0.06	22.3	0.8	0.25	0.33
3 Background 11	70.0	0.05	28.1	1.4	0.14	0.30
3 Background 12	70.0	0.08	24.9	0.8	0.33	0.43
4 Background 1	55.0	7.35	19.4	4.2	7.59	40.85
4 Background 2	44.2	1.44	24.5	2.6	2.89	8.03
4 Background 3	55.0	0.79	18.1	1.6	2.16	4.41
4 Background 4	55.0	0.97	16.9	19.6	0.22	5.41
4 Background 5	55.0	1.81	11.4	3.0	2.58	10.07
4 Background 6	55.0	1.85	26.6	2.6	3.07	10.30
4 Background 7	55.0	0.62	25.6	1.8	1.44	3.43
4 Background 8	55.0	1.64	19.4	1.9	3.76	9.11
4 Background 9	55.0	0.10	21.1	1.2	0.35	0.53
4 Background 10	60.0	0.84	22.7	1.2	2.80	4.65
4 Background 11	55.0	0.46	28.9	24.2	0.08	2.53
4 Background 12	55.0	0.42	24.8	0.8	2.33	2.31
5 Background 1	55.0	2.25	23.9	6.3	1.54	12.51
5 Background 2	55.0	2.87	14.3	8.0	1.54	15.97
5 Background 3	55.0	0.57	15.3	2.5	0.98	3.14
5 Background 4	55.0	0.80	29.5	11.2	0.31	4.43
5 Background 5	55.0	0.23	10.9	3.0	0.34	1.30
5 Background 6	55.0	0.16	21.1	1.7	0.40	0.88
5 Background 7	55.0	0.38	25.3	1.6	1.01	2.11
5 Background 8	55.0	0.34	22.9	1.0	1.49	1.91
5 Background 9	55.0	0.08	2.8	4.5	0.08	0.45
6 Background 1	60.0	5.28	20.5	9.4	2.25	29.3
6 Background 2	60.0	7.84	21.1	2.8	11.26	43.5
6 Background 3	60.0	1.22	14.8	6.3	0.78	6.8
6 Background 4	60.0	0.13	20.2	1.0	0.53	0.7
6 Background 5	60.0	0.02	32.6	4.5	0.02	0.1
6 Background 6	60.0	0.23	24.9	0.9	1.06	1.3
6 Background 7	60.0	0.68	23.1	0.8	3.35	3.8

Table B.1: Gaussian components parameters for M43

Components	T_{ex} (K)	$N_{12,i}$(CII) 10^{18} (cm^{-2})	Vel (km/s)	ΔV (km/s)	τ	A_V
0 Background 1	110.7	1.99	10.0	2.1	2.07	11.07
0 Background 2	55.4	0.63	5.0	1.9	1.42	3.49
0 Background 3	43.1	0.72	7.5	1.3	2.96	3.99
0 Background 4	33.2	0.54	3.5	3.1	1.09	3.02
0 Background 5	55.0	0.21	12.1	3.4	0.27	1.19
1 Background 1	97.3	1.81	9.3	2.6	1.75	10.04
1 Background 2	90.5	0.32	5.7	2.9	0.30	1.80
1 Background 3	54.4	0.15	3.5	7.6	0.09	0.83
1 Background 4	38.5	0.47	11.6	3.3	0.80	2.63
1 Background 5	23.3	0.17	16.5	2.3	0.52	0.96
2 Background 1	52.3	0.89	10.0	2.8	1.43	4.92
2 Background 2	60.0	1.58	8.1	5.0	1.27	8.77
3 Background 1	76.4	0.32	10.2	2.4	0.43	1.77
3 Background 2	70.0	0.77	8.0	4.5	0.60	4.30
4 Background 1	108.4	1.44	10.4	1.9	1.68	8.01
4 Background 2	44.0	0.15	1.4	4.6	0.17	0.86
4 Background 3	80.0	0.48	4.9	2.6	0.57	2.69
4 Background 4	79.6	0.20	12.1	2.6	0.24	1.13
4 Background 5	50.6	0.25	8.6	1.0	1.19	1.41
4 Background 6	99.9	0.13	7.6	1.5	0.20	0.70
5 Background 1	108.0	1.10	10.7	2.5	0.98	6.11
5 Background 2	45.0	0.12	1.3	6.8	0.09	0.66
5 Background 3	70.0	0.18	4.8	1.7	0.37	1.01
5 Background 4	66.7	0.61	8.0	6.7	0.33	3.37
6 Background 1	101.4	1.83	9.7	2.7	1.66	10.16
6 Background 2	39.7	0.20	2.3	6.1	0.18	1.13
6 Background 3	80.0	0.28	4.9	2.4	0.36	1.58
6 Background 4	30.5	0.20	12.7	1.4	0.92	1.12
6 Background 5	32.4	0.45	6.9	1.2	2.41	2.50

Table B.2: Gaussian components parameters for Horsehead PDR

Components	T_{ex} (K)	$N_{12,i}$(CII) 10^{18} (cm^{-2})	Vel (km/s)	ΔV (km/s)	τ	A_V
0 Background 1	38.0	0.27	10.6	0.7	2.16	1.53
0 Background 2	55.0	0.30	10.6	1.4	0.93	1.67
0 Background 3	31.5	0.10	17.6	14.7	0.04	0.56
0 Background 4	40.0	0.11	11.6	5.3	0.12	0.63
1 Background 1	26.7	0.11	10.5	1.0	0.78	0.62
1 Background 2	24.5	0.21	10.8	2.5	0.58	1.16
1 Background 3	36.1	0.14	14.3	18.4	0.04	0.76
1 Background 4	23.6	0.11	13.8	2.5	0.31	0.63
2 Background 1	37.2	0.20	10.5	0.7	1.66	1.10
2 Background 2	35.5	0.40	10.4	1.3	1.80	2.23
2 Background 3	32.0	0.16	11.8	4.8	0.22	0.92
2 Background 4	39.7	0.08	14.4	17.7	0.03	0.47
3 Background 1	38.0	0.17	10.5	0.7	1.34	0.96
3 Background 2	39.8	0.25	10.6	1.5	0.90	1.36
3 Background 3	31.9	0.17	11.9	3.9	0.26	0.92
3 Background 4	53.8	0.04	17.0	13.2	0.01	0.20
4 Background 1	35.5	0.14	10.8	1.1	0.75	0.78
4 Background 2	31.4	0.14	10.9	2.7	0.32	0.76
4 Background 3	27.2	0.11	20.3	9.8	0.08	0.63
4 Background 4	50.1	0.04	13.3	4.4	0.04	0.21
5 Background 1	48.0	0.06	10.7	1.0	0.27	0.31
5 Background 2	31.6	0.17	10.9	2.0	0.52	0.93
5 Background 3	66.2	0.02	17.9	13.0	0.01	0.11
5 Background 4	31.3	0.11	12.7	4.8	0.15	0.63
6 Background 1	43.0	0.48	10.7	0.9	2.84	2.67
6 Background 2	40.4	0.41	10.6	1.5	1.52	2.29
6 Background 3	44.6	0.07	10.8	3.3	0.11	0.39
6 Background 4	23.3	0.27	12.9	4.5	0.42	1.49
6 Background 5	29.7	0.08	18.3	8.5	0.06	0.45

Table B.3: Gaussian components parameters for Mon R2 for the double layer model

Components	T_{ex} (K)	$N_{12,i}$(CII) 10^{18} (cm^{-2})	Vel (km/s)	ΔV (km/s)	τ	A_V
1 Background 1	160.0	2.37	8.8	3.6	0.98	13.14
1 Background 2	150.0	1.12	12.4	9.6	0.19	6.20
1 Background 3	150.0	0.11	31.2	9.9	0.02	0.62
1 Background 4	150.0	0.54	18.2	11.6	0.08	3.02
1 Background 5	150.0	0.09	6.4	20.2	0.01	0.49
1 Foreground 1	20.0	0.24	11.4	1.5	1.14	1.32
1 Foreground 2	20.0	0.59	8.8	4.2	0.99	3.28
2 Background 1	150.0	0.33	12.0	12.3	0.04	1.83
2 Background 2	150.0	1.20	8.5	9.8	0.20	6.67
2 Background 3	150.0	2.49	10.8	5.8	0.69	13.83
2 Background 4	150.0	0.64	11.0	1.0	1.03	3.56
2 Background 5	150.0	0.01	3.6	3.8	0.01	0.08
2 Background 6	150.0	0.01	20.1	2.8	0.01	0.08
2 Foreground 1	20.0	0.16	12.0	1.1	1.03	0.88
2 Foreground 2	20.0	0.09	7.3	1.7	0.38	0.49
2 Foreground 3	20.0	0.25	11.1	1.2	1.52	1.37
2 Foreground 4	20.0	0.14	9.7	4.1	0.24	0.76

Table B.5: Gaussian components parameters for Mon R2 considering a single layer model

Components	T_{ex} (K)	$N_{12,i}$(CII) 10^{18} (cm^{-2})	Vel (km/s)	ΔV (km/s)	τ	A_V
1 Background 1	70.0	2.51	8.3	3.3	2.62	13.4
1 Background 2	35.0	2.85	14.7	25.1	0.68	15.8
1 Background 3	50.0	0.56	20.1	4.8	0.55	3.1
1 Background 4	50.0	0.03	5.4	2.9	0.04	0.2
1 Background 5	70.0	1.19	14.7	4.3	0.96	6.6
2 Background 1	40.4	2.44	10.8	1.3	10.17	13.6
2 Background 2	27.7	10.89	8.7	12.5	5.75	60.5
2 Background 3	95.6	1.08	6.7	4.9	0.56	6.0
2 Background 4	120.0	0.07	10.4	0.7	0.20	0.4
2 Background 5	85.0	0.22	13.0	1.0	0.61	1.2
2 Background 6	85.0	0.31	15.3	3.7	0.24	1.7
2 Background 7	85.0	0.58	13.8	2.1	0.78	3.2
2 Background 8	120.0	0.57	9.3	1.9	0.60	3.2

Table B.7: Gaussian components parameters for the Horsehead PDR for Position 6 considering a beam filling factor of 0.5

Components	T_{ex} (K)	$N_{12,i}$(CII) 10^{18} (cm^{-2})	Vel (km/s)	ΔV (km/s)	τ	A_V
Background 1	57.0	0.63	10.7	0.9	3.07	3.49
Background 2	57.3	0.57	10.6	1.5	1.63	3.18
Background 3	60.8	0.12	11.4	4.2	0.11	0.66
Background 4	47.2	0.08	16.1	7.7	0.05	0.43
Background 5	24.6	0.04	22.8	1.5	0.19	0.23

Table B.8: Gaussian components parameters for the Horsehead PDR for Position 6 considering a beam filling factor of 0.3

Components	T_{ex} (K)	$N_{12,i}$(CII) 10^{18} (cm^{-2})	Vel (km/s)	ΔV (km/s)	τ	A_V
Background 1	73.4	0.81	10.7	0.8	3.19	4.52
Background 2	79.3	0.72	10.6	1.5	1.49	3.98
Background 3	104.1	0.13	11.5	4.4	0.07	0.71
Background 4	50.0	0.13	16.8	9.5	0.06	0.71

Table B.9: Gaussian components parameters for Mon R2 for Position 1 considering a beam filling factor of 0.5

Components	T_{ex} (K)	$N_{12,i}$(CII) 10^{18} (cm^{-2})	Vel (km/s)	ΔV (km/s)	τ	A_V
Background 1	220.0	4.33	8.8	3.6	1.28	24.04
Background 2	200.0	3.44	13.4	9.6	0.43	19.11
Background 3	170.0	0.33	29.0	10.9	0.04	1.82
Background 4	170.0	0.15	22.1	3.8	0.06	0.86
Background 5	160.0	0.14	4.4	10.4	0.02	0.78
Foreground 1	40.0	0.31	11.5	1.3	1.34	1.72
Foreground 2	30.0	0.81	9.3	5.7	0.92	4.51
Foreground 3	30.0	0.06	16.6	4.0	0.09	0.31
Foreground 4	30.0	0.01	8.3	1.1	0.06	0.06

Table B.10: Gaussian components parameters for MonR2 for Position 1 considering an absorbing factor of 0.9

Components	T_{ex} (K)	$N_{12,i}$(CII) 10^{18} (cm^{-2})	Vel (km/s)	ΔV (km/s)	τ	A_V
Background 1	160.0	2.37	8.8	3.6	0.98	13.17
Background 2	150.0	1.12	12.4	9.6	0.19	6.20
Background 3	150.0	0.53	17.6	11.4	0.08	2.95
Background 4	150.0	0.12	31.2	9.9	0.02	0.69
Background 5	150.0	0.06	4.4	20.2	0.00	0.32
Foreground 1	35.0	1.14	11.5	1.1	6.26	6.32
Foreground 2	30.0	0.88	8.9	4.2	1.34	4.91

Table B.11: Gaussian components parameters for Mon R2 for Position 1 considering an absorbing factor of 0.75

Components	T_{ex} (K)	$N_{12,i}$(CII) 10^{18} (cm^{-2})	Vel (km/s)	ΔV (km/s)	τ	A_V
Background 1	160.0	2.37	8.8	3.6	0.98	13.17
Background 2	150.0	1.12	12.4	9.6	0.19	6.20
Background 3	150.0	0.53	17.6	11.4	0.08	2.95
Background 4	150.0	0.12	31.2	9.9	0.02	0.69
Background 5	150.0	0.06	4.4	20.2	0.00	0.32
Foreground 1	30.0	1.62	11.3	1.3	7.72	9.02
Foreground 2	30.0	0.85	8.8	2.3	2.39	4.71
Foreground 3	30.0	0.40	6.6	4.0	0.64	2.21

C ⏐ [^{13}CII] Fitting Procedure Figures

This Appendix shows the results of the multicomponent fitting process for each source. Each plot is built in the same way. The top left panel represents the fitted model in green and the observed spectrum in red. The middle left panel corresponds to a zoom of the fitted model and the observed spectrum to show the [^{13}CII] satellites. The bottom left panel represents the residual between the observed spectrum and the model. For the top right panel, each emitting component is plotted in blue, the resulting background emitting model in cyan, made from the addition of all the blue components and the observed spectrum in red. Finally, the bottom right panel shows the optical depth of each absorbing Gaussian component in pink.

C.1 M43 Multicomponent Analysis
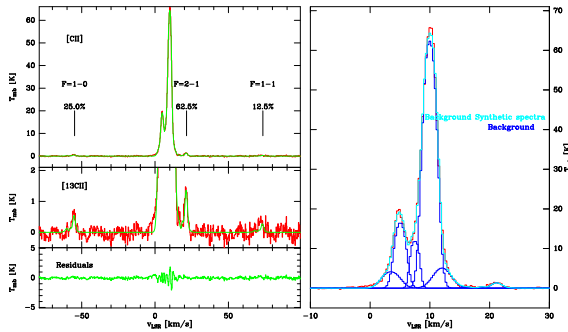
Figure C.1: M43 position 0 fitting result for the multicomponent model
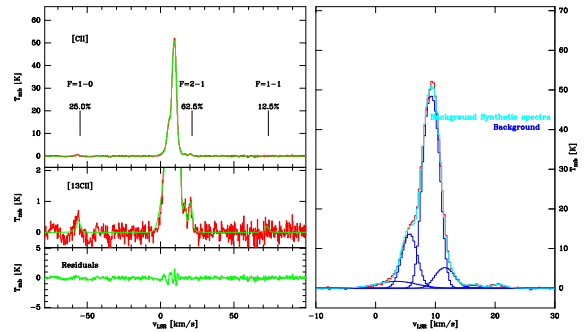
Figure C.2: M43 position 1 fitting result for the multicomponent model

Figure C.3: M43 position 2 fitting result for the multicomponent model
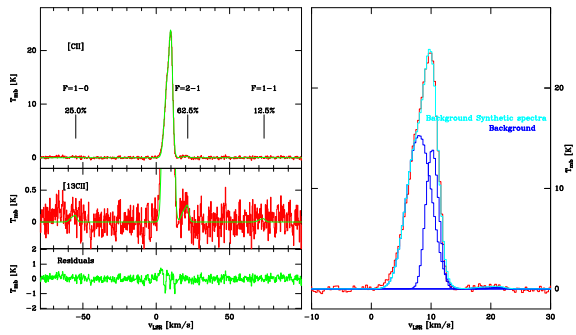
Figure C.4: M43 position 3 fitting result for the multicomponent model
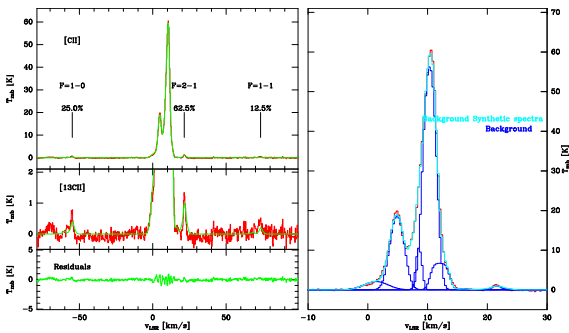
Figure C.5: M43 position 4 fitting result for the multicomponent model
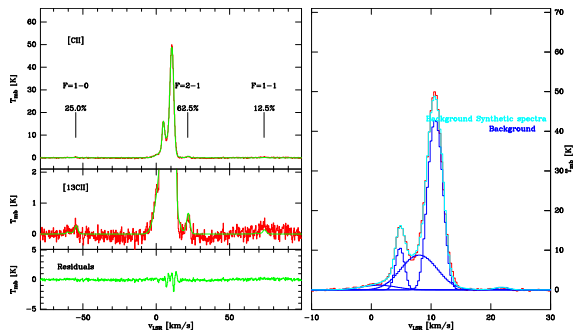
Figure C.6: M43 position 5 fitting result for the multicomponent model
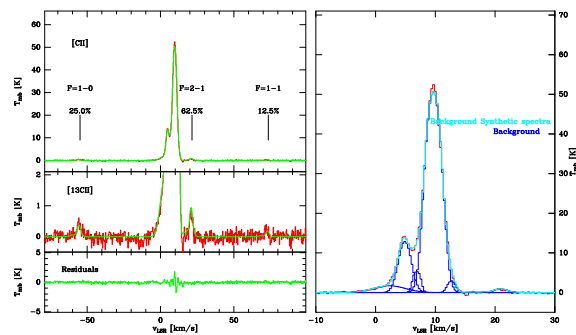
Figure C.7: M43 position 6 fitting result for the multicomponent model

C.2 The Horsehead PDR Multicomponent Analysis
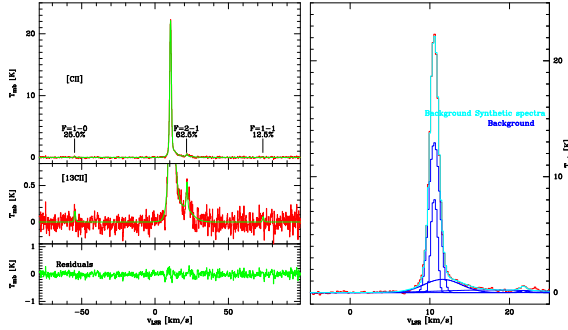
Figure C.8: The Horsehead PDR position 0 fitting result for the multicomponent model
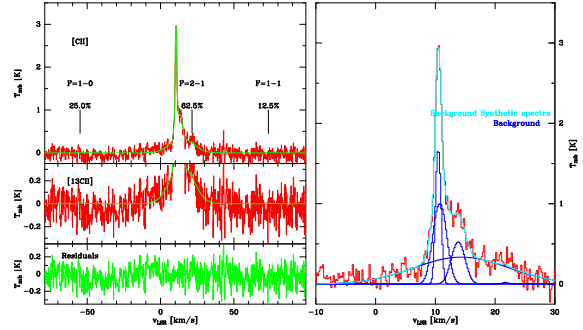
Figure C.9: The Horsehead PDR position 1 fitting result for the multicomponent model
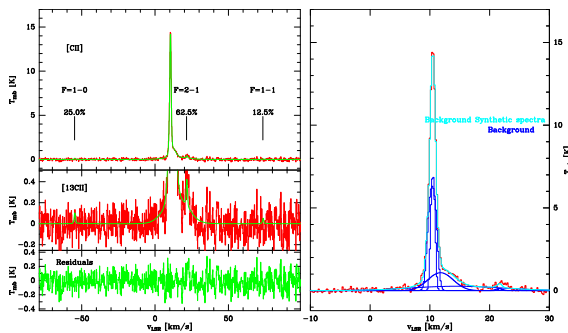
Figure C.10: The Horsehead PDR position 2 fitting result for the multicomponent model
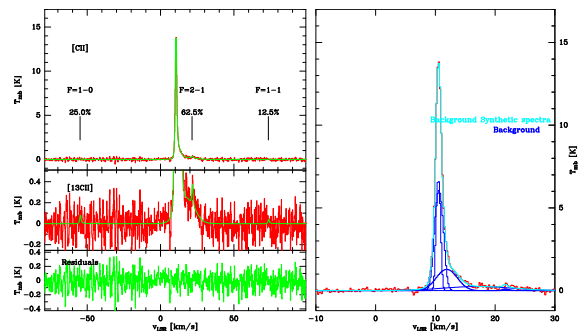
Figure C.11: The Horsehead PDR position 3 fitting result for the multicomponent model

145
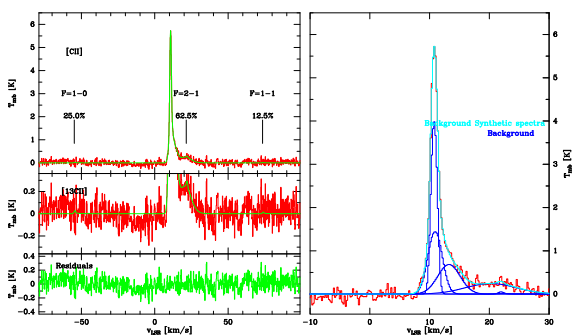
Figure C.12: The Horsehead PDR position 4 fitting result for the multicomponent model
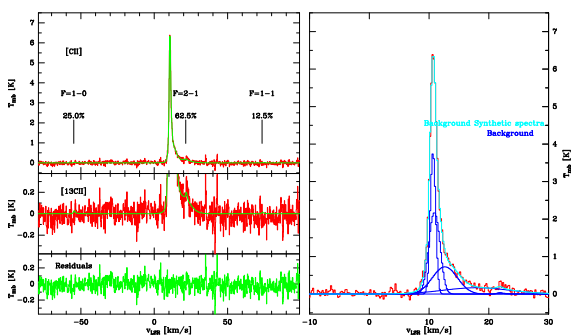
Figure C.13: The Horsehead PDR position 5 fitting result for the multicomponent model
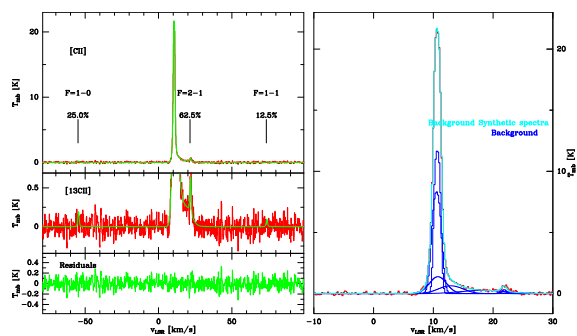
Figure C.14: The Horsehead PDR position 6 fitting result for the multicomponent model

C.3 Monoceros R2 Multicomponent Analysis Dual Layer
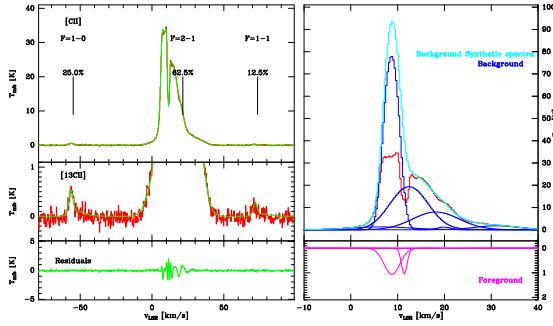
Figure C.15: Monoceros R2 position 1 fitting result for the multicomponent dual layer model
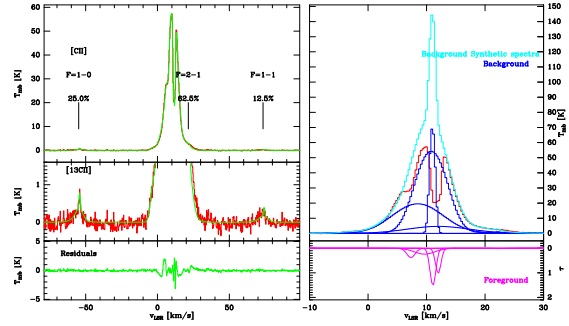
Figure C.16: Monoceros R2 position 2 fitting result for the multicomponent dual layer model

C.4 M17 SW Multicomponent Analysis Dual Layer
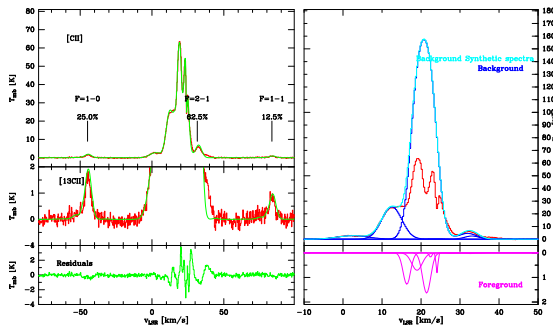
Figure C.17: M17 SW position 0 fitting result for the multicomponent dual layer model
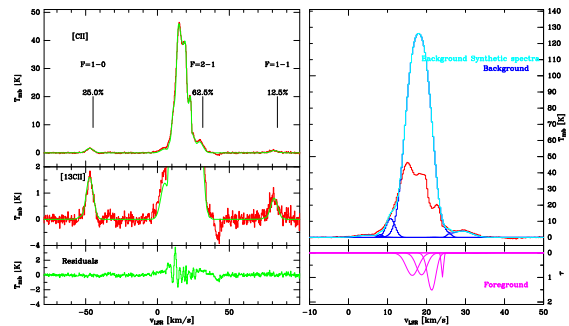
Figure C.18: M17 SW position 1 fitting result for the multicomponent dual layer model
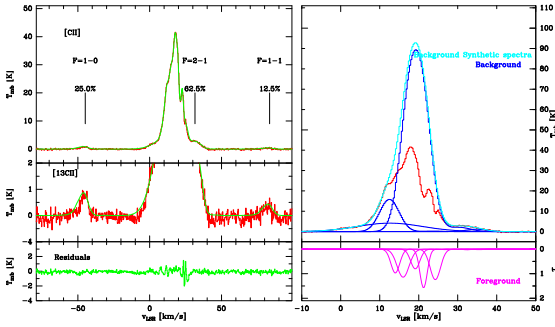
Figure C.19: M17 SW position 2 fitting result for the multicomponent dual layer model
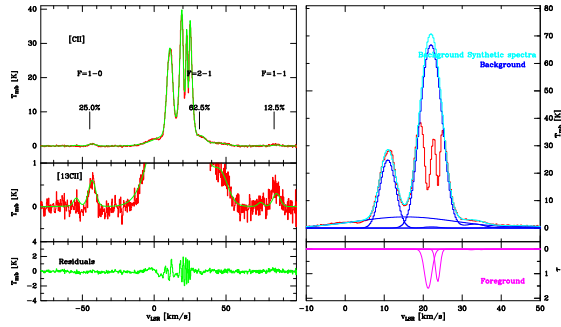
Figure C.20: M17 SW position 3 fitting result for the multicomponent dual layer model
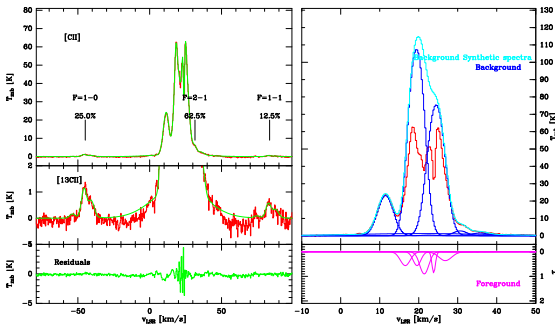
Figure C.21: M17 SW position 4 fitting result for the multicomponent dual layer model
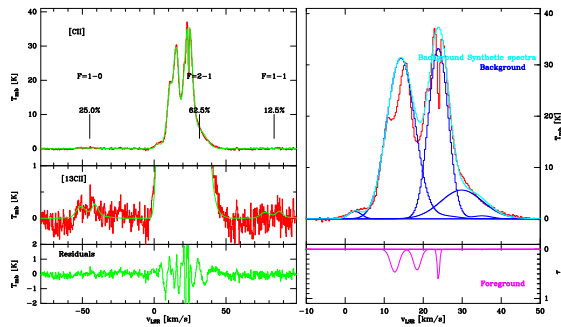
Figure C.22: M17 SW position 5 fitting result for the multicomponent dual layer model
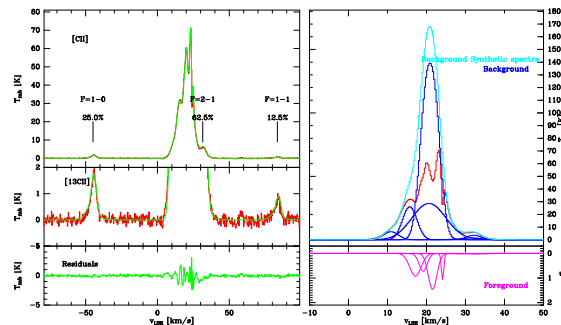
Figure C.23: M17 SW position 6 fitting result for the multicomponent dual layer model

C.5 Monoceros R2 Multicomponent Analysis Single Layer
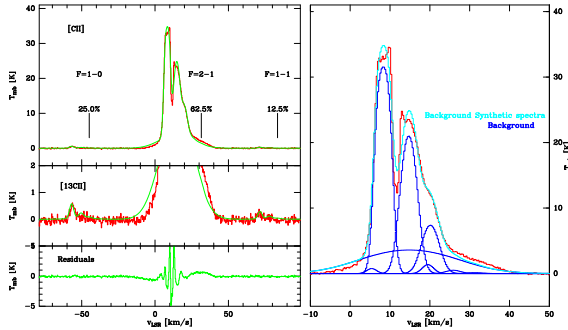
Figure C.24: Monoceros R2 position 1 fitting result for the multicomponent single layer model
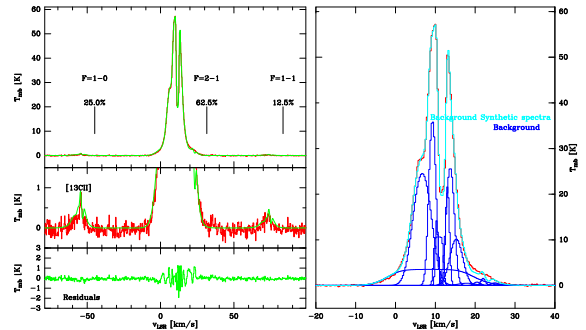
Figure C.25: Monoceros R2 position 2 fitting result for the multicomponent single layer model

C.6 M17 SW Multicomponent Analysis Single Layer
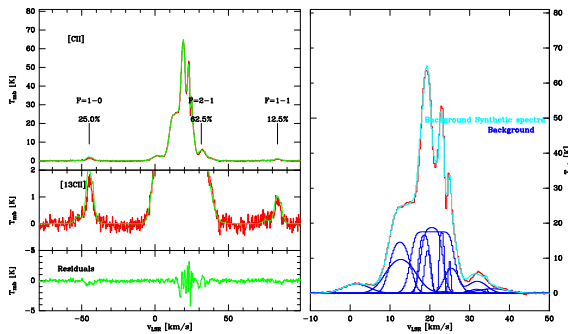
Figure C.26: M17 SW position 0 fitting result for the multicomponent single layer model
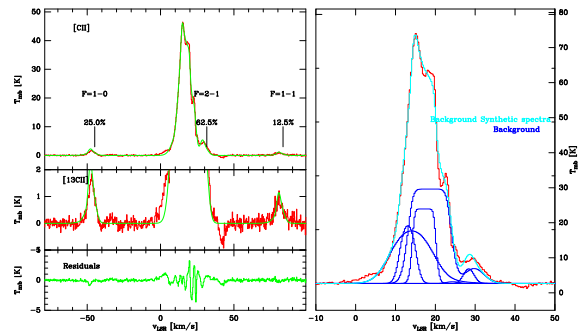
Figure C.27: M17 SW position 1 fitting result for the multicomponent single layer model
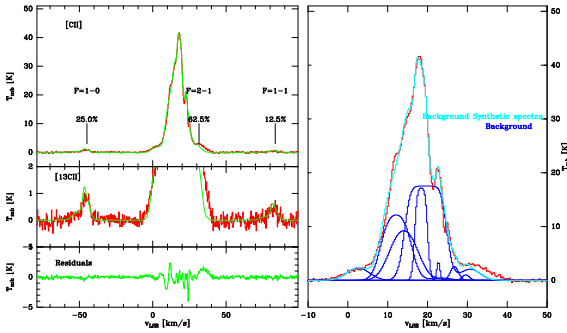
Figure C.28: M17 SW position 2 fitting result for the multicomponent single layer model
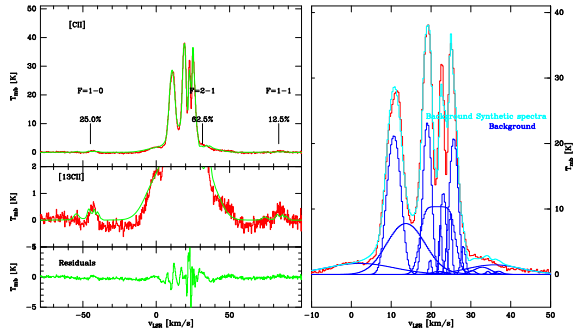
Figure C.29: M17 SW position 3 fitting result for the multicomponent single layer model
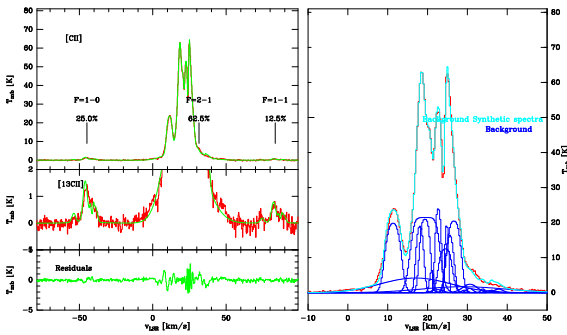
Figure C.30: M17 SW position 4 fitting result for the multicomponent single layer model
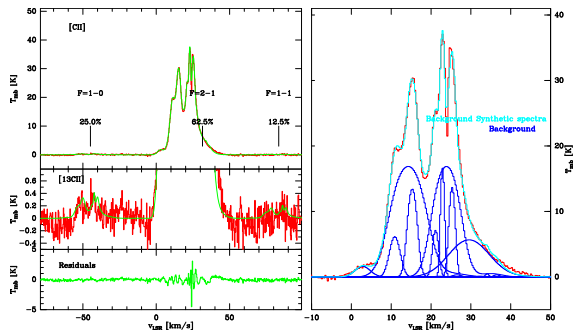
Figure C.31: M17 SW position 5 fitting result for the multicomponent single layer model
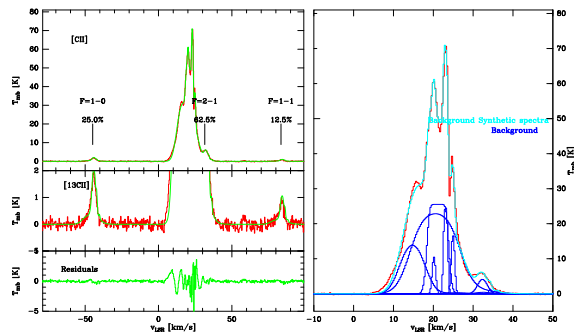
Figure C.32: M17 SW position 6 fitting result for the multicomponent single layer model

C.7 Beam Filling and Absorption Factors
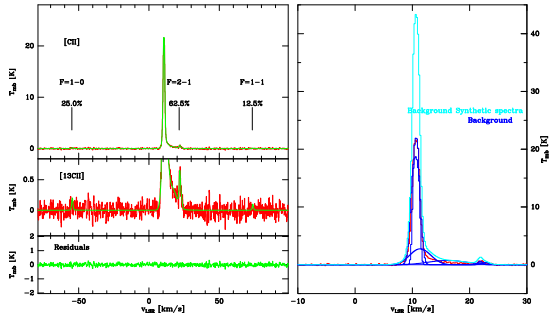
Figure C.33: The Horsehead PDR position 6 fitting result for a $\Phi_{ff} = 0.5$
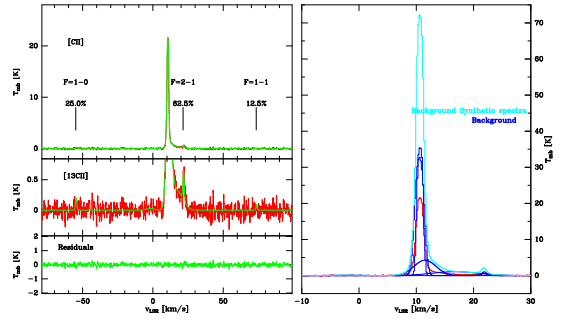
Figure C.34: The Horsehead PDR position 6 fitting result for a $\Phi_{ff} = 0.3$
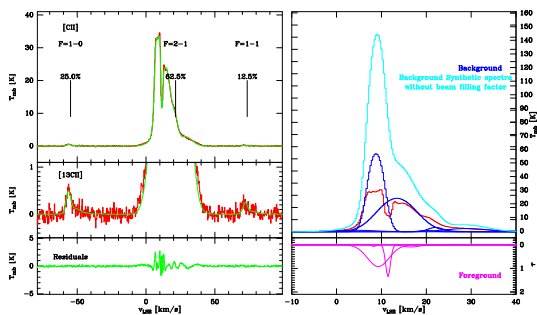
Figure C.35: Monoceros R2 position 1 fitting result for a $\Phi_{ff} = 0.5$
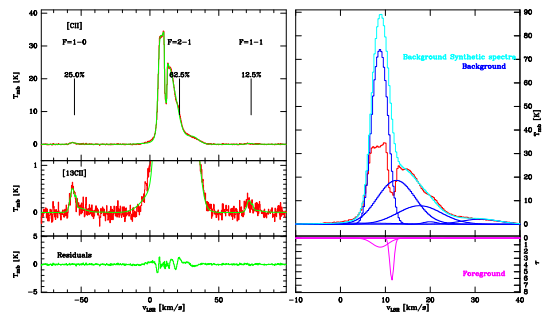
Figure C.36: Monoceros R2 position 1 fitting result for a $\Phi_{af} = 0.9$
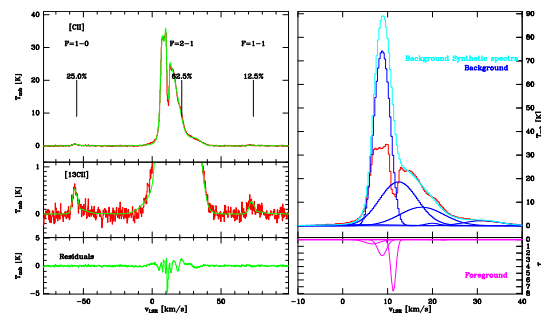
Figure C.37: Monoceros R2 position 1 fitting result for a $\Phi_{\mathrm{af}} = 0.75$

D | [CI] Integrated Intensity Channel Maps

[CI] ^{3}P$_2$-^{3}P$_1$ integrated intensity maps between 10 and 30 km/s of the whole region, M17 N and M17 SW in veloity biens of 1 km/s. The contour levels increases in steps of 10% with respect to the absolute peak integrated intensity value for all the channels. For this case, correspons to 42 K km/s.
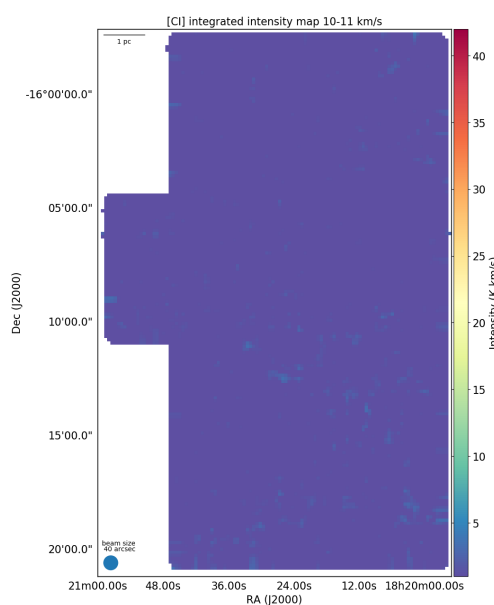
Figure D.1: [CI] ^{3}P$_1$-^{3}P$_0$ integrated intensity map between 10 and 11 km/s.
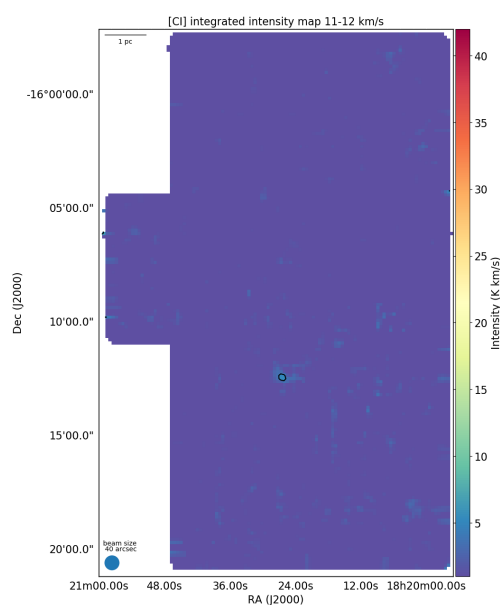
Figure D.2: [CI] ^{3}P$_1$-^{3}P$_0$ integrated intensity map between 11 and 12 km/s.

Figure D.3: [CI] $^3P_1$-$^3P_0$ integrated intensity map between 12 and 13 km/s.
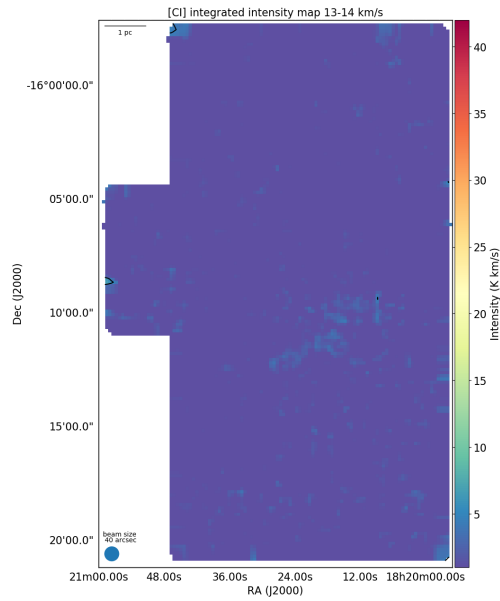
Figure D.4: [CI] $^3P_1$-$^3P_0$ integrated intensity map between 13 and 14 km/s.
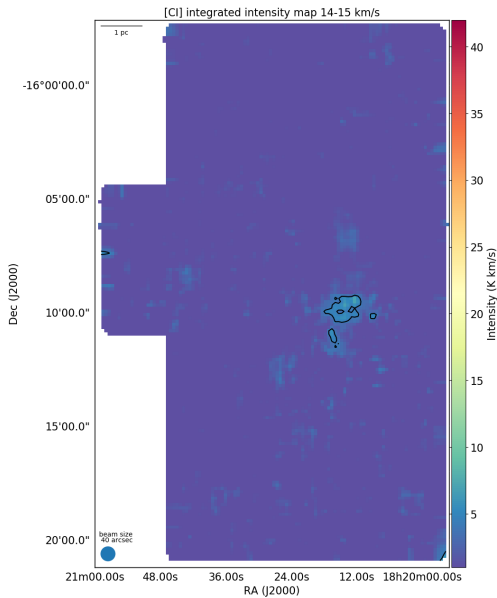
Figure D.5: [CI] $^3P_1$-$^3P_0$ integrated intensity map between 14 and 15 km/s.
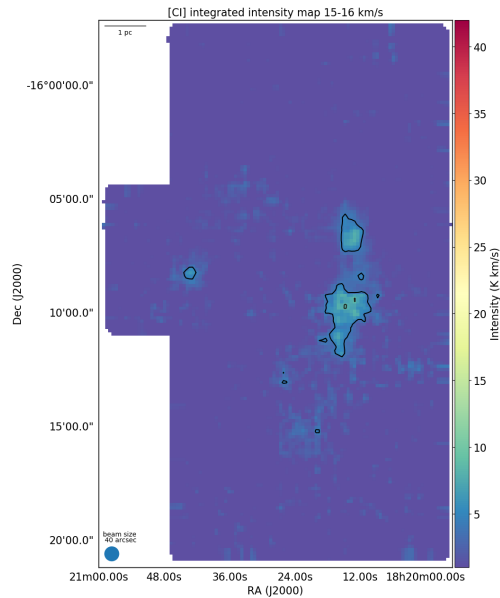
Figure D.6: [CI] $^3P_1$-$^3P_0$ integrated intensity map between 15 and 16 km/s.
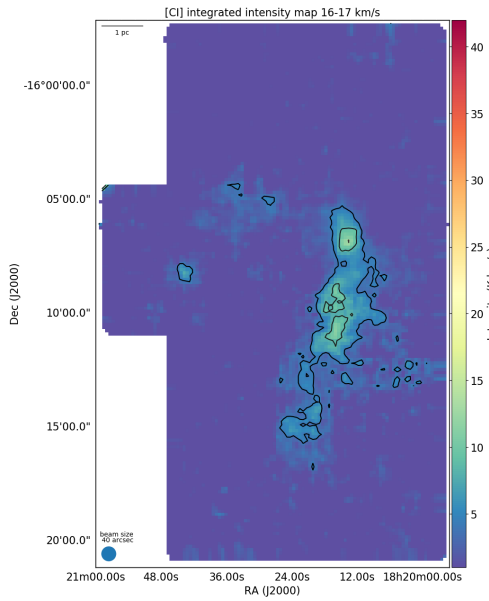
Figure D.7: [CI] $^3P_1$-$^3P_0$ integrated intensity map between 16 and 17 km/s.
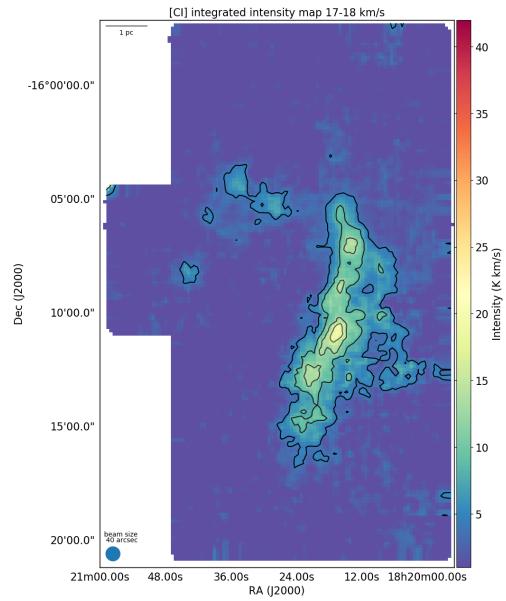
Figure D.8: [CI] $^3P_1$-$^3P_0$ integrated intensity map between 17 and 18 km/s.
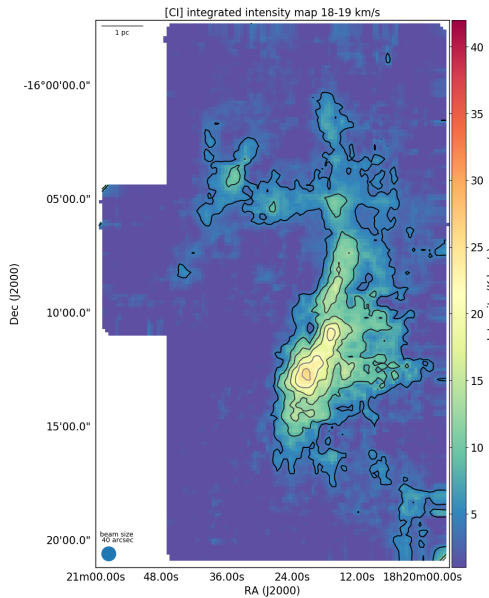
Figure D.9: [CI] $^3P_1$-$^3P_0$ integrated intensity map between 18 and 19 km/s.
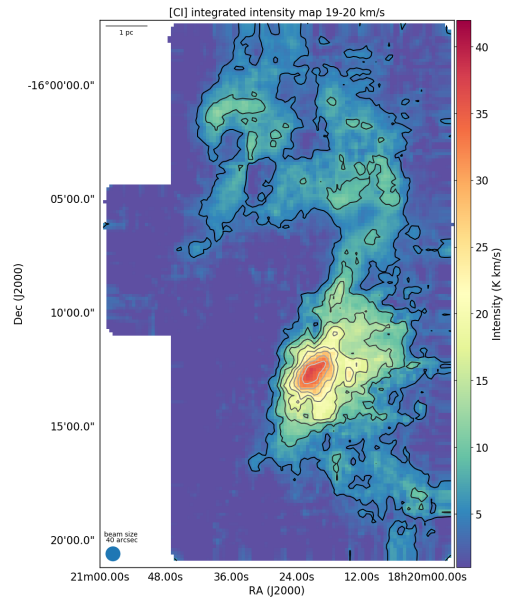
Figure D.10: [CI] $^3P_1$-$^3P_0$ integrated intensity map between 19 and 20 km/s.

Figure D.11: [CI] $^3P_1$-$^3P_0$ integrated intensity map between 20 and 21 km/s.
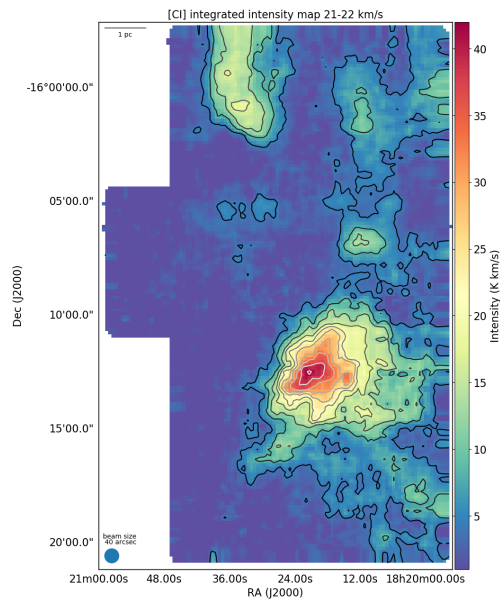
Figure D.12: [CI] $^3P_1$-$^3P_0$ integrated intensity map between 21 and 22 km/s.
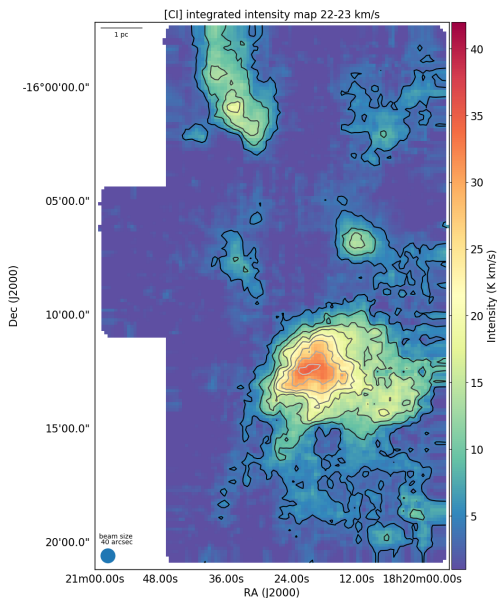
Figure D.13: [CI] $^3P_1$-$^3P_0$ integrated intensity map between 22 and 23 km/s.
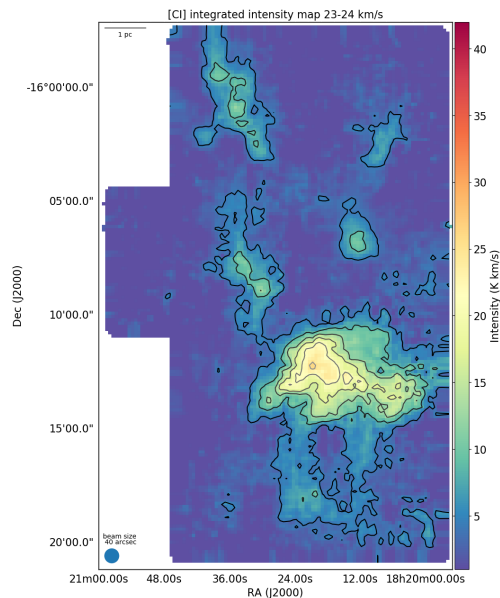
Figure D.14: [CI] $^3P_1$-$^3P_0$ integrated intensity map between 23 and 24 km/s.
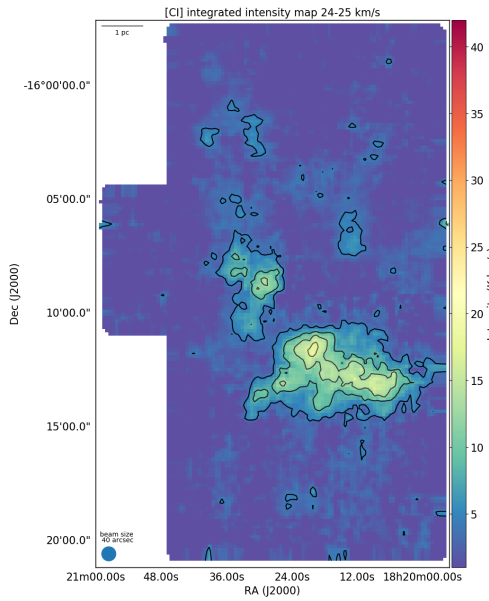
Figure D.15: [CI] $^3P_1$-$^3P_0$ integrated intensity map between 24 and 25 km/s.
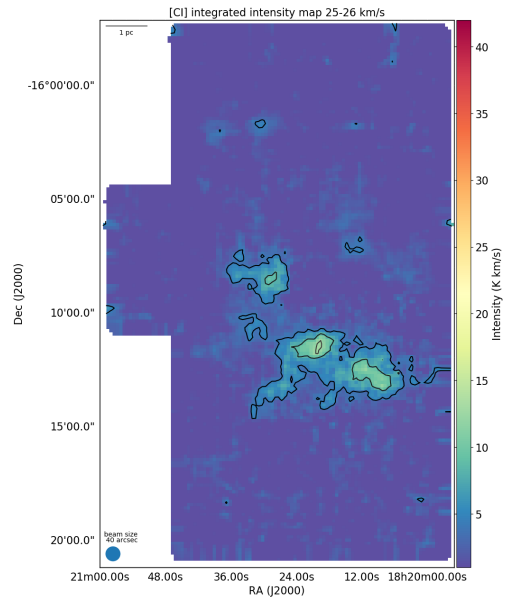
Figure D.16: [CI] $^3P_1$-$^3P_0$ integrated intensity map between 25 and 26 km/s.
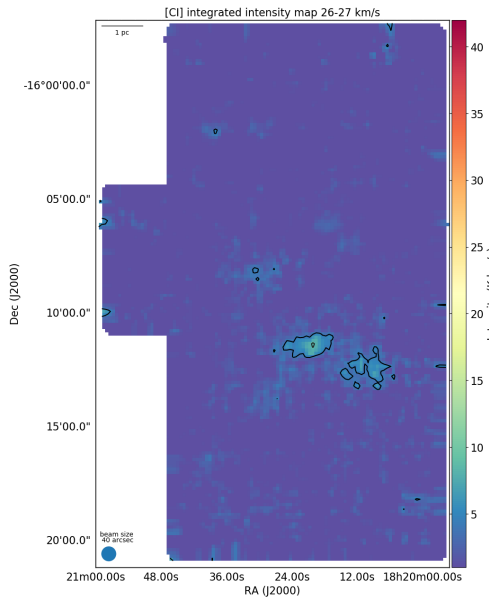
Figure D.17: [CI] $^3P_1$-$^3P_0$ integrated intensity map between 26 and 27 km/s.
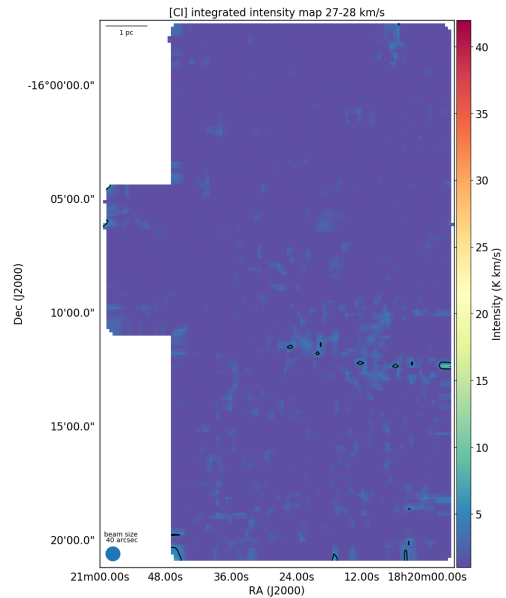
Figure D.18: [CI] $^3P_1$-$^3P_0$ integrated intensity map between 27 and 28 km/s.
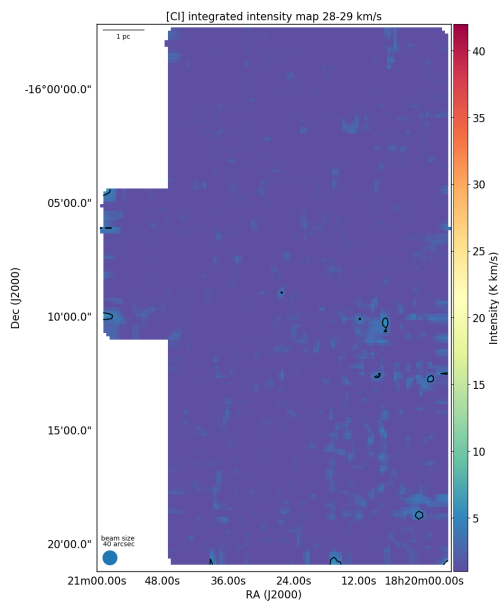
Figure D.19: [CI] $^3P_1$-$^3P_0$ integrated intensity map between 28 and 29 km/s.
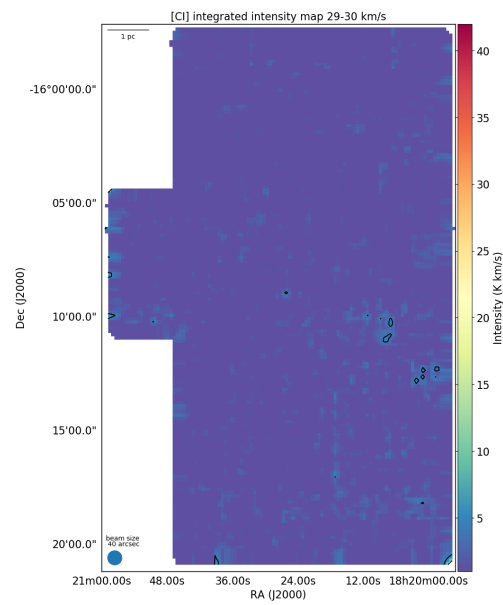
Figure D.20: [CI] $^3P_1$-$^3P_0$ integrated intensity map between 29 and 30 km/s.

List of Figures

List of Tables

Acknowledgements

Erklärung

Ich versichere, dass ich die von mir vorgelegte Dissertation selbständig angefertigt, die benutzten Quellen und Hilfsmittel vollständig angegeben und die Stellen der Arbeit — einschließlich Tabellen, Karten und Abbildungen — , die anderen Werken im Wortlaut oder dem Sinn nach entnommen sind, in jedem Einzelfall als Entlehnung kenntlich gemacht habe; dass diese Dissertation noch keiner anderen Fakultät oder Universität zur Prüfung vorgelegen hat; dass sie — abgesehen von unten angegebenen Teilpublikationen — noch nicht veröffentlicht worden ist sowie, dass ich eine solche Veröffentlichung vor Abschluss des Promotionsverfahrens nicht vornehmen werde. Die Bestimmungen der Promotionsordnung sind mir bekannt. Die von mir vorgelegte Dissertation ist von Professor Dr. Jürgen Stuztki betreut worden.

Teilpublikationen:

- "[CII] 158 μm self-absorption and optical depth effects"
  C. Guevara, J. Stutzki, V. Ossenkop-Okada, R. Simon, J. P. Pérez-Beaupuits, H. Beuther, S. Bihr, R. Higgins, U. Graf, and R. Güsten, **submitted to A&A.**

Ich versichere, dass ich all Angaben wahrheitsgemäßnach bestem Wissen und Gewissen gemacht habe und verpflichte mich, jedmögliche, die obigen Angaben betreffenden Veränderungen, dem Dekanat unverzüglich mitzuteilen.

Köln,   Cristian Guevara N.